STP 605

PROPERTIES RELATED TO FRACTURE TOUGHNESS

AMERICAN SOCIETY FOR TESTING AND MATERIALS

PROPERTIES RELATED TO FRACTURE TOUGHNESS

A symposium
presented at the
Seventy-eighth Annual Meeting
AMERICAN SOCIETY FOR
TESTING AND MATERIALS
Montreal, Canada, 22-27 June 1975

ASTM SPECIAL TECHNICAL PUBLICATION 605
W. R. Warke, Volker Weiss, and
George Hahn, symposium cochairmen

List price $15.00
04-605000-30

AMERICAN SOCIETY FOR TESTING AND MATERIALS
1916 Race Street, Philadelphia, Pa. 19103

Library of Congress Catalog Card Number: 76-9741

NOTE
The Society is not responsible, as a body,
for the statements and opinions
advanced in this publication.

Printed in Baltimore, Md.
August 1976

Foreword

The symposium on Properties Related to Fracture Toughness was presented at the Seventy-eighth Annual Meeting of the American Society for Testing and Materials held in Montreal, Canada, 22-27 June 1975. Committee E-24 on Fracture Testing of Metals sponsored the symposium. W. R. Warke, Illinois Institute of Technology, Volker Weiss, Syracuse University, and George Hahn, Battelle Memorial Institute, presided as symposium cochairmen.

Related ASTM Publications

Fracture Analysis, STP 560 (1974), $22.75, 04-560000-30

Fracture Toughness and Slow-Stable Cracking, STP 559 (1974), $25.25, 04-559000-30

Progress in Flaw Growth and Fracture Toughness Testing, STP 536 (1973), $33.25, 04-536000-30

A Note of Appreciation to Reviewers

This publication is made possible by the authors and, also, the unheralded efforts of the reviewers. This body of technical experts whose dedication, sacrifice of time and effort, and collective wisdom in reviewing the papers must be acknowledged. The quality level of ASTM publications is a direct function of their respected opinions. On behalf of ASTM we acknowledge with appreciation their contribution.

ASTM Committee on Publications

Editorial Staff

Contents

Introduction 1

Fracture Toughness Concept—G. C. SIH 3

Fracture Process in Metals 5
Strain Energy Density Theory 7
Bifurcation Near Free Surface 9
Growth Characteristics of Thumbnail Cracks 12
Concluding Remarks 13

Microstructural Aspects of Fracture Toughness—V. WEISS, Y. KASAI, AND K. SIERADZKI 16

Fracture-Toughness Ductility Relationships 17
Microstructural Consideration 26

Relationship Between Tensile Properties and Microscopically Ductile Plane-Strain Fracture Toughness—R. H. SAILORS 34

Materials 36
Flow Stress from Crack Opening Displacement 36
Crack Tip Strain Distribution 42
Delineation of Length of Parameter 50
Comparison of Calculated and Measured Values of K_{Ic} 52
Medium-Carbon Machinery Steels 55
Discussion 56
Summary and Conclusions 59

Relationship Between the Fracture Toughness and the Crack Tip Radius—R. TAGGART, K. K. WAHI, AND R. BEEUWKES, JR. 62

Experimental Procedure 64
Results and Discussion 66
Conclusions 69

Microstructure and Toughness of High-Strength Aluminum Alloys—J. T. STALEY 71

Constituent Particles 72
Dispersoid Particles 74
Hardening Precipitates 80
Summary 91
High-Toughness Alloys 94

Discussion 96

Fracture Analysis of Various Cracked Configurations in Sheet and Plate Materials—J. C. NEWMAN, JR. 104

Two-Parameter Fracture Criterion 106
Failure Predictions 108
Analysis of Test Data 109
Plane-Stress and Plane-Strain Fracture 118
Concluding Remarks 120

Mechanical Behavior Model for Graphites—J. D. BUCH 124

Pore-Free, Well-Bonded Isotropic Graphites 125
Porosity 131
Grain Boundaries 136
Anisotropy 138
Volume Effect 140
Discussion 140
Summary 142

Introduction

It has always seemed reasonable that a material's resistance to crack propagation should be related to other mechanical and physical properties, such as strength, ductility, work hardening exponent, etc. A workshop on the subject held in 1973 drew considerable interest. Twelve speakers discussed the relationship between toughness and properties based on a variety of fracture models.

In view of the current interest in the subject it was decided to hold a symposium so that a broader spectrum of speakers could participate and a larger portion of the technical community could be exposed to this timely area of technology.

The objective of the symposium was to provide a forum for the presentation of papers dealing with the relationships between fracture, that is, progressive crack extension, and the structure and properties of solids.

In support of this objective, papers dealing with the relationship of toughness to interatomic potentials and bond strengths; slip character and distribution; nature and distribution of microconstituents and inclusions; uniaxial tensile properties such as yield strength, fracture strain, and work hardening exponent; and plane-strain tensile strength and ductility were included in the symposium.

This publication contains the papers presented at the symposium and subsequently submitted for publication.

Volker Weiss

Professor, Department of Chemical Engineering and Materials Science, Syracuse University, Syracuse, N. Y. 13210; symposium cochairman.

G. C. Sih[1]

Fracture Toughness Concept

REFERENCE: Sih, G. C., "**Fracture Toughness Concept,**" *Properties Related to Fracture Toughness, ASTM STP 605,* American Society for Testing and Materials, 1976, pp. 3–15.

ABSTRACT: Fracture toughness is an indication of the resistance of a material to physical separation by a process of unstable macrocrack propagation. Conceptually, it is an intrinsic material parameter that should not vary with changes in specimen size, speed of loading, temperature, etc.

The brittle-ductile transition size effect of metal specimens is discussed using the strain energy density theory. By assuming that the critical strain energy factor, S_{cr}, is a material constant, predictions on the fracture behavior of metals can be made. The following remarks are helpful toward defining a fracture toughness parameter associated with instability of the macrocrack:

1. The dominant or continuum crack travels in the elastic portion of the material always skirting around or bypassing the yield material and hence releases only elastic energy.
2. Stable macrocrack growth in metals is the result of necking or constraint from specimen boundary.
3. The last ligament of macrofracture will terminate in a plane inclined to the free surface or boundary of the specimen.

KEY WORDS: fracture properties, toughness, crack propagation, plastic deformation, tensile strength, mechanical properties

Recent advances in linear fracture mechanics have enabled engineers to use the fracture toughness of a material as a design parameter. The approach relies on using small specimens to obtain data and translating this information to the design of a larger size structure. To date, no real confidence in this approach has been established, particularly for metal specimens or structural components. This is partly due to the lack of an understanding of fracture size effect, that is, smaller specimens appear to be more ductile than larger specimens. Changes in the rate of loading and temperature can also make the same material to behave either in a brittle or ductile manner.

[1] Professor of mechanics and director of the Institute of Fracture and Solid Mechanics, Lehigh University, Bethlehem, Pa. 18015.

The linear theory is limited to plane-strain fracture as according to the American Society for Testing and Materials (ASTM) [*1*][2] the smallest dimension of the specimen, say δ, should satisfy an inequality $\delta \geq 2.5 (K_{Ic}/\sigma_{ys})^2$, where K_{Ic} is the fracture toughness and σ_{ys} the yield strength of the material. To overcome this limitation, the physical causes that are responsible for the nonlinear and irreversible[3] behavior of the metal must be understood and properly recognized in analytical modeling.

Under normal conditions, fracture mechanics attempts to associate the point of instability on the load-deformation curve with a critical crack size in the specimen. This is clearly a departure from the conventional continuum mechanics approach which considers either a critical stress, strain, or some other quantity without taking into account the dimensions of the defects that start the process of material separation. At the macroscopic level, the objective is to avoid having the dominant crack reach a critical size at which catastrophic failure may result.

The concept of "fracture toughness" relies on the existence of a parameter that represents the inherent characteristics of the material. It can then be related to load and geometry to determine the subcritical or critical size of defects as a function of the applied stress. The energy release rate approach of Griffith [*2*] and Irwin [*3*] has had reasonable success in predicting brittle fracture. In particular, the assumption that numerous cracks exist in any real material and that fracture occurs when the largest existing crack reaches a critical size eliminates several orders of magnitude discrepancy between the theoretical and experimentally observed tensile strength of single crystals.

Past attempts to extend the Griffith's concept to the more ductile materials are not clear and raise some serious questions [*4*]. First of all, they failed to recognize the important feature of metal fracture characterized by slow crack growth[4] that leads to rapid, unstable crack propagation. Next, material damage within the yielded portion of the material is microscopic in size and cannot be readily identified with the point of instability on the load-deformation curve. In other words, it is difficult to account for the dissipated energy that is not available to drive unstable macrocrack propagation. Instability caused by material separation at the macro- and microscales must be carefully distinguished. Experimental measurements include both types of damage, while analysis may account only for one or the other. Compatibility between the analytical model and physical behavior of material must be observed.

[2] The italic numbers in brackets refer to the list of references appended to this paper.

[3] Irreversibility caused by stable macrocrack extension is not the same as that introduced by the creation of microcracks which normally is modeled as plastic deformation in continuum mechanics.

[4] Stable crack growth can also occur under a constant sustained load (creep) or cyclic loadings (fatigue). The present discussion is limited to metal specimens under monotonically rising load prior to unstable crack extension.

In order to have a better understanding of fracture toughness, an attempt is made to clarify the fracture development process in metals with the objective of explaining the influence of size on ductility—the brittle-ductile transition size effect. The insufficiency of existing theories is evidenced by the fact that the parameters they propose are sensitive to changes in specimen sizes or apply only for a very limited range of sizes. There is a lack of ways in which the physical problem can be realistically modeled without confronting an insurmountable amount of mathematics.

Metal fracture behavioral prediction based on the strain energy density theory [*5*,*6*] for bodies with cracks is discussed. Assuming that the critical strain energy density is a material constant, the growth characteristics of a crack as it approaches a free boundary are made. The results show that there is a tendency for the crack to branch near a free surface even in the absence of plasticity. This effect is more pronounced as the distance between the crack tip and specimen boundary is decreased and as yielding takes place. A similar situation occurs ahead of a thumbnail crack in a finite thickness plate when it penetrates through the plate surfaces. The need for analyzing the different crack profiles as it grows from a stable to an unstable state cannot be overemphasized. This can be accomplished by examining the change of stiffness or compliance of the specimen for each increment of crack extension until an instability point on the load-deformation curve is observed.

Fracture Process in Metals

Microfractography and macrofractography have become of interest to investigators relating the mechanical behavior of metals to the appearance of their fracture surfaces. Observations of the surfaces of broken metals have led to descriptive accounts, often associated with ductility or brittleness, of the fracturing process. However, there has been no significant progress made toward quantifying the observed phenomena of fracture. On the other hand, there is an enormous burden on any theory that attempts to predict the entire history of material failure from crack nucleation to propagation and final separation. This process is further complicated by its dependency on temperature, the speed of load application, and specimen geometry.

What will be discussed here are the basic features of ductile fracture that should be modeled in the analysis. Evidence from the fracture surfaces of broken metal specimens shows that there are three distinct stages of fracture development, each of which possesses a difference surface appearance[5] and instability at the macroscopic level. These stages are designated as I, II, and III for the fracture surface of a tensile bar as

[5] No attempt will be made here to describe or analyze the detailed appearance of the fracture surfaces, whether fibrous, granular, or cleaved. Incorporation of these effects in the analysis is beyond the scope of this work and the capacity of our analysis.

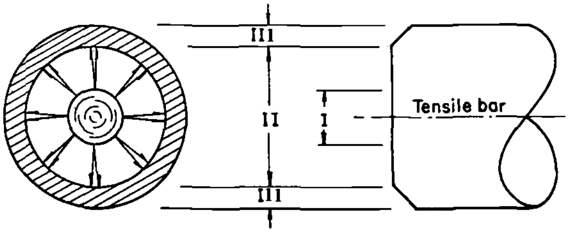

FIG. 1—*Three stages of fracture in a tensile bar: (I) slow crack growth, (II) rapid crack propagation, and (III) last ligament of failure—shear lip.*

shown in Fig. 1. Fracture originates inside region I which represents slow or stable crack growth. It then changes to rapid or unstable crack propagation indicated by region II. Final separation of the material begins as the crack turns away from the normal to the free surface. This slanted fracture surface is referred to normally as the shear lip zone III. The boundary separating stages I and II represents a transition from slow to rapid fracture, while the time elapsed between stages II and III is so short that the load and deformation do not change appreciably during this period.

The final stage of the fracturing process is that of the formation of the shear lip.[6] At this point, the material snaps, and a sharp drop on the load-deformation curve can be observed. Because the fracturing process is seldom symmetrical, the shear lip always appears only on one half of the broken specimen. Some discussions on the way in which the shear lip is formed are in order. Preliminary analysis indicates that plastic zones are formed on both sides of the plane of the macrocrack as it moves through the material. Upon approaching the specimen edge, the plastic zones intersect the free boundary, and an additional island of yielded material appears, leaving a forked region of elastic material. The result in Fig. 2 suggests that the shear lip forms as the macrocrack bifurcates through the forked elastic region.[7] Should this be the case, which could be checked from a fracture criterion such as the strain energy density theory, the implication is that instability on the load-deformation curve at the continuum level corresponds to release of elastic energy by the macrocrack. To reiterate, plasticity appears to reduce the available energy for causing macrocrack instability. The material in the plastic zone is damaged on a microscopic scale level where the effect of instability is not easily measurable in terms of load.

Before applying the concept of fracture toughness to characterize metal

[6] In those cases where the bar necks down continuously to a point without developing the shear lip, the instability of the material separation process is occurring on a different scale level.

[7] This is in contrast to the current open literature belief that the shear lip is formed within the plastic zone as the crack approaches the specimen boundary.

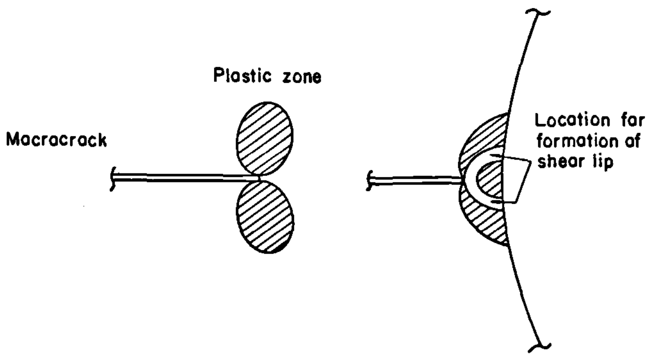

FIG. 2—*Shear lip formation.*

fracture, it is pertinent to discuss the effect of specimen size on the three stages of fracture development. Experimental measurements on the relative size of regions I, II, and III for a range of specimen diameters are available [7]. The behavior for aluminum, titanium, and steel alloys are all similar and is illustrated in Fig. 3, where the lineal dimensions of these regions are compared with the increasing specimen diameter. Note that as the specimen diameter increases, region II increases at a much greater rate than regions I and III. In other words, the region in which rapid crack extension occurs normal to the load increases with increasing section size. This tends to support the concept of a critical shear lip size which is relatively insensitive to changes in specimen size. Hence, an analytical understanding of shear lip formation is much needed for resolving the size effect problem in metal fracture.

Strain Energy Density Theory

Successful prediction of metal fracture depends on the effectiveness of stress analysis, soundness of failure criterion, and an understanding of the

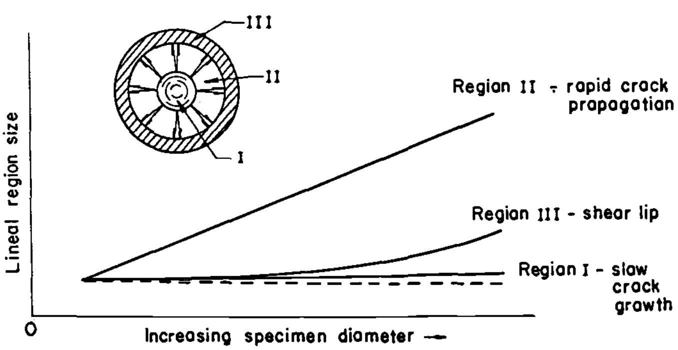

FIG. 3—*Lineal region size versus specimen diameter.*

actual fracture process. Repeated careful experiment and observation have revealed that crack propagation is not a continuous process but occurs discretely by breaking elements of material in regions ahead of the crack. Hence, any theories that assume continuous advancement of the crack such as the energy release rate concept will have limited application. Such an assumption does not lend itself to cracks that do not propagate in a self-similar manner and can lead to analyses involving unwarranted and unprofitable labor. Too much emphasis cannot be placed on predicting the direction[8] of crack propagation in three dimensions which is a prerequisite for analyzing metal fracture.

One of the basic concepts of the S-criterion is that fracture initiates from an interior element located at a finite distance r from the crack front [5,6]. This distance has been referred to as the radius of the core region within which the material can be highly distorted and its mechanical properties can be very different from those in the bulk [8]. Moreover, investigation of three-dimensional fracture behavioral prediction should be carefully distinguished from two-dimensional crack behavior. In two dimensions, fracture initiates from a point element ahead of the crack where the strain energy density factor S reaches a critical value, S_{cr}, and if the fracture is considered as three-dimensional, then there is a whole line of critical elements parallel to the straight crack edge. In truly three-dimensional problems such a line cannot be expected to be parallel with the crack border, and the position (r_o,θ_o,ϕ_o) of each isolated point element must be determined separately, Fig. 4. The basic assumptions of the S-criterion may be summarized as follows [5]:

1. Crack initiation takes place in a direction of minimum strain energy density factor, S, that is, $\partial S/\partial\theta = 0$, $\partial S/\partial\phi = 0$ at $\theta = \theta_o$ and $\phi = \phi_o$.
2. Crack extension occurs when the minimun strain energy density factor, S_{min}, reaches a critical value, S_{cr}.
3. The radius of core region, r, locating the points of initial fracture is assumed to be proportional to S_{min} such that S_{min}/r remains constant.

Assumptions 1 and 2 are sufficient for determining where and when crack propagation occurs in a two-dimensional problem in which all the elements are assumed to fail at the same distance r from the straight crack front. In three dimensions, the crack front is generally curved, and the distance r may vary from point to point along the crack border as illustrated in Fig. 4.

[8] Until recently, the only widely known criterion for predicting the direction of crack propagation was based on the maximum normal stress. It is common knowledge that this theory can be applied with confidence only if one of the normal stresses dominate while the others are absolutely smaller.

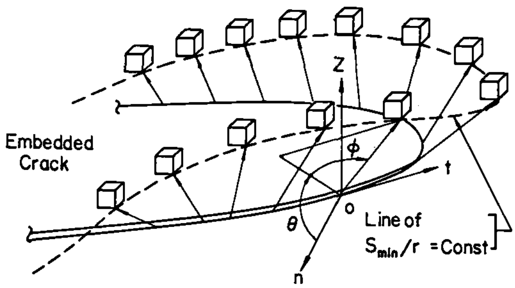

FIG. 4—*Material elements near crack border.*

Referring to Fig. 4, the strain energy density factor for an element (r, θ, ϕ) near a crack of arbitrary shape may be written as[9]

$$S = a_{11}k_1^2 + 2a_{12}k_1k_2 + a_{22}k_2^2 + a_{33}k_3^2 \tag{1}$$

in which the coefficients a_{ij} ($i, j = 1, 2, 3$) depend on the elastic constants μ and ν and the angles θ and ϕ

$$\begin{aligned}
16\,\mu\cos\phi\, a_{11} &= (3 - 4\nu - \cos\theta)(1 + \cos\theta) \\
16\,\mu\cos\phi\, a_{12} &= 2\sin\theta(\cos\theta - 1 + 2\nu) \\
16\,\mu\cos\phi\, a_{22} &= 4(1 - \nu)(1 - \cos\theta) + (3\cos\theta - 1)(1 + \cos\theta) \\
16\,\mu\cos\phi\, a_{33} &= 4
\end{aligned} \tag{2}$$

The angle θ is located in the nz-plane normal to the crack border. The direction of maximum strain energy density factor corresponds to the direction of maximum yielding. Further insights into the S-criterion may be gained by resolving S into two component parts, one associated with volume change and the other with shape change as discussed in Refs *5,6*.

With this brief introduction on the S-criterion, it is now more pertinent to discuss the physical aspects of the problem of a through crack growing in a ductile material.

Bifurcation Near Free Surface

The three stages of fracture development as mentioned earlier are independent of specimen geometry. Only the sizes of the individual

[9] The simpler expressions in Eqs 1 and 2 are equivalent to those complicated ones in Ref *10* provided that the angles θ and ϕ are defined according to Fig. 4 and a mistake in the expansion of one of the ellipsoidal coordinates is corrected.

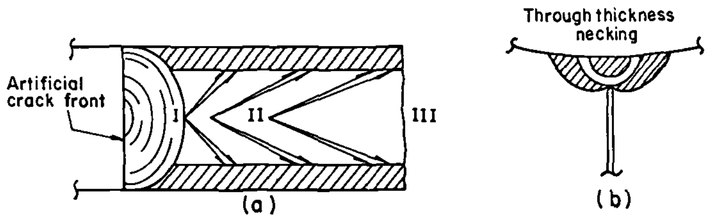

FIG. 5—*Regions of fracture development in flat plate.*

regions are varied as the specimen geometry is changed. Figure 5*a* refers to the fracture behavior of a cracked plate specimen. The region of stable crack growth contains crack fronts which are curved while the final separation of material takes place near the plate surface where the shear lip is formed and takes on the general contour of the reduced section. Figure 5*b* illustrates the formation of a shear lip and the associated plastic zones which are similar to those in Fig. 2 for a round bar. Size effects of plate specimens are also similar to those observed for bar specimens where region III, the shear lip, does not vary nearly as much with the plate thickness as the size of region II in which unstable crack propagation occurs.

Clearly, stages I, II, and III are inherent features of metal fracture observable on the macroscopic level. For the more brittle materials, these three stages are close to one another and fracture instability appears to occur instantaneously without warning or slow crack growth. In such a case, critical load data taken on artificially introduced cracks of various sizes can be meaningfully interpreted by a two-dimensional analysis. In metals, the three-dimensional aspects of the fracture process, as illustrated in Fig. 1 or Fig. 5, cannot be ignored. The arbitrary insertion of a through crack in a metal plate merely introduces an additional boundary, the crack front, from which fracture will be developed through the three stages as mentioned earlier.

Theoretical treatment of three-dimensional elastic-plastic crack problems is to say the least extremely difficult. Our present day knowledge of mathematics and mechanics is not adequate for describing the three stages of fracture development on a continuous time scale. Hence, analysis is limited to the combination of loading and crack geometry at a given instance of the fracture process. To begin with, a two-dimensional crack model of plane strain which incorporates a continuum theory of plasticity can shed some light on the bifurcation phenomenon of a crack approaching a free surface. Figure 6*a* gives a schematic of the plane-strain problem of a central crack whose tips are close to the specimen boundary where plasticity[10] is developed in front of the crack near the free surface.

[10] The sizes of the plastic zones in Fig. 6 are exaggerated since the specimen boundary normally will be highly distorted or curved. This means that less energy will be available to yield the material.

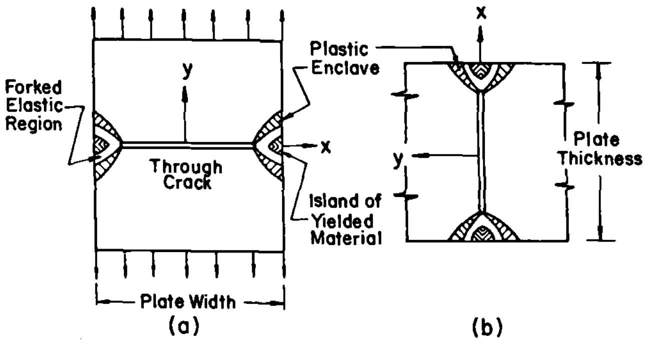

FIG. 6—*Plastic zones for crack edges near specimen boundary.*

Note that in addition to the usual plastic enclaves, which have now merged with the specimen edge, there is an island of yielded material, leaving a forked region of elastic material. The same situation applies to a thumbnail crack whose edge is close to the top and bottom surfaces of a finite thickness plate. A cross-sectional view of the thumbnail crack accompanied by plastic deformation can be obtained simply by rotating Fig. 6*a* 90 deg and replacing the plate width in the plane-strain problem by plate thickness in the three-dimensional problem as indicated in Fig. 6*b*. The strain energy density theory will actually predict branching of the main crack [9] with a chip of material falling off the edge, Fig. 7*a*. This is consistent with the experimentally observed departure of crack direction in the last ligament of growth. In reality, the crack never forks symmetrically. A slanted fracture surface on the separated pieces, Fig. 7*b*, are always observed because of nonalignment of load and specimen. The formation of shear lips which occur as a thumbnail crack breaks through to the plate surfaces has the same physical cause as the cup and cone fracture of a round bar. Figure 7*b* can also be viewed as a broken tensile bar. The central portion of the fracture is normal to the direction of tension, while the outer portions of it form a cone inclined at an angle of approximately 45 deg with respect to the axis of the specimen, "cup and cone" fracture. In fact, the shear lips formed in through thickness

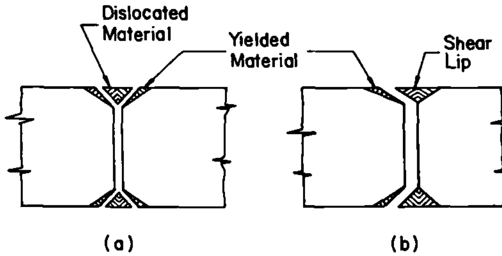

FIG. 7—*Slanted fracture near a free surface.*

cracking are also inclined at approximately 45 deg to the direction of loading.

There is evidence to the effect that the main crack forks in the elastic portion of the material. The continuum crack always appear to avoid running into the yielded material and hence releases only elastic energy. The plastic or yielded portion of the material is relatively soft and can only sustain mechanical damage at the microscopic level. This argument is based on a detailed elastic-plastic stress analysis coupled with the strain energy density criterion. It is anticipated that a three-dimensional elastic-plastic analysis of a through crack in a plate will lead to the same conclusion.

Growth Characteristics of Thumbnail Cracks

In order to reproduce the fracture growth patterns discussed earlier, the strain energy density criterion can be applied to forecast thumbnail profiles having a constant strain energy density, $dw/dV = S/r$. The material elements along these profiles experience more volume change than shape change. A series of possible new crack front shapes, as illustrated in Fig. 8*a*, can be determined for various values of the parameters involved, say σ (applied stress), σ_{ys} (yield strength), n (strain hardening exponent), a (half crack length), h (plate thickness), ρ (crack tip radius of curvature), etc. For a particular set of parameters, the new crack front shape, as predicted by the strain energy density criterion, will be the basis of a second set of stress calculations. If the analysis for the extended crack indicates that an increased load is required to obtain further crack extension using the same growth criterion, then the crack extension will be considered to be stable and the analysis will be repeated to study further growth. The compliance values for the various stages of crack growth can then be determined as the crack front tunnels through the midsection of the plate and possible branches near the plate surface, Fig. 8*b*. The results may be summarized in mathematical form as

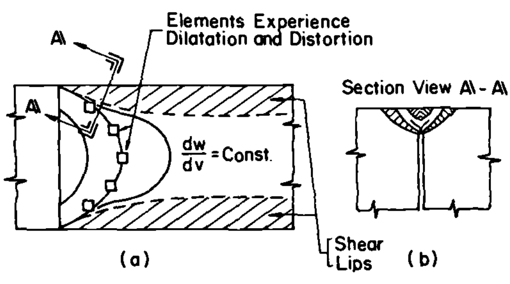

FIG. 8—*Cross-sectional view of crack growth behavior.*

$$S_{cr} = S\left(\frac{\sigma}{\sigma_{ys}}, n, \frac{\rho}{a}, \frac{h}{a}\right) \tag{3}$$

where the critical value of some strain energy density factor, S_{cr}, can be used as a material constant. Initially, the motion of the thumbnail crack, Fig. 8*a*, will be constrained by the shear lips, and the crack grows slowly as the load increases. As soon as the size of the thumbnail overcomes the thickness constraint, unstable rapid crack propagation begins. This can be identified on the global stress-strain curve. Some preliminary work on this difficult and complicated problem can be found in Ref *9*.

Concluding Remarks

One of the least understood problems in fracture mechanics is that of crack propagation in a material that deforms beyond its elastic limit. The assumption made in many of the existing two-dimensional models is that the crack propagates through a plastic zone as implied in the models of circular enclave, plastic fan, narrow strip, etc. The application of these models to explain metal fracture of bar or plate specimens raises some serious questions, since fracture of metal bars and plates is basically a three-dimensional phenomenon and cannot be adequately explained by any two two-dimensional analyses which ignore the specimen boundary effect [*11*]. Too often, agreement between theory and experiment is purely coincidental or contrived. A classical example is the plasticity strip model for predicting the yielded zone size in thin metal sheets or plates. The so-called observed "plasticity" ahead of the crack is due to necking of the material in the thickness direction, while the analysis considers no such effect and is strictly a planar one. A refined two-dimensional elastic-plastic stress analysis will reveal that the material along the line of expected crack extension will not distort sufficiently to cause yielding.

In most structural metals, where the separation event is preceded by slow crack growth, the classical notion of fracture toughness fails to apply. This is mainly because of the inability of the theory to explain the brittle-ductile transition phenomenon. By assigning different fracture toughness values to the same material that may behave either in a brittle or ductile manner depending on the rate of loading, temperature or specimen size or both is certainly not the answer. Clear concepts are necessary to understand the meaning of fracture toughness as applied to metal fracture. Yielding is known to affect the load at which unstable crack propagation commences but not necessarily the fracture toughness. The region within which microcracks prevail should be distinguished from that of macrocrack extension at the point of load instability. An analysis at the macroscopic scale level requires a suitable fracture criterion that is capable of separating the zones of yielding from unstable fracture. The strain energy density or S-criterion is well suited for this purpose since it can simultaneously predict the locations of fracture ($S_v > S_d$) and yielding ($S_d > S_v$), where S_v is the energy density factor associated with volume change and S_d with shape change. Moreover, the formation of shear lips in ductile fracture necessitates a criterion that can predict noncoplanar crack growth.

The critical strain energy density factor, S_{cr}, is proposed as a possible material constant for finding the load carrying capacity of metals. Experimental determination of S_{cr} should be associated with load instability at which the macrocrack acquires unstable motion. The time interval within which this instability occurs is assumed to be sufficiently small so that the analysis need not consider the microscopic damage along the path of macrocrack extension. The continuum mechanics view is that plastic deformation occurs in regions away from the macrocrack trajectory, and its only influence is to reduce the available macrocrack extension force. In other words, the continuum crack tends to spread in the elastic portion of the material and releases only elastic energy. Hence, dilatation or volume change would appear to be the dominant mode of energy dissipation. Although it is often difficult to determine the precise locations where brittle fracture terminated and ductile fracture started or vice versa, the events of initiation of stable crack growth (local instability) and onset of rapid crack propagation (global instability) can be identified on the nonlinear stress-strain curve.

Acknowledgment

This work is supported by the Office of Naval Research, Arlington, Virginia, through contract N00014-76-C-0094 with Lehigh University, Bethlehem, Pennsylvania.

References

[1] *Plane Strain Crack Toughness Testing of High Strength Metallic Materials*, W. F. Brown, Jr., and J. E. Strawley, Eds., *ASTM STP 410*, American Society for Testing and Materials, 1966.

[2] Griffith, A. A., *Philosopical Transactions of the Royal Society*, Vol. A221, 1921, pp. 163-198.

[3] Irwin, G. R. in *Structural Mechanics*, Pergamon Press, London, 1960, pp. 560-574.

[4] Sih, G. C., *Engineering Fracture Mechanics*, Vol. 5, 1973, pp. 365-377.

[5] Sih, G. C. in *Methods of Analysis and Solutions of Crack Problems*, G. C. Sih, Ed., Noordhoff International Publishing, Leyden, the Netherlands, 1973, pp. 21-45.

[6] Sih, G. C., *International Journal of Fracture*, Vol. 10, 1974, pp. 305-321.

[7] DeSisto, T. S., Carr, F. L., and Larson, F. R. in *Proceedings*, American Society for Testing and Materials, Vol. 63, 1963, pp. 768-779.

[8] Sih, G. C. in *Proceedings on the Prospects of Fracture Mechanics*, G. C. Sih, H. C. van Elst, and D. Broek, Eds., Noordhoff International Publishing, Leyden, The Netherlands, 1974, pp. 85-102.

[9] Sih, G. C., Hilton, P. D., Hartranft, R. J., and Kiefer, B V. "Three-Dimensional Stress Analysis of a Finite Slab Containing a Transverse Central Crack," Technical Report

IFSM-75-69, Institute of Fracture and Solid Mechanics, Lehigh University, Bethlehem, Pa., June 1975.
[10] Sih, G. C. in *Three-Dimensional Crack Problems*, G. C. Sih, Ed., Noordhoff International Publishing, Leyden, The Netherlands, 1975, pp. 15-53.
[11] Sih, G. C. in *Proceedings on the Prospects of Fracture Mechanics*, G. C. Sih, H. C. van Elst, and D. Broek, Eds., Noordhoff International Publishing, Leyden, The Netherlands, 1974, pp. 613-620.

V. Weiss[1], *Y. Kasai*[1], *and K. Sieradzki*[1]

Microstructural Aspects of Fracture Toughness

REFERENCE: Weiss, V., Kasai, Y., and Sieradzki, K., "**Microstructural Aspect of Fracture Toughness,**" *Properties Related to Fracture Toughness, ASTM STP 605,* American Society for Testing and Materials, 1976, pp. 16–33.

ABSTRACT: For most technical materials the dominant mechanism resisting crack extension is plastic deformation. Continuum mechanics analysis shows that fracture toughness, in addition to depending on Young's modulus, flow stress, strain hardening exponent, and yield strain, should be nearly proportional to the effective fracture ductility obtained for the stress state characteristic for the region ahead of the crack; plane stress or plane strain. The original equation for plane-strain fracture toughness-equibiaxial ductility is refined to include the effects of strain hardening. Such a correlation has been experimentally confirmed for steels; K_{Ic} was found to be proportional to the effective equibiaxial ductility. A model for the thickness effect on K_c has been developed on the basis of these observations and is in fair agreement with experimental results.

The dominant microstructural events that control ductility, and therefore fracture toughness, are void nucleation, void growth, and void coalescence. Void nucleation at an inclusion—matrix interface is governed by the value of the interface strength—flow stress difference and is, consequently, temperature sensitive. Models for void growth mechanisms show the void coalesence strain to be a strong function of the nuclei density but rather insensitive to temperature. Qualitative relationships are presented which give some insight into the microstructural causes for ductility and fracture toughness transitions (or their absence in face-centered-cubic materials) with temperature, and can serve for the development of new high-toughness materials.

KEY WORDS: fracture properties, plastic deformation, toughness, ductility, voids, mechanical properties, nucleation

[1] Professor, research fellow on academic leave from Daido Steel Co., Ltd., Nagoya, Japan, and graduate research assistant, respectively, Department of Chemical Engineering and Materials Science, Syracuse University, Syracuse, N.Y. 13210.

Since Krafft's early work [1][2], much research has been conducted to correlate a material fracture toughness with its uniaxial tensile properties. The key ingredients to most of these approaches are a critical crack tip strain and a length parameter. The former is related to the fracture ductility, usually obtained on smooth tension specimens [2]. Although some of these approaches give useful correlations, the use of the uniaxial tensile fracture ductility must be questioned for several reasons: due to plastic instability the stress state in a tension test changes as a function of strain [3]; tensile fracture ductility itself depends on the section size [4]; and the stress state near the crack tip is multiaxial [5]. In order to avoid this complexity some researchers have employed a "plane-strain tension specimen," for example, as proposed by Clausing [6]. However, even there necking may occur under certain experimental conditions [7,8], thereby altering the stress state in the course of a test. Based on these considerations, Weiss proposed the use of equibiaxial fracture ductility or bulge ductility, for correlation with fracture toughness [9]. The experimental results obtained for steels show a linear relationship between effective bulge ductility and plane-strain fracture toughness with a scatter around 30 percent. The analytical basis for this correlation is a critical mean stress hypothesis for the stress state on fracture strain. This hypothesis has been proposed by Bridgeman [3] and was supported experimentally by the work at Syracuse University [10], by Yajima et al [11], and recently by French et al [12-14].

The first part of the present paper deals with the analytical continuum mechanics aspects of the fracture toughness ductility correlation. The original relationships are extended to include the effects of strain hardening. Experimental evidence for the applicability of these correlations is presented. The second part is an attempt to account for the microstructural mechanisms that control material ductility as a function of stress state.

Fracture-Toughness Ductility Relationships

Analytical Studies

Fracture toughness is the work required to form a unit area crack extension

$$G_c = \frac{\partial W}{\partial A} \tag{1}$$

For metallic materials most of the contribution to ∂W is plastic flow. A simple analysis, presented elsewhere [15], yields for the plane-strain

[2] The italic numbers in brackets refer to the list of references appended to this paper.

fracture toughness

$$G_{Ic} = s\rho^*\bar{\sigma}_0\bar{\epsilon}_{F,\alpha\beta}\left(\frac{\bar{\epsilon}_{F,\alpha\beta}}{\bar{\epsilon}_Y} - 1\right) \tag{2}$$

where

$\bar{\epsilon}_{F,\alpha\beta}$ = local fracture strain near the crack tip under a stress state characteristic for plane-strain condition,
$\alpha = \sigma_2/\sigma_1 = 0.81$ and $\beta = \sigma_3/\sigma_1 = 0.61$ [*16*],
s = shape factor characterizing the geometry of the plastic zone,
ρ^* = Neuber's microsupport effect constant,
$\bar{\sigma}_0$ = flow stress, and
$\bar{\epsilon}_Y$ = yield strain.

Since $\bar{\epsilon}_{F,\alpha\beta}$ cannot be determined experimentally for the plane-strain stress state ahead of a crack, it's value is obtained by extrapolation from the bulge ductility, $\bar{\epsilon}_{F,\,\alpha\,=\,1,\,\beta\,=\,0}$, via the mean stress failure hypothesis, that is, $\bar{\epsilon}_{F,\alpha\beta} = (0.279)^{1/n}\,\bar{\epsilon}_{F,\alpha\,=\,1,\,\beta\,=\,0}$.

In order to determine $\bar{\epsilon}_{F,\alpha\beta}$ by any test other than a fracture-toughness test it is necessary to know the effect of stress state on fracture ductility. Previous studies in this area have confirmed the applicability of a mean-stress failure criterion. Accordingly the fracture strain for a given stress state characterized by $\alpha = \sigma_2/\sigma_1$, $\beta = \sigma_3/\sigma_1$ for a material following an exponential strain hardening relationship of the type of $\bar{\sigma} = k\epsilon^n$ is given by

$$\epsilon_{F,\alpha\beta} = (wm)^{1/n}\epsilon_{TF} = \left(\frac{3\sigma_{mF}}{k}\right)^{1/n}(wm)^{1/n} \tag{3}$$

where

$$\sigma_m = \frac{1}{3}\quad(\sigma_1 + \sigma_2 + \sigma_3),$$

$$w = \frac{1}{1 + \alpha + \beta}\text{, and}$$

$$m = [(1 + \alpha + \beta)^2 - 3(\alpha + \beta + \alpha\beta)]^{1/2}.$$

Figure 1 represents this expression in the form of a ductility surface for $n = 1$. For smaller n values the surface drops off more rapidly towards zero as the condition of hydrostatic stress state of $\alpha = 1$, $\beta = 1$ is

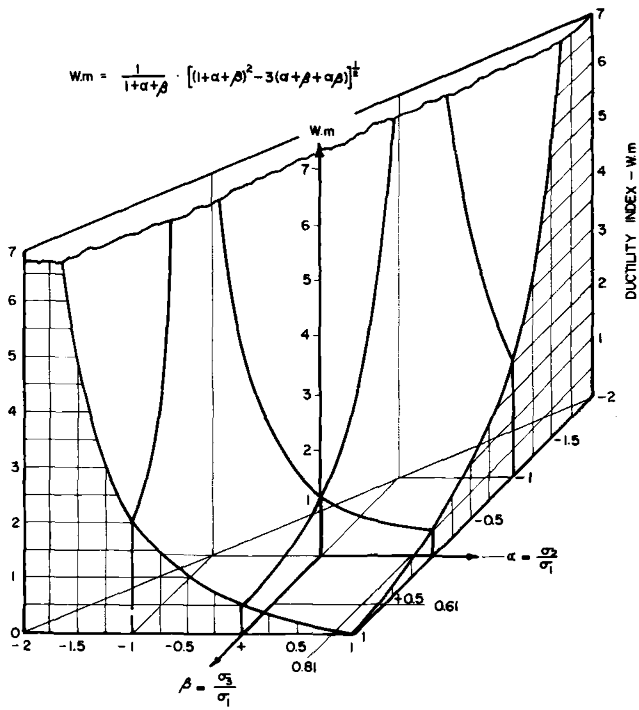

FIG. 1—*Fracture ductility index surface for the mean stress failure criterion.*

$$\bar{\epsilon}_{F,\alpha\beta} = \left(\frac{3\sigma_{mF}}{k}\right)^{1/n} (wm)^{1/m}$$

approached. With the help of this stress state-ductility relationship one can estimate the fracture ductility in the "plane-strain zone" ahead of the crack tip from measurements of other fracture ductilities, such as the bend ductility or the bulge ductility, provided that necking does not precede fracture in these tests. Accordingly, the ratio of bulge ductility to local fracture ductility ahead of a crack under plane-strain conditions is given by

$$\bar{\epsilon}_{F,\alpha = 0.81,\ \beta = 0.61} = (0.279)^{1/n}\ \bar{\epsilon}_{F,\alpha = 1,\ \beta = 0} \tag{4}$$

For the materials considered here fracture toughness, or fracture resistance, is represented by the plastic work, ΔW, accompanying unit crack extension, that is, the plastic work required to advance the plastic zone by Δa, as schematically illustrated in Fig. 2. The work increment is given by $dW = \bar{\sigma} \times d\bar{\epsilon} \times r d\theta dr$ and ΔW is given by

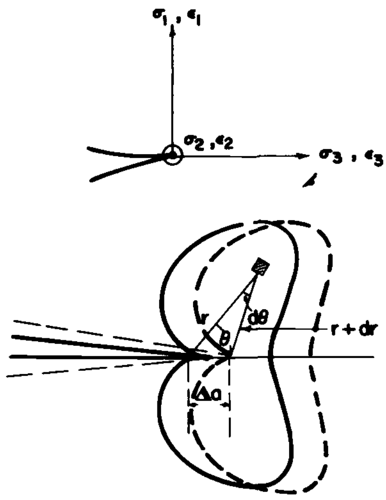

FIG. 2—*Crack tip coordinate system and schematic for the determination of* $G_{IC} = \partial W/\partial A$.

$$\Delta W = 2\int_0^{r_p}\int_0^{\pi} dW$$

$$= \Delta a \times ks' \times \bar{\epsilon}_{F,\alpha\beta}{}^{n+1}\int_0^{r_p}\left(\frac{\rho^*}{\rho^* + 2r}\right)^{(n+1)/2} dr \tag{5}$$

where

$$s' = \int_0^{\pi} g(\theta) \times [f_{ij}(\theta)]^{n+1}$$

This equation applies to a power law strain hardening material, $\bar{\sigma} = k\bar{\epsilon}^n$, and a strain distribution characterized by the $r^{-1/2}$ singularity. Thus at the onset of fracture the stress and strain distributions are given by

$$\bar{\epsilon}\,(r,\theta) = \epsilon_{F,\alpha\beta}\left(\frac{\rho^*}{\rho^* + 2r}\right)^{1/2} f_{ij}(\theta) \tag{6}$$

$$\bar{\sigma}\,(r,\theta) = k\epsilon^n{}_{F,\alpha\beta}\left(\frac{\rho^*}{\rho^* + 2r}\right)^{n/2} [f_{ij}(\theta)]^n \tag{7}$$

The shape factor s' results from the assumption that the effective strain can be separated into a radial and an angular component as

$$\bar{\epsilon}(r,\theta) = \bar{\epsilon}(r)\Big|_{\theta = 0^\circ} \times f_{ij}(\theta)$$

The radial part of dW can be integrated and yields

$$\frac{\rho^*}{1-n}\left[\left(\frac{\rho^* + 2r_p}{\rho^*}\right)^{(1-n)/2} - 1\right] \quad \text{for } n \neq 1 \tag{8a}$$

$$\frac{\rho^*}{2}\ \ln\frac{\rho^* + 2r_p}{\rho^*} \qquad \text{for } n = 1 \tag{8b}$$

The integrand for $n = 1$, Eq 8*b*, corresponds to the case for a linear strain hardening law. Substituting the plastic zone length

$$r_p = \frac{\rho^*}{2}\left[\left(\frac{\epsilon_{F,\alpha\beta}}{\bar{\epsilon}_Y}\right)^2 - 1\right] \tag{9}$$

we obtain for the fracture resistance of a material following a linear strain hardening law

$$G_{\text{Ic}} = ks'\rho^*\bar{\epsilon}^2{}_{F,\alpha\beta}\ln\frac{\bar{\epsilon}_{F,\alpha\beta}}{\bar{\epsilon}_Y} \tag{10}$$

and for a material following a power law strain hardening

$$G_{\text{Ic}} = \frac{ks'\rho^*}{1-n}\ \bar{\epsilon}_{F,\alpha\beta}^{\,n+1}\left[\left(\frac{\bar{\epsilon}_{F,\alpha\beta}}{\bar{\epsilon}_Y}\right)^{1-n} - 1\right] \tag{11}$$

For a rigid linear strain hardening material following a stress-strain law of the type $\bar{\sigma} = \bar{\sigma}_0 + k\bar{\epsilon}$ we obtain

$$G_{\text{Ic}} = \rho^*\bar{\epsilon}_{F,\alpha\beta}\left[s\bar{\sigma}_0\left(\frac{\bar{\epsilon}_{F,\alpha\beta}}{\bar{\epsilon}_Y} - 1\right) + ks'\bar{\epsilon}_{F,\alpha\beta}\ln\frac{\bar{\epsilon}_{F,\alpha\beta}}{\bar{\epsilon}_Y}\right] \tag{12}$$

and for a rigid power law strain hardening material, following a stress-strain relationship of the type $\bar{\sigma} = \bar{\sigma}_0 + k\ \bar{\epsilon}^n$ we obtain

$$G_{\text{Ic}} = \rho^*\bar{\epsilon}_{F,\alpha\beta}\left[s\bar{\sigma}_0\left(\frac{\bar{\epsilon}_{F,\alpha\beta}}{\bar{\epsilon}_Y} - 1\right) + \frac{ks'}{1-n}\bar{\epsilon}^n{}_{F,\alpha\beta}\left\{\left(\frac{\bar{\epsilon}_{F,\alpha\beta}}{\bar{\epsilon}_Y}\right)^{1-n} - 1\right\}\right] \tag{13}$$

These relationships represent further extension of the original work expressed in Eq 2. The underlying assumption is that the strain hardening exponent contributes only to the stress distribution. This assumption seems appropriate, since the experimental results on measurements of the surface strains suggest that the strain distribution has a $r^{-1/2}$ singularity at the tip even after the general yielding of the specimen, regardless of the value of the strain hardening exponent of the material [17].

It should be noted that, while the form of the expression for the fracture toughness clearly depends on the stress-strain relationship chosen, all expressions derived above are of the type

$$G_{Ic} = s\rho^* \bar{\epsilon}^2_{F,\alpha\beta} \times f(E,k,n,\bar{\epsilon}_Y) \tag{14}$$

provided that n is less than 0.7 and $\bar{\epsilon}_{F,\alpha\beta}$ is large compared to $\bar{\epsilon}_Y$. The dependence of the expression on the strain hardening exponent is illustrated for a sample material in Fig. 3. Figure 3 is based on $E = 30 \times 10^3$ ksi, $k = 200$ ksi, $\bar{\epsilon}_Y = 3.33 \times 10^{-3}$, $\bar{\epsilon}_{F,\alpha\beta} = 0.3$, and $\bar{\sigma}_0 = 100$ ksi. For a material following an exponential strain hardening law and having a yield point intercept the multiplier drops by a factor of approximately 2.5 with increasing n from 0 to $n = 0.5$.

The essential feature is that G_{Ic} is proportional to $\bar{\epsilon}_{F,\alpha\beta}{}^2$, or that K_{Ic} should be proportional to the fracture ductility ahead of the crack tip.

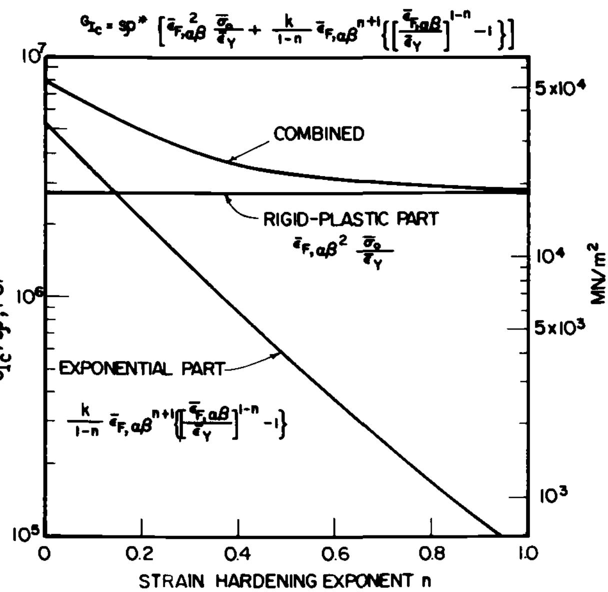

FIG. 3—*Fracture toughness as a function of strain hardening exponent calculated from Eq 11.* s $\simeq$ s′ *is assumed.*

Following the mean stress fracture hypothesis for the effect of stress state on fracture ductility, this proportionality should also be maintained for the plane-strain fracture toughness and the bulge ductility. In this connection it should perhaps be noted that the stress state ahead of the crack tip may also depend on the strain hardening exponent. From slip line field theory [*18*], for a rigid plastic material, we obtain $\alpha = 0.806$ and $\beta = 0.611$. Hutchinson's analytical results [*19*] suggest that for a strain hardening material the stress state α and β may be approximated by

$$\alpha = 0.387\, n + 0.806$$

$$\beta = 0.762\, n + 0.611 \qquad (15)$$

which may be valid up to $n \sim 0.35$. Nevertheless, for similar classes of materials for which the n value does not vary significantly, again the proportionality between plane-strain fracture toughness and the bulge ductility should be maintained. The factors discussed here merely change the proportionality constant. In view of the complexity of these relationships, however, the proportionality constants have to be determined experimentally at this time.

Experimental Studies

The bulge ductility is considered to offer the most promising measure of the material ductility to correlate with its fracture toughness. The reason for this is, that for most technical materials of medium and high strength, fracture in the bulge test occurs prior to the onset of necking or instability. Bulge testing is relatively simple. A variety of bulge test configurations have been utilized in this program, as illustrated in Fig. 4. These are the hydraulic bulge tests, Fig. 4*a*, the bulge test on a specimen geometry suggested by Azrin and Backofen [*20*], Fig. 4*b*, and a further modification of the Azrin-Backofen geometry recently developed at Syracuse University, Fig. 4*c*. While the hydraulic bulge test is not strictly speaking equibiaxial tension, due to the presence of a third compressive stress in the direction normal to the inside surface of the specimen, geometries illustrated in Fig. 4*b* and *c* result in a truly equibiaxial tension loading. The effective fracture strain is simply determined from a thickness measurement and given by

$$\bar{\epsilon}_{F,\alpha = 1,\, \beta = 0} = \ln \frac{t_o}{t_f} \qquad (16)$$

Plane-strain fracture toughness tests were conducted in accordance with ASTM Test for Plane-Strain Fracture Toughness of Metallic Materials (E 399-74) on the same materials on which the bulge tests were conducted. These materials include 300M steel, D6AC steel, and 250-

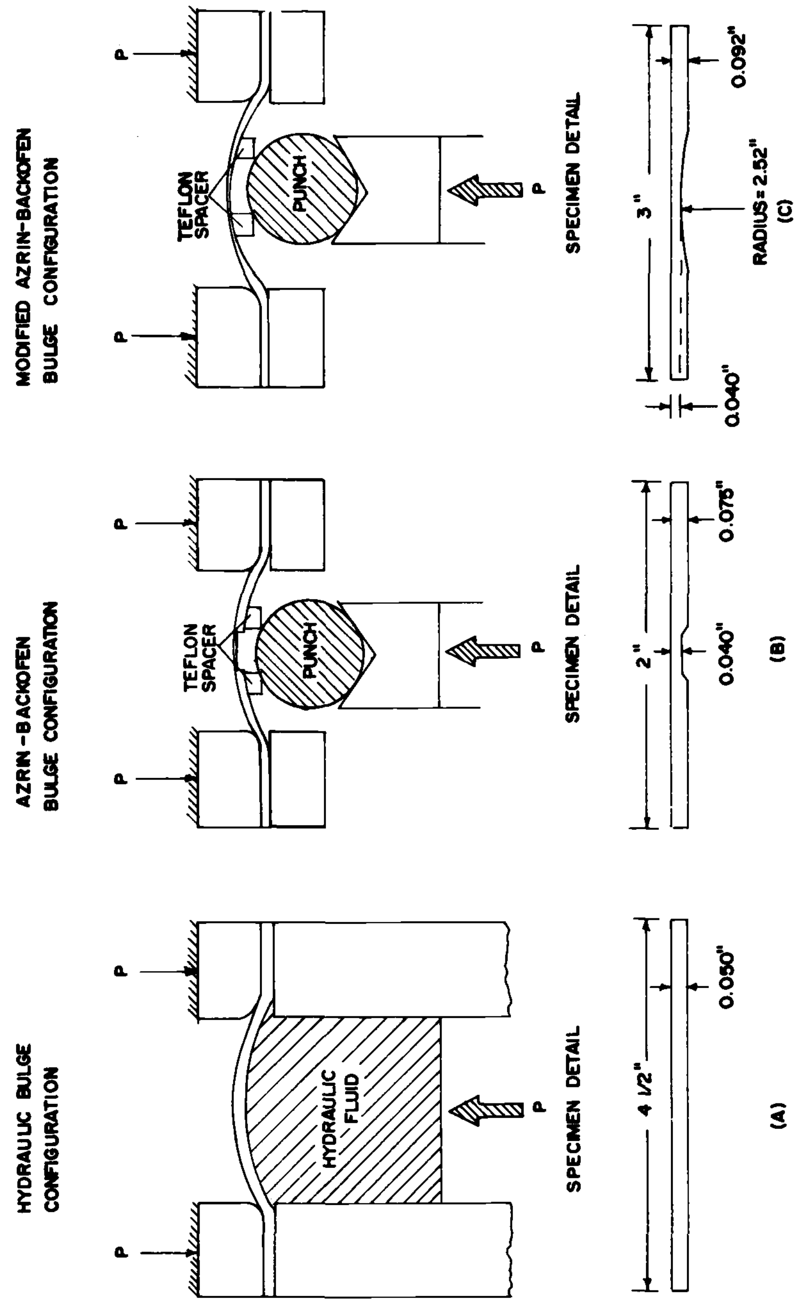

FIG. 4—Bulge fixtures for equibiaxial ductility test.

grade maraging steel, all heat treated to several strength levels. The experimental results in the form of plane-strain fracture toughness versus effective fracture strain as determined from the bulge tests are plotted in Fig. 5 which includes the data reported earlier [15]. The correlations may be expressed as

$$K_{Ic} = 147.2 \times \bar{\epsilon}_{F,\alpha = 1,\ \beta = 0}\ \text{ksi}\sqrt{\text{in.}}$$

or

$$K_{Ic} = 161.7 \times \bar{\epsilon}_{F,\alpha = 1,\ \beta = 0}\ \text{MN} \times \text{m}^{-3/2}$$

The scatter is approximately 30 percent, as indicated in Fig. 5 by the dashed lines.

The experimental confirmation of the linear relationship between fracture toughness or fracture resistance and fracture ductility made it possible to consider the effect of specimen thickness [15]. In order to do

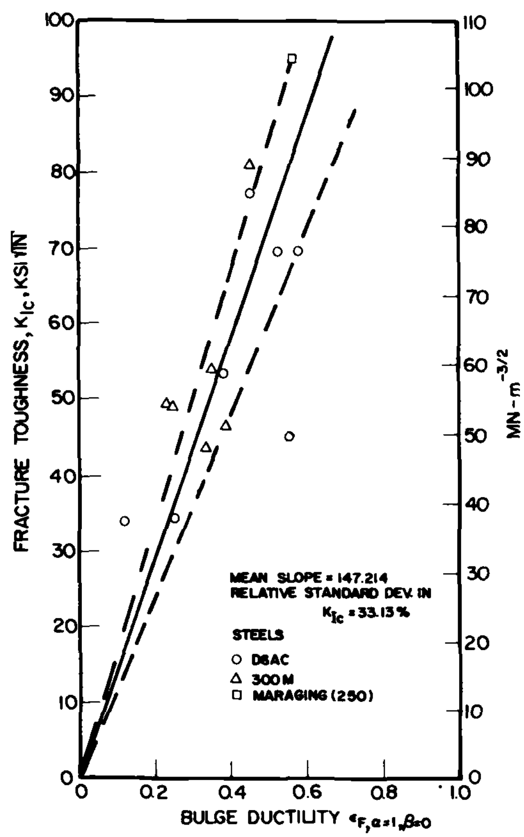

FIG. 5—*Correlation between plane-strain fracture toughness and hydraulic bulge ductility for steels.*

this it is necessary to assume a relationship for the transition of the stress state from plane stress at the specimen surface to plane strain in the interior. Based on previous studies it was suggested to keep β constant at 0.61 and to express α as

$$\alpha = \frac{0.81}{4r_p} \frac{z}{\left\{1 + \left(\frac{z}{4r_p}\right)^4\right\}^{1/4}} \tag{17}$$

where z is the distance below the specimen surface. This relationship is illustrated in Fig. 6. Accordingly, plane strain is nearly reached at a distance four times the plastic zone size below the specimen surface. The fracture toughness for such a specimen is computed as the average along the entire crack front, that is

$$\bar{G}_R = \frac{2}{t}\int_0^{t/2} G_R(z)\, dz \tag{18}$$

where G_R represents the local fracture resistance characterized by the local stress state, namely, $G_R(z)\ \alpha\, \bar{\epsilon}_{F,\alpha\beta}{}^2(z)$. Utilizing G_{Ic}, the plane-strain fracture toughness, the ductility term can be eliminated and one obtains for the thickness effect

$$\bar{G}_R = \frac{G_{\mathrm{Ic}}}{(1-\nu^2)\,(0.279)^2} \times \frac{2}{t}\int_0^{t/2} (2wm)^2\, dz \tag{19}$$

Equation 19 is based on the simplified assumption that $n = 1$. Figure 7 shows the predicted K_c versus thickness curves for 7075 aluminum alloy together with the experimental data reported by Kaufmann [22]. Excellent agreement between the experimental and the predicted data is obtained for a choice of $K_{\mathrm{Ic}} = 26$ ksi$\sqrt{\text{in.}}$

Microstructural Consideration

Because of the strong correlations between fracture toughness and ductility it is logical to explore the microstructural events that control the ductility. The dominant features on the fracture surfaces of structural metallic materials are dimples which have been associated with a fracture process due to "void coalescence" [23-26]. For a number of two-dimensional void growth models McClintock obtained an expression for

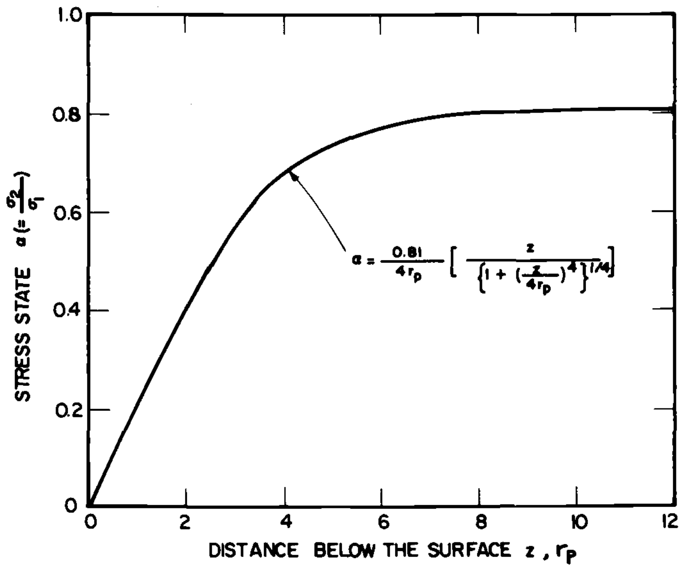

FIG. 6—*Distribution of stress ratio ($\alpha = \sigma_2/\sigma_1$) along the crack tip as a function of the distance (z) below the specimen surface, calculated based on Eq 17.*

the fracture ductility

$$\bar{\epsilon}_{V_f}{}^{\infty} = \frac{(1-n)\ln V_f^{-1/3}}{\sinh[(1-n)(\sigma_1+\sigma_2)/2\bar{\sigma}/\sqrt{3}]} \tag{20}$$

where

V_f = volume fraction of the voids
σ_1 and σ_2 = stresses
n = strain hardening exponent, and
$\bar{\sigma}$ = flow stress. From this relationship, one obtains for the fracture strain ratio

$$\frac{\bar{\epsilon}_{c,\alpha}}{\bar{\epsilon}_{c,o}} = \frac{\sinh[(1-n)\sqrt{3/2}]}{\sinh[(1-n)(\sqrt{3/2})(\alpha+1)/\sqrt{\alpha^2-(\alpha+1)}]} \tag{21}$$

which is plotted in comparison with the predictions of the volume strain criterion in Fig. 8. The trends of the two models are the same; however, the McClintock model predicts a much smaller effect of decreasing n value than the mean stress model. Experimental data show a sharper decrease of fracture ductility than would be possible in accordance with the hole growth model even for n towards zero. Similar arguments and experimental results have led Broek [26] to propose a relationship between plane-strain fracture toughness and volume fraction. Thomason [27] utilizing an internal necking criterion, has also derived a set of equations relating the plane-strain toughness to the void concentration. Low and Cox [25] were able to demonstrate experimentally two different modes of void coalescence, the classical mode resulting in the dimples, and a mode characterized as void sheet linking of large inclusion nucleated voids separated by several multiples of their individual void diameters. The former process, classical void coalescence, is typically noted in maraging steel, while void sheet linking is noted in quenched and tempered AISI 4340 steel. It is suggested that this second process leads to a lower fracture toughness.

While complete analytical relationships for these microstructural coalescence processes are not available, it may be assumed that the relationships illustrated in Fig. 9 represent a fair approximation. Also, Fig. 9 indicates that the coalescence strain is not temperature sensitive except as the strain hardening exponent, n, may depend on the tempera-

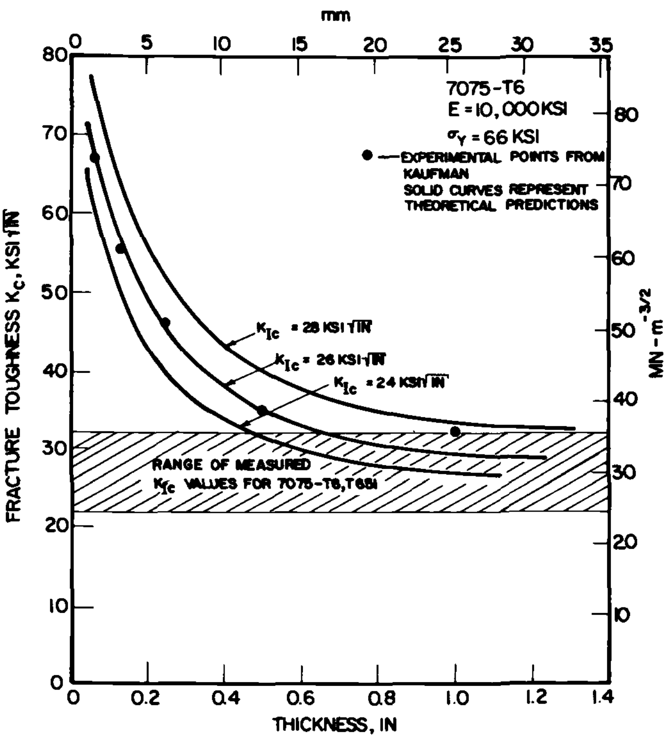

FIG. 7—*Experimental data and theoretical curves calculated according to Eq 19 for Al 7075-T6 and -T651.*

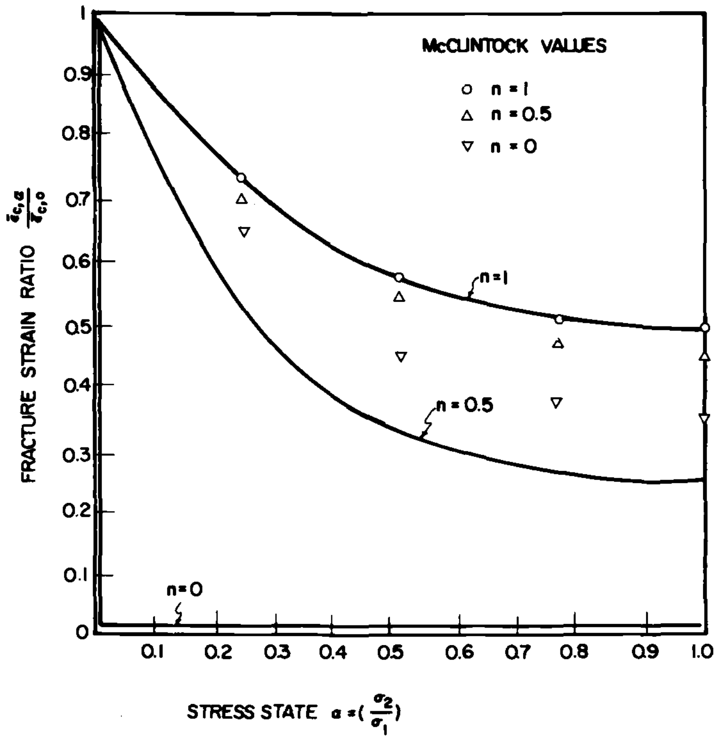

FIG. 8—*Comparison of fracture strain ratios predicted from the McClintock's hole growth model and the mean stress criterion* (solid curves).

ture (which is certainly the case for face-centered-cubic (fcc) aluminum alloys). Conversely for body-centered-cubic (bcc) materials such as structural steel the coalescence strain may be considered independent of temperature and primarily related to the stress state and the volume fraction of voids. The latter is related to the void nucleation phase. It must be assumed that the voids are nucleated during the deformation process itself. Such void nucleation could occur at inclusions and grain boundaries. Typical processes are the fracturing of a brittle inclusion or the decohesion of the inclusion-matrix interface. For the latter Argon et al *[28]* have found that the interface stress normal to the inclusion-matrix interface is given by

$$\sigma_{rr} = Y(\bar{\epsilon}^p) + \sigma_m \qquad (22)$$

where

$Y(\bar{\epsilon}^p)$ = flow stress in the region of the inclusion and
σ_m = mean stress (or negative pressure component).

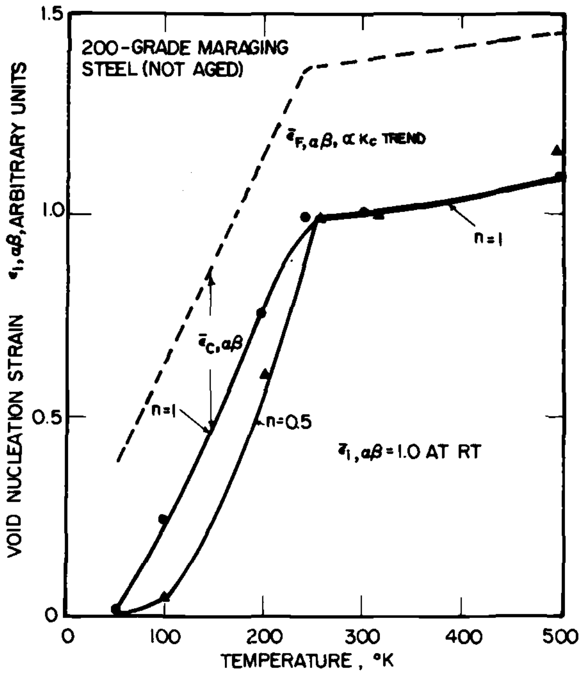

FIG. 9—*Schematic of the strain required for void nucleation as a function of temperature in unaged 200-grade maraging steel.*

Experimental determinations [29] of σ_{rr} yield for

TiC inclusions in unaged maraging steel ($Y \simeq 195$ ksi)	$\sigma_{rr} \simeq$	264 ksi
Cu-Cr inclusions in copper ($Y \simeq 70$ ksi)	$\sigma_{rr} \simeq$	144 ksi
Fe_cC particles in spherodized 1045 steel ($Y \simeq 125$ ksi)	$\sigma_{rr} \simeq$	242 ksi

These values are between 0.008 E and 0.009 E.

Equation 22 indicates that the critical mean stress required for void nucleation varies with temperature as

$$\sigma_m = \sigma_{rr} - Y(\bar{\epsilon}^p, T) \tag{23}$$

If σ_{rr} increases only moderately with decreasing temperature (like Young's modulus), much less than the yield strength, then the mean stress required for void nucleation may decrease rapidly in a critical temperature range, thus providing an explanation for the ductility transition phenomenon. For $\bar{\sigma} = K\bar{\epsilon}^n = 3\sigma_m \times f(\alpha,\beta)$ the strain for void nucleation becomes a function of σ_m only, if the stress state (α,β) remains the same. Figure 9 shows computed values of the void nucleation strain, $\bar{\epsilon}_{i,\alpha\beta}$, as a function of test temperature for maraging steel ($\sigma_Y = 200$ ksi at room temperature) in the unaged condition. σ_{rr} was assumed to vary with temperature in the same ratio as Young's modulus. The *Y(T)* curve for maraging steel was available from a prior study. Since it is only possible to calculate ratios a room temperature value of $\bar{\epsilon}_{i,\alpha\beta} = 1$ was assumed as reference.

An examination of Eq 20 indicates that, for a given material and constant stress state, the strain required for void coalescence is nearly constant and independent of test temperature. The principal influence is the void density V_f (or $2b/1$). For typical materials one might expect a coalescence strain of between 0.01 and 0.5 for the stress ahead of a crack. These strains are additive, that is

$$\bar{\epsilon}_{F,\alpha\beta} = \bar{\epsilon}_{i,\alpha\beta} + \bar{\epsilon}_{c,\alpha\beta} \tag{24}$$

and hence the fracture strain versus temperature curve will be parallel to the void nucleation strain versus temperature curve, displaced upwards by a constant amount, $\bar{\epsilon}_{c,\alpha\beta}$. Finally, because of the already discussed linear correlation between fracture strain and fracture toughness, a fracture toughness versus test temperature curve is obtained which is proportional to the $\epsilon_{F,\alpha\beta} - T$ curve.

Thus, as a first step, a connection between microstructure and fracture toughness of the form

$$K_{c,\alpha\beta} = [\bar{\epsilon}_{i,\alpha\beta}\{\sigma_{rr} - Y(\bar{\epsilon}^p,T,n)\} + \bar{\epsilon}_{c,\alpha\beta}(V_f,n)]E\sqrt{s\rho^*/\alpha'} \tag{25}$$

is proposed. This synthesis suggests that the temperature dependence of ductility and fracture toughness arises in the void nucleation phase. The ease of void nucleation depends primarily on the inclusion—matrix interface strength and the amount by which it exceeds the flow stress. The inclusion density affects primarily the strain required for void coalescence. Both components of the fracture strain, $\bar{\epsilon}_i$ and $\bar{\epsilon}_c$, are strong functions of the stress state, (α,β), and decrease with increasing stress triaxiality. In fcc materials the yield strength is not a very strong function of temperature; however, the strain hardening exponent n is. As n increases with decreasing test temperature the initiation and coalescence strains increase. This might offset to some extent the $(\sigma_{rr} - Y)$ effect and thus produce a much weaker fracture toughness transition with decreasing temperature than observed in bcc materials.

At present the character of the proposed correlations is largely qualitative. However, some quantitative information, such as values of σ_{rr} and the $K_{Ic} - \bar{\epsilon}_{F,\alpha=1,\beta=0}$ relation for steels, is already available. Further development of reliable quantitative relationships of the type suggested here should be strongly encouraged; they would aid considerably in materials development and also in the development of fracture toughness tests that do not require the difficult and expensive procedures now necessary for typical medium-strength high-toughness materials.

Acknowledgment

This work was supported by the U.S. Navy Air Systems Command, under Contracts No. N-62269-73-C-0261 and N-00019-75-C-0065. The authors wish to thank Dr. M. Sengupta for his great contribution in the early stage of this study and C. Chave for his help in conducting tests.

References

[1] Krafft, J. M., *Applied Materials Research*, Vol. 3, 1964, pp. 88-101.
[2] For example, Hahn, G. T. and Rosenfield, A. R. in *Applications Related Phenomena in Titanium Alloys, ASTM STP 432*, American Society for Testing and Materials, 1968, pp. 5-32.
[3] Bridgeman, P. W., *Studies in Large Plastic Flow and Fracture*, Harvard University Press, Cambridge, Mass., 1964.
[4] Weiss, V., Sanford, W., and Liu, K., unpublished work at Syracuse University, Syracuse, N.Y., 1974.
[5] Allen, F. C. in *Damage Tolerance in Aircraft Structures, ASTM STP 486*, American Society for Testing and Materials, 1971, pp. 16-38.
[6] Clausing, D. P., *International Journal of Fracture Mechanics*, Vol. 6, 1970, pp. 71-85.
[7] Barsom, J. M. and Pellegrino, J. V., *Engineering Fracture Mechanics*, Vol. 5, 1973, pp. 209-221.
[8] Sailors, R. H., T&AM Report, No. 367, Illinois University, Urbana, Ill., 1973.
[9] Weiss, V. in *Mechanical Behavior of Materials*, Proceedings of the 1971 International Conference on Mechanical Behavior of Materials, The Society of Materials Science, Japan, Vol. 1, 1972, pp. 458-474.
[10] Weiss, V., Ahuja, R. K., Sheu, J. L., and Sessler, J. G., Final Report to Department of the Navy, MET-VW-1810-F1170, Syracuse University, Syracuse, N.Y., 1970.
[11] Yajima, M., Ishii, M., and Kobayashi, M., *International Journal of Fracture Mechanics*, Vol. 6, 1970, pp. 139-150.
[12] French, I. E., Weinrich, P. F., and Weaver, C. W., *Acta Metallurgica*, Vol. 21, 1973, pp. 1045-1049.
[13] French, I. E. and Weinrich, P. F., *Acta Metallurgica*, Vol. 21, 1973, pp. 1533-1537.
[14] French, I. E. and Weinrich, P. F., *Metallurgical Transactions*, Vol. 6A, 1975.
[15] Weiss, V. and Sengupta, M. in *Mechanics of Crack Growth, ASTM STP 590*, American Society for Testing and Materials, 1976, pp. 194-207.
[16] Sengupta, M., Ph.D. dissertation, Syracuse University, Syracuse, N.Y., 1974.
[17] Ogasawara, M., Adachi, M., Nagao, M., and Weiss, V. in *Mechanical Behavior of Materials*, Proceedings of the 1973 Symposium on Mechanical Behavior of Materials, The Society of Materials Science, Japan, 1974, pp. 159-176.
[18] Hill, R., *Mathematical Theory of Plasticity*, Clarendon Press, Oxford, England, 1950.
[19] Hutchinson, J. W., *Journal of the Mechanics and Physics of Solids*, Vol. 16, 1968, pp. 13-31.
[20] Azrin, M. and Backofen, W. A., *Metallurgical Transactions*, Vol. 1, 1970, pp. 2857-2865.
[21] Weiss, V. in *Fracture—An Advanced Treatise*, Vol. 3, H. Liebowitz, Ed., Academic Press, New York, 1971, Chapter 3, pp. 227-264.
[22] Kaufmann, J. G. in *Review of Developments in Plane Strain Fracture Toughness Testing, ASTM STP 463*, American Society for Testing and Materials, 1970, pp. 3-21.
[23] McClintock, F. A., *Journal of Applied Mechanics, Transactions*, American Society of Mechanical Engineers, Series E, Vol. 35, 1968, pp. 363-371.
[24] Broek, D., NLR TR 710214 U, National Aerospace Laboratory, The Netherlands, 1971.
[25] Cox, T. B. and Low, J. R., Jr., NASA Technical Report No. 5, Carnegie-Mellon University, Pittsburgh, Pa., 1973.

[26] Broek, D., *Engineering Fracture Mechanics*, Vol. 5, 1973, pp. 55-66.
[27] Thomason, P. F., *International Journal of Fracture Mechanics*, Vol. 7, 1971, pp. 409-419.
[28] Argon, A. S., Im, J., and Safoglu, R., *Metallurgical Transactions*, Vol. 6A, 1975, pp. 825-837.
[29] Argon, A. S. and Im, J., *Metallurgical Transactions*, Vol. 6A, 1975, pp. 839-851.

R. H. Sailors[1]

Relationship Between Tensile Properties and Microscopically Ductile Plane-Strain Fracture Toughness

REFERENCE: Sailors, R. H., "**Relationship Between Tensile Properties and Microscopically Ductile Plane-Strain Fracture Toughness,**" *Properties Related to Fracture Toughness, ASTM STP 605,* American Society for Testing and Materials, 1976, pp. 34–61.

ABSTRACT: An equation has been derived which will permit plane-strain fracture toughness, K_{Ic}, to be calculated from a knowledge of uniaxial tensile properties. After corrections for constraint and strain hardening the plane-stress rigid plastic crack opening displacement expression was found to describe accurately experimental crack opening displacement for the plane-strain condition. The crack tip strain distribution was measured and found to be compatible with an r^{-1} strain distribution within a small region ahead of the crack tip. A length parameter was identified and shown to be proportional to mean-free ferrite path in steels. From the proposed behavior of crack tip instability, it was possible to better understand the observed trend of decreasing fracture toughness with increasing yield strength and how this trend can be altered by control of the microstructure.

KEY WORDS: fracture properties, fracturing, toughness, microstructure, tensile properties, ductility, mechanical properties, fracture strength

Numerous references illustrate that fracture toughness, K_{Ic} or G_{Ic}, increases with either or a combination of decreasing yield strength, Y, increasing true fracture strain, ϵ_{ct}, and increasing strain hardening exponent, n [*1-6*].[2] Despite qualitative trends and attempts to become quantitative [*5-9*], there still does not exist an undisputed basic understanding of how fracture toughness and tensile properties are related, even for a single class of materials. It is the purpose of this paper to review recent

[1] Formerly, research assistant, Department of Theoretical and Applied Mechanics, University of Illinois, Urbana, Ill.; presently, materials development engineer, Bucyrus-Erie Co., South Milwaukee, Wis. 53172.

[2] The italic numbers in brackets refer to the list of references appended to this paper.

developments in understanding near crack tip behavior and attempt to formulate an expression between tensile properties and fracture toughness for steels that is simple, accurate, and based on undisputed principles.

A simple notch tip analysis illustrates in concept that the critical strain energy release rate, G_c, is the product of notch tip flow stress, Y_E, times the additional opening of the notch to instability, δ. The additional notch opening, δ, arises from a crack tip plastic strain of $\bar{\epsilon}_p$ acting over a gage length 2 ρ, where ρ is the notch root radius. Thus, the critical strain energy release rate, G_c, becomes

$$G_c = Y_E \, 2\rho\bar{\epsilon}_p \tag{1}$$

For the case of an actual crack, ρ, as presently defined, tends to zero and of course needs redefinition. Thus, 2ρ is simply referred to as a length parameter. The effective flow stress, Y_E, and crack tip strain, $\bar{\epsilon}_p$, both must account for the multiaxial nature of the crack tip.

Recent developments in near crack tip behavior show a stress times strain singularity in terms of r, the polar coordinate, as the crack tip is approached [*10,11*]. In the elastic region of the crack tip such a singularity results by simply multiplying the linear elastic crack tip field expressions for stress and strain. The strength of the singularity is G, the strain energy release rate. However, for the plastic region, the same form of singularity has not been obtained in closed form. Rice and Johnson [*12*] described a "region of intense strain" and showed that for circular crack tip blunting it extended ahead of the crack approximately two times the crack opening displacement. Within the region of intense strain an approximate r^{-1} strain singularity was demonstrated. Figure 1 illustrates growth of the region of intense strain until it envelopes a void initiating particle after which void coalescence with the crack tip rapidly occurs. Crack tip blunting occurs under the biaxial stress state and is recorded on fracture surfaces at the fatigue crack-fast fracture interface as the "stretched zone" which is also indicated in Fig. 1.

Practical implications of the recent work on near crack tip behavior have emphasized new and more manageable ways of measuring fracture toughness of low strength-high toughness materials [*13*]. However, important to the problem at hand are the implications concerning the description of crack tip flow and fracture from the materials point of view. For instance, the crack tip stress state or states of importance must be identified before attempts are made to measure the material property fracture strain. Realistic values must be assigned to the crack tip material property flow stress, and finally microstructural entities which participate in void initiation must be recognized. The present investigation used the recent work on near crack tip behavior as a guide

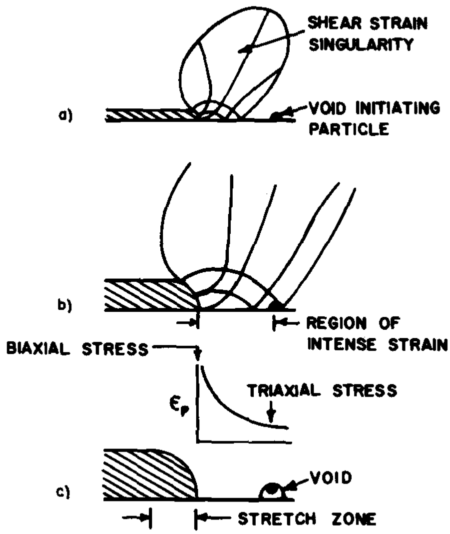

FIG. 1—*Proposed crack tip behavior after Rice et al* [12]. (a) *Start of crack tip blunting.* (b) *Region of intense strain reacts with void initiating particle.* (c) *Void forms, under triaxial stress, at strain value much lower than that which exists at the physical crack tip.*

and attempted to determine experimentally the critical values of crack tip flow stress, plastic strain distribution, and length parameter. A crack tip model is proposed which, by recognizing microstructural features, permits plane-strain fracture toughness to be calculated from tensile properties. Although the model is demonstrated to be accurate for only low- and medium-strength steels, the principles derived are expected to apply to other alloy systems as well.

Materials

The three materials chosen for this investigation were air-melted low-alloy plate steels having the compositions and mechanical properties given in Table 1. The two highest strength steels were water quenched and tempered (tempered martensite), and the lowest strength steel was hot rolled (ferrite and pearlite). All mechanical tests were performed so that the fracture plane was through the thickness and parallel to the rolling direction (T-L orientation). In the interests of generality, materials were purposely chosen to have a wide range in mechanical properties.

Flow Stress from Crack Opening Displacement

Analytical relationships between crack opening displacement (COD or δ) and other crack tip quantities have been derived only for rigid-plastic material behavior under plane-stress conditions as shown in Table 2 [*14-17*]. Numerical analysis of the crack tip region taking into account constraint and strain hardening showed similar relationships to that for the rigid-plastic situation with the exception of modifying coefficients such as listed in Table 2 [*10,12,18,19*]. The varying coefficients reflect the particular numerical method used to derive the equation as well as effects of constraint and strain hardening. Therefore, the following equation was accepted in form only as representative of the relationship between COD and stress intensity.

$$\frac{\delta}{e_y} = \left(\frac{K}{Y}\right)^2 \tag{2}$$

where

δ = crack opening displacement;
$e_y = Y/E$: Y = yield strength, E = elastic modulus; and
K = stress intensity factor.

To modify this expression for work-hardening plane-strain conditions, it is necessary to insert some effective value of flow stress, Y_E, which will be larger than Y. As a first approximation assume that multiplicative factors, one for constraint, C, and one for hardening, H, will adequately describe Y_E (that is, $Y_E = CHY$). Thus, the COD expression (Eq 2) becomes

$$\frac{\delta}{e_y} = \frac{1}{CH}\left(\frac{K}{Y}\right)^2 \tag{3}$$

TABLE 1—*Composition and mechanical properties of steels investigated (T-L orientation).*

Steel Designation	C	Mn	P	S	Si	Ni	Cr	Mo	Cu	Al	B
1 EAFD	0.17	1.06	0.009	0.019	0.23	0.01	0.40	0.29	0.03	0.02	0.0006
1 EAEG	0.19	1.14	0.008	0.013	0.26	0.02	0.51	0.30	0.01	0.024	0.0016
1 E170	0.15	1.03	0.018	0.017	0.19	0.025	0.03	0.01	0.02	0.037	. . .

Steel Designation	Ultimate Strength		Yield Strength		Reduction of Area, %	(ϵ_{fl})	n	G_{IC}	
	ksi	MPa	ksi	MPa				$\frac{\text{in} \cdot \text{lb}}{\text{in.}^2}$	$\frac{J}{M^2}$
1 EAFD	171	1179	161	1110	42	(0.55)	0.04	162	2.84×10^4
1 EAEG	121	834	106	731	56	(0.82)	0.07	246	4.31×10^4
1 E170	67	462	41	283	63	(1.00)	0.20	470	8.23×10^4

TABLE 2—*Chronological list of analytically and numerically derived equations for COD.*

Investigator		Procedure[a]	Equation	Stress State	Hardening
Wells	1962	A	$\delta/e_y = \frac{4}{\pi}(K/Y)^2$	plane stress	no
Goodier and Field	1963	A	$\delta/e_y = (K/Y)^2$	plane stress	no
Bilby et al	1964	A	$\delta/e_y = (1 + \nu)(K/Y)^2$	plane stress	no
Rice	1965	A	$\delta/e_y = (K/Y)^2$	plane stress	no
Rice and Rosengren	1968	N	$\delta/e_y = (K/Y)^2$	plane strain	yes
Wells	1969	FE	$\delta/e_y = (K/Y)^2$	plane strain	no
Rice and Johnson	1970	N	$\delta/e_y = (0.625 \text{ to } 0.707)(K/Y)^2$	plane strain	no
Levy et al	1971	FE	$\delta/e_y = 0.425(K/Y)^2$	plane strain	no

[a] A = analytical.
N = numerical other than finite element.
FE = finite element.

As a first approximation, the constraint factor, C, should remain constant and represent the average elevation of yield strength due to the multiaxial stress state. The strain-hardening factor, H, should vary with the strain-hardening exponent, n, and approach 1 as yield strength becomes large (rigid-plastic behavior). In effect, H is a multiplier of the yield strength which takes the work-hardening stress-strain curve and makes it a rigid-plastic stress-strain curve.

A limited amount of COD data was available on a 36 and 110-ksi yield strength steel [6,20], so measurements reported here are limited to the 160-ksi yield strength level. COD measurements were made from photographs of surface traces of cracks in 1-in. compact specimens. Compact specimens were loaded according to ASTM (E 399-72) Test for Plane-Strain Fracture Toughness of Metallic Materials. The loading was interrupted far short of crack instability, however, and a wedge was inserted in-line with the load and thereafter supported the specimen deflection. Figure 2 illustrates the load-deflection record during this procedure. The specimen was then removed from the test fixture and placed in its entirety in a scanning electron microscope (SEM), and the surface crack tip profile was examined at magnifications up to ×2000. Measurements of COD were made on the photographs back of the crack tip blunted region. After photographs of both crack tip surface traces were taken, the specimen was returned to the testing machine where a higher load was applied, and, consequently a thicker wedge inserted. The specimen was returned to the SEM, and the crack tip surface traces were again photographed. Figure 3 shows, photographically, a series of five such

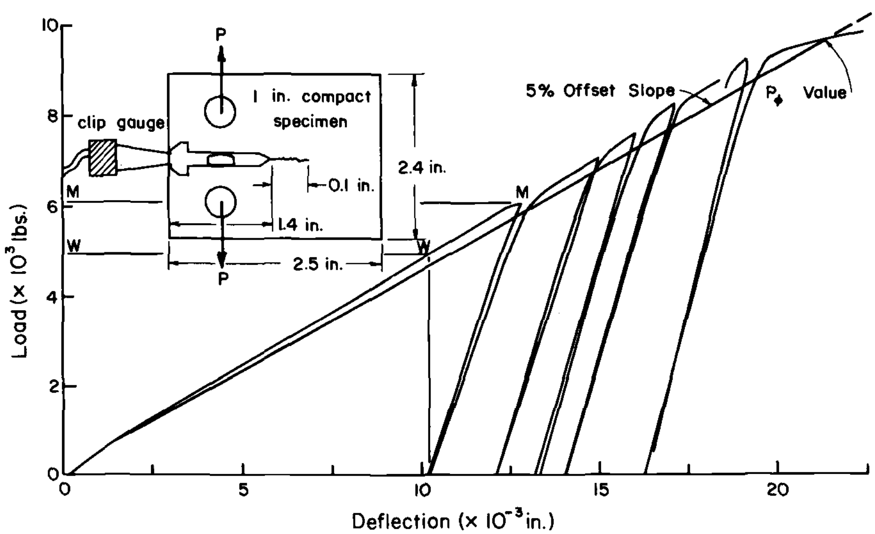

FIG. 2—*Load-deflection record illustrating COD measurement technique.*

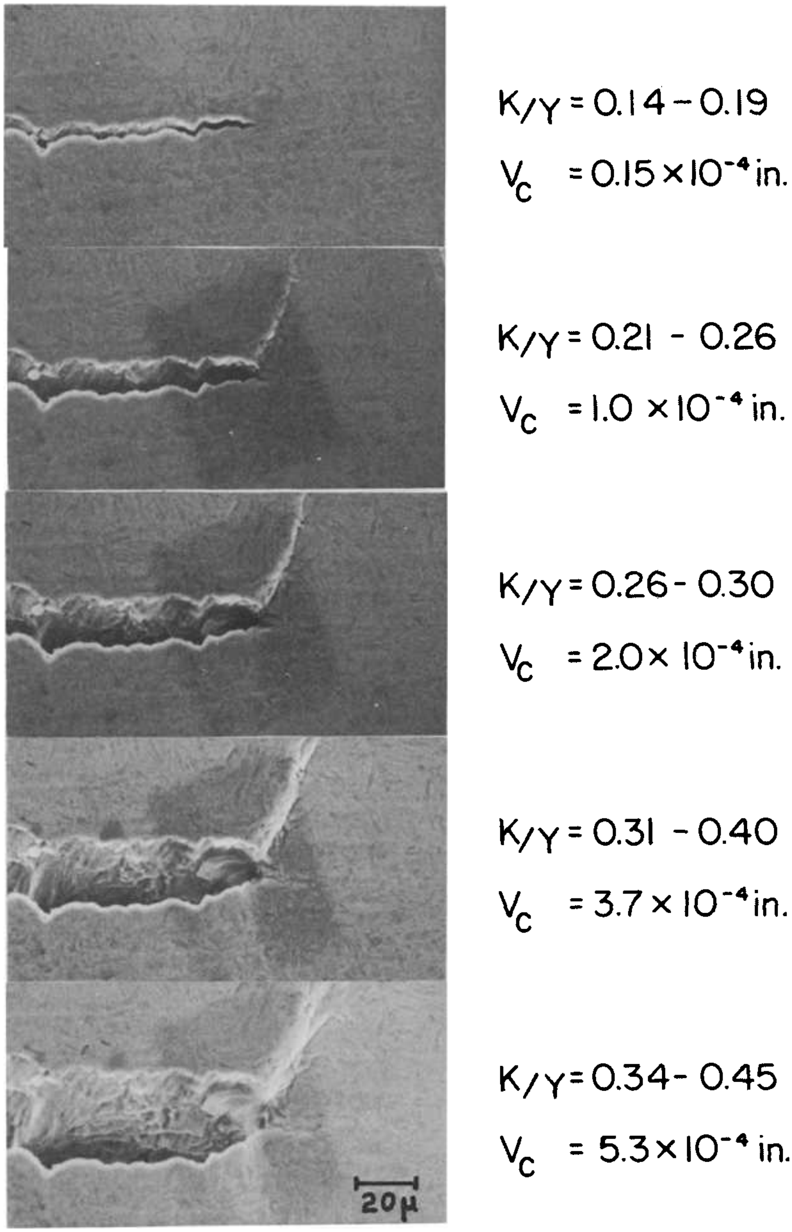

FIG. 3—*Photographs illustrating COD on specimen surface as crack tip stress intensity increases.*

loadings with corresponding stress intensity and COD values. A range of stress intensity is reported for each COD measurement which corresponds to the load from the machine (*M* in Fig. 2) down to the estimated load on the wedge (*W* on Fig. 2).

Data from the three widely different strength levels are shown in Fig. 4 as δ/e_y versus K/Y and illustrates that as strain-hardening effects become greater (that is, lower yield strength), the relationship between COD, stress intensity, and yield strength deviates more from the plane-stress, rigid-plastic form of Eq 3. A diagram of the quantity CH from Eq 3 (that is, (intercept)$^{-1}$ at $K/Y = 1$) versus yield strength as shown in Fig. 5 better illustrates the effect of strain hardening. Connecting the data points by a smooth curve and acknowledging negligible strain hardening above $\simeq$200 ksi ($H = 1$) suggested a value of 1.3 for C. Dividing out the value of C left the various values of H to be accounted for.

The method chosen to account for H consisted of constructing a rigid-plastic σ-ϵ curve from the actual work-hardening σ-ϵ curve. The

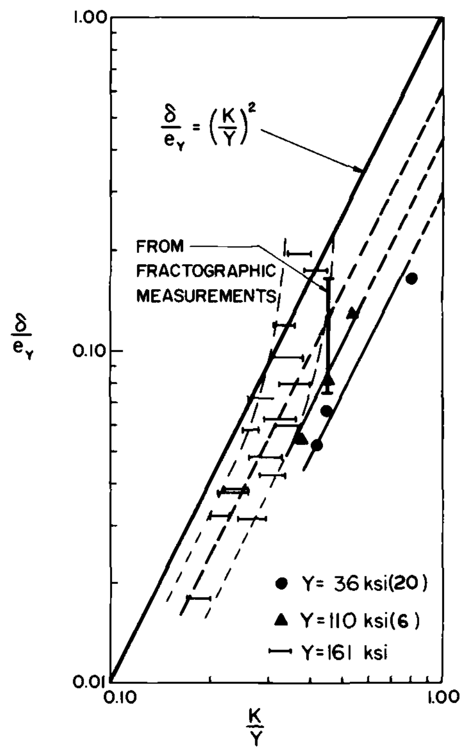

FIG. 4—*Crack opening displacement uncorrected for constraint and strain hardening as a function of stress intensity.*

subscripts H_1 and H_3, for instance, in Fig. 6*a* indicate values of flow stress obtained by equating areas under the actual and rigid-plastic σ-ϵ curves out to the instability strain ($\epsilon_p = n$) and fracture strain ($\epsilon_p = \epsilon_{ft}$), respectively. Figure 6*b* compares these and other values of H_1 against needed corrections (that is, $Y_{H1} = H_1Y$) and indicates that H_3 is the best choice to describe the strain-hardening correction needed. Thus, for the data available the strain-hardening correction term was chosen as

$$H = \frac{1}{n+1}\left(\frac{\epsilon_{ft}}{0.002}\right)^n \tag{4}$$

COD data replotted with $C = 1.3$ and H defined by Eq 4, as shown in Fig. 7, all fall into a reasonably small scatterband. Values of H vary from 1.2 for $Y = 160$ ksi up to 2.8 for $Y \simeq 40$ ksi. Thus, as defined here, the strain-hardening correction can hardly be neglected. Extrapolating the data out to crack instability leads to the following equation.

$$G_{Ic} \simeq \frac{K_{Ic}{}^2}{E} = CH\,\delta_{Ic} \tag{5}$$

The subscript Ic refers to mode I fracture instability.

Crack Tip Strain Distribution

Although the crack tip strain distribution has been predicted within the region of intense strain, experimental verification is lacking. The biaxial

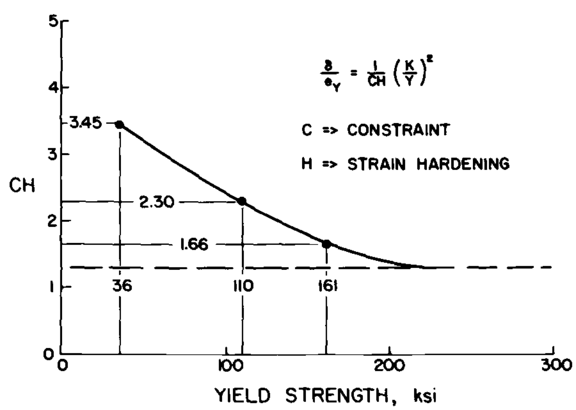

FIG. 5—*Effect of yield strength on values of strain hardening correction needed.*

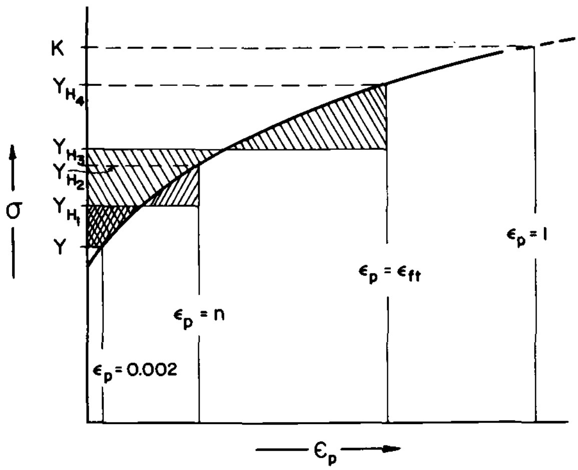

FIG. 6 *a—Construction of rigid-plastic stress-strain curve from actual work-hardening stress-strain curve.*

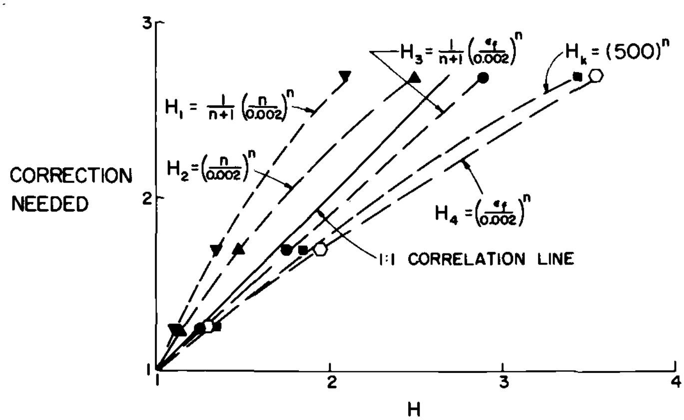

FIG. 6*b—Comparison of strain-hardening correction needed versus calculated stress.*

stress state which exists on the blunted crack tip can be duplicated macroscopically by the plane-strain ductility specimen first suggested and used by Clausing [*21*]. Triaxial stresses which exist at the inner boundary of the region of intense strain, can be approximated by the specimen shown in Fig. 8. A simplified stress analysis yielded the principal stresses given in Fig. 8 [*22*], which agree on the average with a more detailed and sophisticated stress analysis by Merkle [*23*].

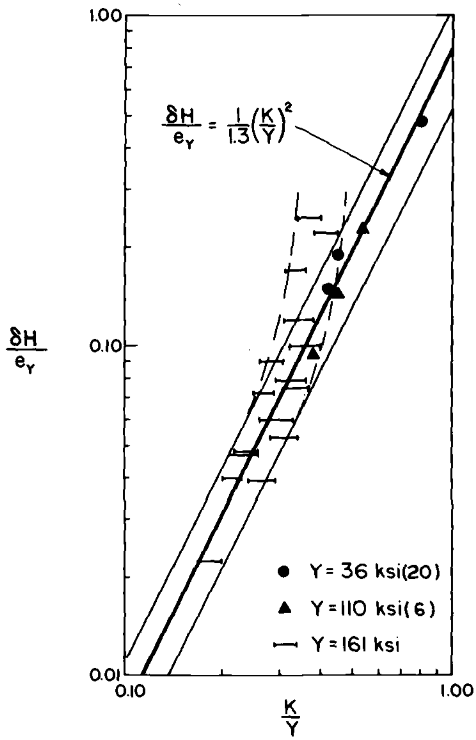

FIG. 7—*Crack opening displacement corrected for constraint and strain hardening as a function of stress intensity.*

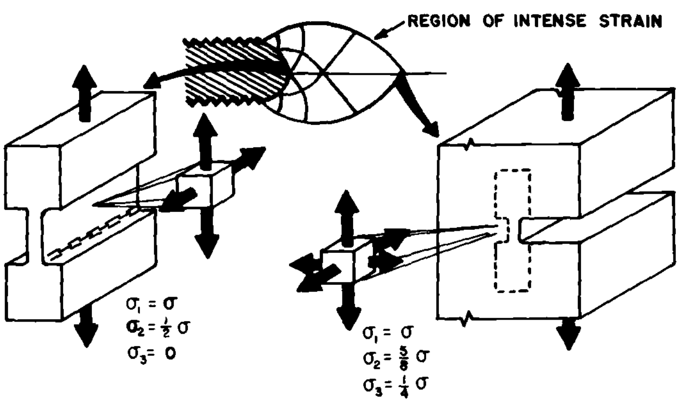

FIG. 8—*Method used to measure crack tip strain distribution.*

Figure 9 shows the uniaxial, biaxial, and triaxial stress state ductility specimens. Fracture strain in the biaxial stress plane-strain ductility specimen was determined following the method outlined by Clausing [21]. The triaxial stress plane-strain ductility specimen maintained, qualitatively, constraint from the biaxial stress plane-strain ductility specimen but additionally added constraint in the third direction. Although fracture should initiate in the triaxial stress field below the surface of the specimen, fracture strain was measured by a strain gage on the surface which is in line with the loading holes.

Figure 10 summarizes biaxial stress plane-strain ductility in terms of fracture strain ratio (FSR), $\bar{\epsilon}_f/\epsilon_{ft}$, versus yield strength. Since the steels investigated were air melted and rolled plates, test section orientation with respect to rolling direction (orientation *A* versus *B* in Fig. 11) affected fracture strain ratio (see total strain data). However, not only absolute values but even the trend of FSR with yield strength was different for the two orientations. For orientation *A*, FSR decreased with increasing yield strength. For orientation *B*, total strain data showed that the FSR was nearly independent of yield strength. An explanation of the anomaly has been suggested by considering the interaction of inclusion shape and macroscopic fracture plane [22]. Void growth occurs most rapidly, in wrought plate, when biaxial stresses are perpendicular to the

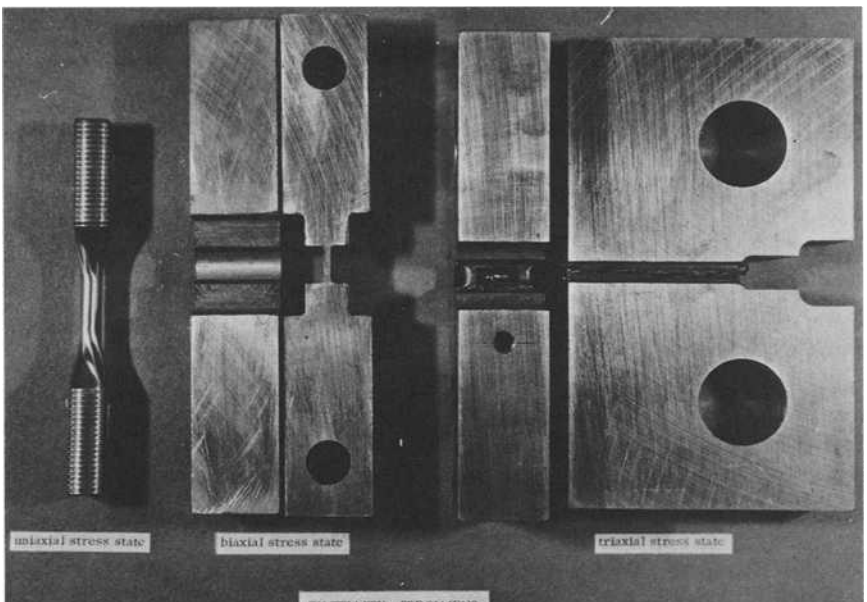

FIG. 9—*Specimens used for measuring fracture strain under different stress states.*

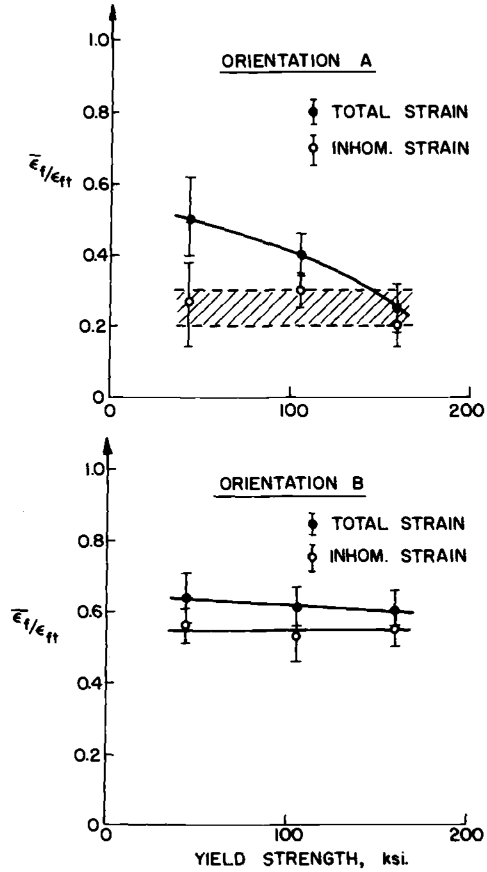

FIG. 10—*Effect of yield strength on fracture strain ratio for the 2:1 biaxial stress state.*

inclusion's longest axis. Orientation *A* in Fig. 11 experiences such stresses only after the "necking" strain is surpassed, whereas orientation *B* experiences such stresses immediately upon loading. Reconsidering FSR using only "strain past necking" values or inhomogeneous strain, ϵ_{ftI}, show a relative independence of FSR on yield strength for both orientation *A* and *B* as demonstrated in Fig. 10. Clausing has generated considerable plane-strain ductility data for the longitudinal direction [*21,24*]. Regardless of whether total or estimated inhomogeneous strain is used, fracture strain ratio decreased with increasing yield strength. Thus, the inhomogeneous strain argument just given would not apply to the longitudinal direction.

Figure 12*a* shows the fracture surface of a 1-in. compact fracture toughness specimen at the fatigue crack-fast fracture boundary. The specimen had been loaded at ambient temperature (fracture mechanism would be microvoid coalescence) to slightly above the P_{Q5} load, then fracture was completed at the liquid nitrogen temperature (fracture mechanism would be quasi-cleavage). The fractograph shows that the original straight fronted crack had tunneled ahead at ambient temperatures in regions of high inclusion density. Thus, the crack front is visualized as becoming very irregular before instability as illustrated in Fig. 12*b*. Instability actually results from the fracturing of sheets having an orientation the same as orientation *A* of the biaxial stress plane-strain ductility specimen. Orientation *A*, incidentally, had the lowest value of FSR.

The results of the triaxial stress ductility specimens are given in Fig. 13 in terms of fracture strain ratio versus yield strength. The curve labeled complete fracture gives the strain (from strain gage readings) necessary to produce two pieces of specimen. Additionally, specimens from each strength level were interrupted during testing, sectioned, prepared metallographically, and examined microscopically. Considerable void growth was observed approximately ¼ in. below the strain gaged surface as indicated in Fig. 13. Thus, complete fracture repre-

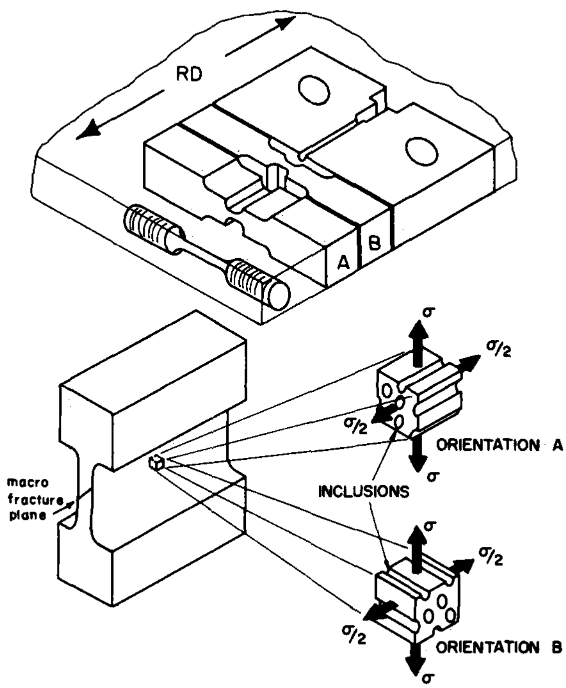

FIG. 11—*Proposed interaction of inclusion distribution and fracture plane.*

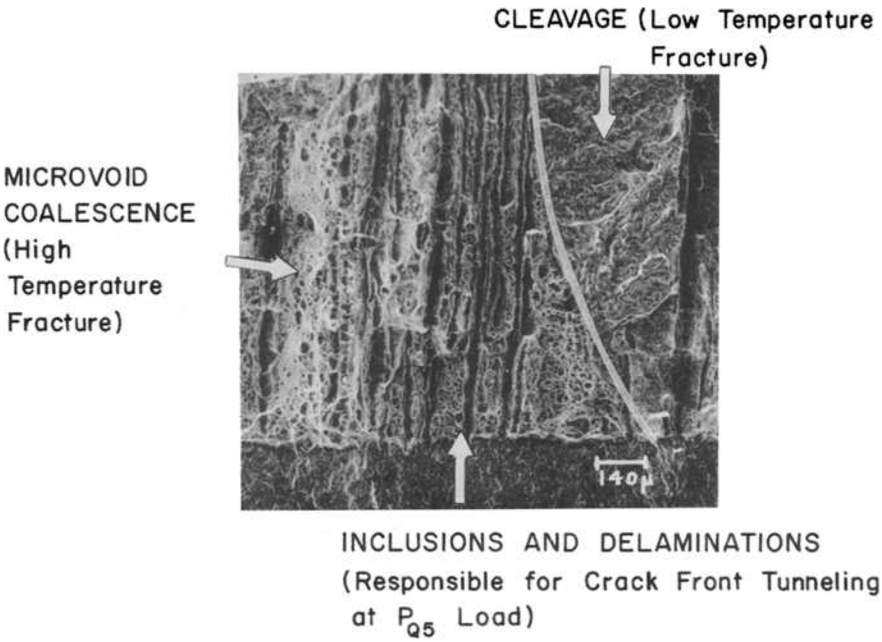

FIG. 12*a*—*Crack front tunneling in high yield strength (IEAFD) fracture toughness specimen.*

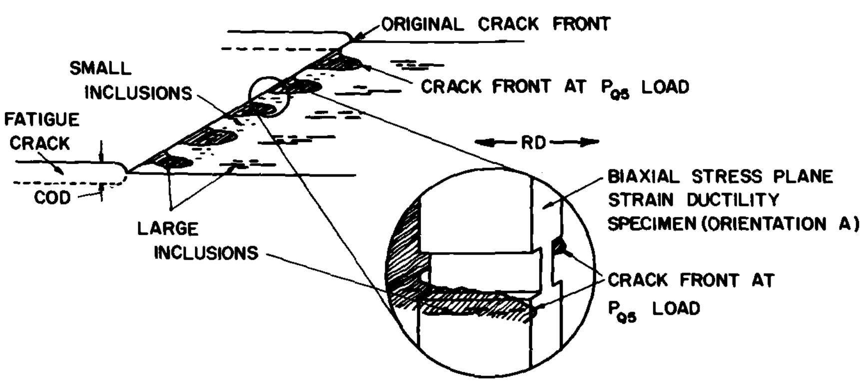

FIG. 12*b*—*Schematic of crack advance as interpreted from fractograph.*

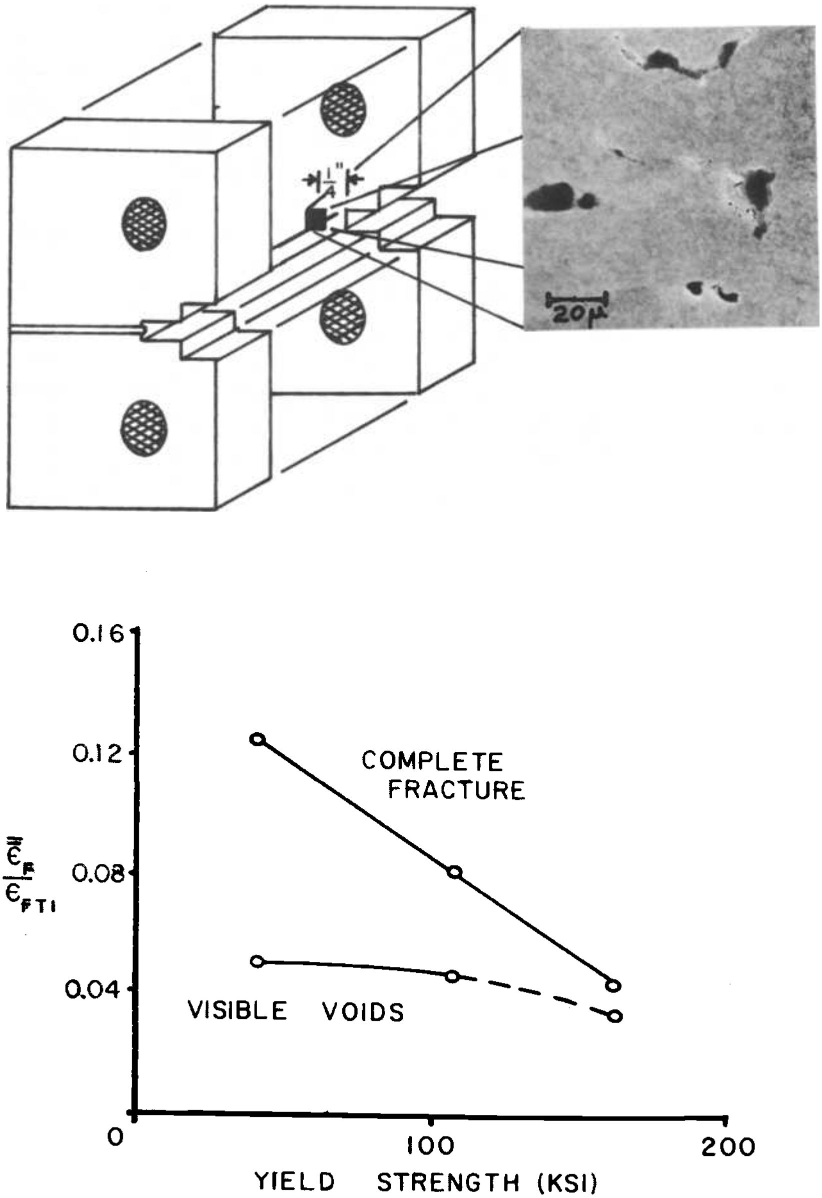

FIG. 13—(a) *Void growth beneath surface in triaxial stress plane-strain ductility specimen.* (b) *Effect of yield strength on fracture strain ratio for triaxial stress plane-strain ductility specimen.*

sented considerable crack growth which was particularly obvious on the fracture surface of the lowest yield strength steel. The strain to void formation and growth, being much less than that for complete fracture, was felt to be more representative of fracture because a high strain gradient exists at the crack tip and crack growth (or fracture) undoubtedly is represented by the coalescence of only a few voids, such as shown in Fig. 13, rather than the existence of a macrocrack.

Delineation of Length Parameter

The data given in Figs. 10 and 13 are proposed to represent fracture strain ratios for the biaxial stress state which exists on the blunted crack tip and the triaxial stress state which exists $\approx 2\delta$ ahead of the crack tip. Thus, the proposed y-direction strain distribution in the region of intense strain can be constructed. Assuming the r^{-1} strain distribution proposed by Rice et al [12], and using 0.045 for the FSR 2δ ahead of the crack tip, gives the following equation.

$$\frac{\bar{\epsilon}_p}{\epsilon_{ftl}} = 0.09 \frac{\delta}{r} \tag{6}$$

Figure 14 shows this strain distribution and illustrates its reasonableness for the biaxial stress situation which exists at the physical crack tip. The actual strain singularity is avoided by recognizing that the upper limit on macroscopically measured strain is the biaxial stress plane-strain ductility. With these assumptions, the r^{-1} strain singularity in the region of intense strain appears realistic. The ductility measurements reported here support rather than confirm the singularity.

The magnitude of the fracture strains under a multiaxial stress state should be emphasized. For instance, the biaxial stress state produced

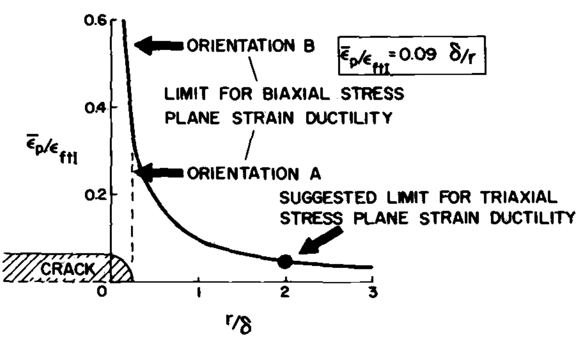

FIG. 14—*Experimentally measured crack tip strain distribution.*

fracture at a strain of only 25 percent of that for the initially uniaxial stress state. The triaxial condition produced fracture at a strain (for void growth) of 4 to 5 percent of the uniaxial value, a reduction by a factor of 20 to 25.

Reemphasizing Rice and Johnson's crack tip blunting model [12], it was assumed that fracture occurred when a strain sufficient to grow voids was reached $\approx 2\delta$ ahead of the physical crack tip. The strain at the physical crack tip must be less than $\simeq 25$ percent of the uniaxial fracture value otherwise fracture would commence there first. Therefore, plastic strain on the physical crack tip $\bar{\epsilon}_p$, was chosen to be 0.2 $\epsilon_{f\mathrm{tI}}$ (or 0.8 times the biaxial plane strain ductility $\bar{\epsilon}_f$).

The strain value, $\bar{\epsilon}_p$, is a result of crack opening and should be relatable to δ by the following rather basic strain-length parameter relationship.

$$\bar{\epsilon}_p = \ln\frac{\delta_{\mathrm{Ic}}}{\delta_o} \tag{7}$$

where

δ_{Ic} = value of δ at fracture and
δ_o = "initial" value of δ.

Solving for δ_{Ic} gives the following equation

$$\delta_{\mathrm{Ic}} = \delta_o e^{\bar{\epsilon}_p} \tag{8}$$

The physical meaning of δ_o can be accounted for best by first substituting Eq 8 into Eq 5 then calculating δ_o from known values of K_{Ic}. Making the substitution gave the following equation

$$G_{\mathrm{Ic}} \simeq \frac{K_{\mathrm{Ic}}{}^2}{E} = CHY\,\delta_o e^{\bar{\epsilon}_p} \tag{9}$$

Table 3 shows results of calculating δ_o from Eq 9 using known values of K_{Ic} for the three steels listed in Table 1 [22]. Results show that δ_o had a value the same order of magnitude as either the ferrite or prior austenite grain size. Values of δ_o increased as yield strength decreased or fracture toughness increased, whereas for the martensitic steels, prior austenite grain size remained unchanged. However, δ_o for the martensitic steels are proportional to the mean-free ferrite path (MFFP) [25]. In fact, 50 times the MFFP was almost numerically equal to δ_o. In the case of the ferritic steel (1E170), δ_o was almost identical to twice the ferrite grain size.

TABLE 3—*Comparison of calculated values with microstructural features.*

Material	δ in.	(μ)	δ_0 in.	(μ)	50 MFFP, in.	(μ)	Grain Size, in.	(μ)
1 EAFD	7.0×10^{-4}	(17.8)	6.3×10^{-4}	(16.0)	6.5×10^{-4}	(16.5)	10×10^{-4}	(25.4)
1 EAEG	13.3×10^{-4}	(33.8)	11.5×10^{-4}	(29.2)	12.5×10^{-4}	(31.8)	10×10^{-4}	(25.4)
1 E170	34.8×10^{-4}	(88.4)	29.6×10^{-4}	(75.2)			15×10^{-4}	(38.1)

The identification of δ_0 with microstructural constituents is logical. Strain implies matrix slip which can occur on the average only over a mean-free ferrite path without obstruction. COD, as measured, results from strain occurring back of the crack tip which has so far been neglected. By considering only the crack tip tensile strain, $\bar{\epsilon}_p$, δ_0 appears as a length parameter over which the tensile strain acts to produce δ, and indeed should be related to units of matrix slip or to a multiple of the MFFP. An interesting result was that for two martensitic steels having widely different strength levels, δ_0 was equal to the same multiple of MFFP. A similar argument for the ferritic steel is necessarily questionable because only one strength level was investigated. However, a mean-free ferrite path in this steel is simply the average ferrite grain size. Figure 15 attempts to illustrate schematically the mean-free ferrite path unit of slip which produced crack openings. It should be emphasized that the magnitude of the constant 50 is not understood. Mean-free ferrite path is, of course, a well-defined microstructural feature. In the case of martensitic steels, the mean-free ferrite path is relatable to the 0.2 percent offset yield strength [25]. Thus, each term in Eq 9 becomes well defined.

$$G_{Ic} \simeq \frac{K_{Ic}{}^2}{E} = CHY\,\delta_0 e^{\bar{\epsilon}_p} \tag{9}$$

where

$\delta_0 = 50$ (MFFP) martensitic steels and
$\delta_0 = 2$ (grain size) ferritic steels.

Comparison of Calculated and Measured Values of K_{Ic}

The proposed relationship between K_{Ic} and mechanical properties is not limited to any particular class of materials. Emphasized in its development were practical and realistic definitions of the continuum quantities flow stress, fracture strain, and length parameter. Naturally, the three steels used to define the terms in Eq 9 gave calculated values which agreed with measured values of K_{Ic}. It is necessary now to explore the generality of Eq 9 and compare calculated and measured values of K_{Ic} for steels not used in its derivation.

Low-Carbon Air-Melted Plate Steels

Table 4 compares calculated and measured values of K_{Ic} for both the longitudinal and transverse direction. The circled values under transverse are the steels used to derive Eq 9. Three other transverse K_{Ic} values are listed, but they are values obtained by extrapolating K_{Ic} data obtained at −40°F [*26*]. Only estimated values of K_{Ic} for the longitudinal direction were available for air-melted plate steels in the 50 to 170 ksi yield strength range [*26,27*]. Examinations of values believed to be the most undisputable revealed that Eq 9 could be used to calculate K_{Ic} for the longitudinal direction (L-T) with only a change in δ_0, the length parameter, from 50 (MFFP) up to 58 (MFFP). Of course, without COD data it was uncertain whether to increase the value of C or increase the constant 50 in 50 (MFFP) when using Eq 9. Regardless of which constant is changed, it is maintained for all calculations made for the

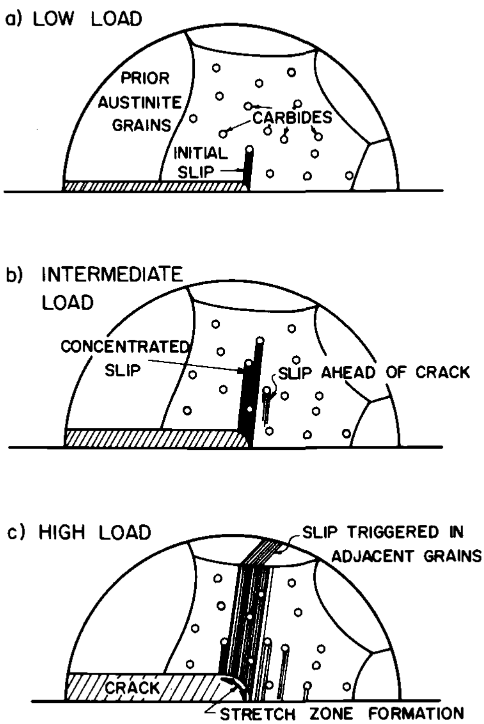

FIG. 15—*Illustration showing interaction of microstructural features with matrix slip.*

TABLE 4—*Calculated/measured values of fracture toughness.*

Material	Yield Strength		Fracture Toughness, K_{IC}			
			Longitudinal, $C\delta_0$ = 75 (MFFP)		Transverse, $C\delta_0$ = 65 (MFFP)	
	ksi	MPa	ksi $\sqrt{\text{in.}}$	MPa $\sqrt{\text{m}}$	ksi $\sqrt{\text{in.}}$	MPa $\sqrt{\text{m}}$
1 E170	41	283			130/122	144/135
1 EAEG	106	731			95/90	105/99
T-1	110	758	128/170*	141/188*		
4147	137	945	96/109*	106/120		
1 E682U	145	1000	97/(108)	107/(119)	80/(91)	88/(100)
4130	158	1089	87/100*	96/110*		
1 EAFD	161	1110			75/73	83/81
70B496	168	1158	84/(85)	93/(94)	71/(69)	78/(76)
99M174	170	1172	85/(74)	94/(82)	72/(61)	79/(67)

NOTE—( ) K_{Ic} extrapolated from data at −40°F.
* = undersize specimen.

longitudinal direction. The required change in some constant as fracture plane orientation changed is not entirely unexpected. The mechanics of ductile fracture are dependent on inclusion shape and distribution, both of which change when fracture plane orientation is changed in wrought steel.

Figure 16 shows measured versus calculated values of K_{Ic} and illustrates with relatively few exceptions that the agreement is within ±10 percent. Equation 9, similar in form to Eq 1 given at the beginning of this paper, is broken into four terms in Fig. 16. Each term is listed and its

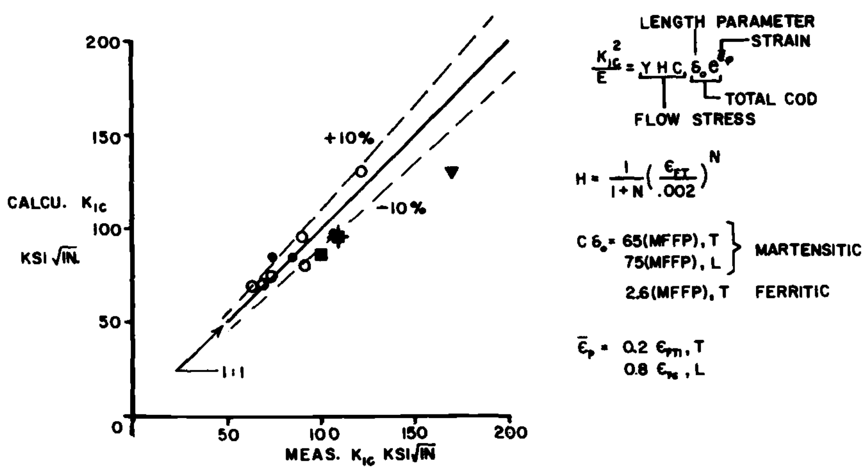

FIG. 16—*Comparison of measured and calculated values of fracture toughness.*

value for the longitudinal and transverse direction given. The least straight-forward term is $\bar{\epsilon}_p$, the plastic strain at the physical crack tip. For the transverse orientation $\bar{\epsilon}_p$ is approximately 20 percent of the inhomogeneous part of the true fracture strain regardless of the yield strength ($\bar{\epsilon}_p = 0.2\epsilon_{fti}$; $\epsilon_{fti} = \epsilon_{ft} - n$). For the longitudinal orientation $\bar{\epsilon}_p$, based on Clausing's data [24], is a function of the yield strength but is still considered to be 0.8 times the plane-strain ductility. The 0.8 is used because in the fracture model, physical separation does not commence at the crack tip but $\approx 2\delta$ ahead of it.

Figure 17 illustrates the trend of fracture toughness, K_{Ic}, with yield strength both for the measured and calculated values. An implicit assumption made was that the air-melted steels are all reasonably similar with respect to cleanliness. Certainly the constant 50 multiplied times the MFFP and used over the entire yield strength range depends on cleanliness being reasonably constant. Thus, the trend of calculated values with yield strength is a reasonably smooth curve, whereas measured values show scatter which is believed to reflect the heat to heat variation in cleanliness.

Medium-Carbon Machinery Steels

Attempts to demonstrate agreement between measured [28] and calculated values of K_{Ic} for high-strength SAE 4340, as shown in Fig. 18, were unsuccessful. Studies of carbide morphology in tempered medium-carbon steels have illustrated an acicular morphology for tempering around 600°F [25,30], thus leaving somewhat in question the meaning of mean-free ferrite path. This, coupled with tempered martensite embrittlement, which would promote something other than fracture by micro-void coalescence [30], makes agreement between calculated and

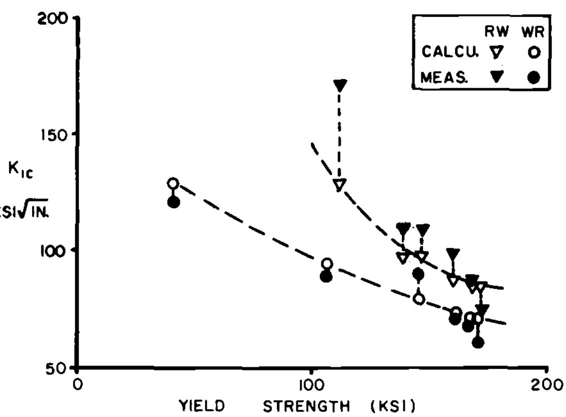

FIG. 17—*Measured and calculated values of fracture toughness as a function of yield strength.*

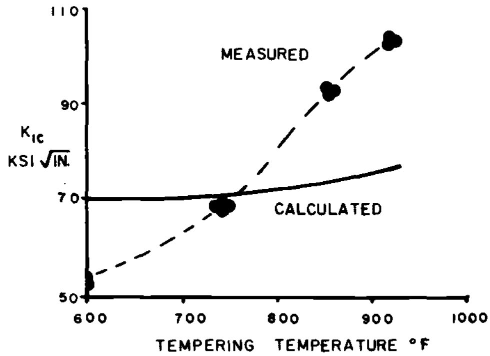

FIG. 18—*Comparison of measured* [28] *and calculated values of fracture toughness for SAE 4340.*

measured values of K_{Ic} unlikely. Indeed, Fig. 18 shows calculated values of K_{Ic} higher than measured values which is at least compatible with suggestions just given. At higher tempering temperatures calculated values of K_{Ic} are less than measured values. Although speculative, this behavior may again reflect the rather poorly defined mean-free ferrite path. Turkalo and Low have illustrated that surface deformation in a tensile specimen follows, preferentially, carbide-free regions [*25*].

Discussion

The foregoing description of crack tip instability in terms of conventional mechanical properties is compatible with the most recent understanding of near crack tip behavior [*10,12,17*]. Values of the constraint correction, *C*, in Eq 5 have been uncertain [*6,10,12*]. Since COD was measured purposely to include crack tip blunting, the value of *C* should be close to the constraint value for the biaxial stress state, 1.15, but higher than it because a biaxial stress state exists only on the blunted crack tip surface. By considering the Von Mises yield criterion, one can easily show that only a very small triaxial component is needed to elevate the constraint factor up to $\simeq 1.3$. Thus, the value of *C* must be considered to represent an average value of constraint over the deformed region of the crack tip which contributes to COD.

The correction for strain hardening, *H*, has been heretofore neglected in COD. Admittedly the correction as used was derived empirically, but it is a well-defined term composed of two very important conventional flow and fracture properties, the power law strain-hardening exponent, *n*, and the uniaxial true fracture strain, ϵ_{ft}.

The envelope of measured COD values for the 161-ksi yield strength steel deviate from the straight line slope of two (Figs. 4 and 6) as the applied stress intensity increases. In all probability, this reflects the formation of the plane-stress shear lip on the specimen surface. Thus, only COD values determined at low values of applied stress intensity are claimed to approximate COD under plane-strain conditions. Additionally, COD measured by a stereo technique from matching halves of the fractured specimen [31] gave COD values at instability which fell on a linear extrapolation of log δ/e_y versus log K/Y data collected at low values of stress intensity.

The strain distribution near the crack tip where voids are initiated has been the subject of considerable discussion by Rice et al [12]. In Rice's analysis, it is assumed that materials fracture (or voids coalesce) at strains between 0.1 and 2.0 which leads to a relationship between COD and R, the spacing of void initiating particles, of COD $\simeq$ (1 to 7)R. However, the results of this investigation, Fig. 12, would dictate that COD $\simeq 0.5R$ or in other words that the extent of the region of intense strain remains approximately two times the COD right up to fracture. Rice's examination of Birkle et al data [32] necessarily assumed that the managanese sulfide nucleated voids expanded until they coalesced. Considerable fractographic evidence on steels indicate that the smaller cementite particles interrupt manganese sulfide nucleated void growth, by initiating voids themselves which eventually produce final fracture. Thus, it is suggested that the seemingly favorable comparison between estimated and measured values of δ/R presented by Rice be reexamined both from the viewpoints of fractographic features and the value of strain proposed here for void coalescence. The attempts to measure crack tip strain distribution described here, although approximate, certainly support the concept of a strain singularity proposed by Rice and Johnson [12]. In view of the noncontinuum nature of metals on the microscale and their inherent inhomogeneities, it is necessary to accept the crack tip strain distribution as being averaged across the entire crack front.

The length parameter, δ_0, introduced in this investigation represents an attempt to incorporate microstructural features into the fracture process. Being proportional to mean-free ferrite path, δ_0 recognizes implicitly the fundamental unit of slip or deformation on the microscopic scale. Mean-free ferrite path in steels is probably the best quantitatively described microstructural feature which can be related to mechanical properties [25]. Thus, it is not surprising that mean-free ferrite path is related to the length parameter over which strain is summed to produce crack opening.

The model of crack lip behavior described serves to explain such things as why fracture toughness decreases with increasing yield strength. For instance, consider the terms of Eq 9. The constraint factor C remains a constant for a given inclusion orientation (that is, L-T or T-L orientation) regardless of yield strength. The strain hardening factor, H, and the length parameter, δ_0, both decrease with increasing yield strength. Typical values for H and δ_0 are:

Y (ksi)	H	δ_0 = 50(MFFP)	$YH\,\delta_0$
100	1.5	1.2×10^{-3} in.	180
160	1.2	0.6×10^{-3} in.	115

Thus, it is seen that for a 60 percent increase in yield strength, one suffers a 20 and a 50 percent decrease in H and δ_0, respectively. The overall effect is a 35 percent decrease in fracture toughness, G_{Ic}. The largest single detriment to fracture toughness was the decreasing mean-free ferrite path with increasing yield strength. Thus, it appears that as long as conventional steels are strengthened by cementite precipitates this trend will persist. Only improvements in cleanliness, which are here interpreted to increase δ_0 by increasing the constant which multiplies mean-free ferrite path, would increase fracture toughness at the same strength level.

In the case of ferritic steels δ_0 is claimed to be proportional to the ferrite grain size. All other conditions equal, increasing grain size should increase fracture toughness. This conclusion, although contrary to conventional practice, is true as long as cleavage fracture is avoided. Unfortunately, some low-alloy ferritic steels under notch or crack tip constraint conditions undergo a fracture mechanism transition (microvoid coalescence $\rightarrow$ cleavage) at temperatures alarmingly close to practical operating temperatures. Thus, the practice of using large grain ferritic steels for the purpose of increasing toughness in general, cannot be recommended.

Usable concepts for designing alloys are implicit in the proposed model of crack tip behavior. For instance, in conventional steels, the length parameter δ_0 was given as a multiple of mean-free ferrite path. Also, in conventional steels, cementite precipitates, Fe_3C, eventually initiate voids, which ultimately lead to failure. It would be advantageous to have the second phase precipitates present for strengthening purposes but not have them act as void initiators. Just such a thing has been realized in the case of maraging steels. As illustrated in the work of Cox and Low [*33*], the difference in fracture toughness between SAE 4340 and 18Ni maraging steel both at the 200-ksi yield strength level cannot be attributed to cleanliness or inclusion spacing but rather to the void initiating particles which produce final fracture. They found that cementite initiated void sheets connected the large inclusion nucleated voids in SAE 4340, whereas in the maraging steel the inclusion nucleated voids themselves grew and coalesced for fracture. Thus, a direct benefit to fracture toughness is seen in the case of maraging steels by metallurgically controlling structure. High strength is achieved by precipitation of a second phase, but the size of individual precipitates is small enough that they do not initiate voids.

Summary and Conclusions

The model of crack tip deformation and instability presented here appears to be in agreement with well established trends of fracture toughness versus various mechanical properties. Certainly a better definition of the constant in the length parameter term deserves additional work.

The information derived from this investigation is as follows.

1. The conventional expression for COD, $\delta/e_y = (K/Y)^2$, after modification to account for constraint and strain hardening was observed to describe accurately COD as a function of elastic modulus, yield strength, and stress intensity for three steels ranging in yield strength from 40 to 160 ksi.

2. Crack tip strain distribution was measured and is believed to support the strain singularity suggested by Rice and Johnson [12].

3. Upon modeling the crack tip in terms of COD and crack tip strain distribution, a length parameter, δ_0, was identified and shown to be proportional to the mean-free ferrite path in steels.

4. Upon assembling the model of crack tip deformation and instability, the following relationship between fracture toughness and mechanical properties was derived

$$G_{Ic} \simeq \frac{K_{Ic}^2}{E} = YCH\ \delta_0 e^{\bar{\epsilon}_p}$$

where

G_{Ic} = critical strain energy release rate;
Y = 0.2 percent offset uniaxial yield strength;
C = constraint factor = 1.3;
H = strain hardening correction term $H = \dfrac{1}{n+1}\left(\dfrac{\epsilon_{ft}}{0.002}\right)^n$;
δ_0 = D (mean-free ferrite path) where D = 50 transverse direction, 58 longitudinal direction; and
$\bar{\epsilon}_p$ = 0.8 (plane-strain fracture strain).

Using this relationship, calculated values of fracture toughness were generally within 10 percent of measure values.

5. The proposed model of crack tip deformation and instability in conjunction with microstructural observation of Cox and Low [33] illus-

trates that fracture toughness decreases with increasing yield strength because mean-free ferrite path (mean cementite spacing) decreases with increasing yield strength and additionally, the cementite precipitates act as void initiation sites.

Acknowledgment

The author wishes to acknowledge the constant encouragement and advice provided by Prof. H. T. Corten, Theoretical and Applied Mechanics Department, University of Illinois, Urbana, Illinois. Caterpillar Tractor Company, Peoria, Illinois, provided financial support for this project. Technical assistance for much of the experimental work was supplied by J. N. Sterner.

References

[1] Steigerwald, E. A. and Hanna, G. L., *Transactions*, American Institute of Mining, Metallurgical, and Petroleum Engineers, Vol. 242, 1968, p. 320.
[2] Vishnevsky, C. and Steigerwald, E. A., *Transactions Quarterly*, American Society for Metals, Vol. 62, 1969, p. 305.
[3] Low, J. R., Jr., *Engineering Fracture Mechanics*, Vol. 1, 1968, p. 47.
[4] Brown, W. F., Jr., and Srawley, J. E. in *Review of Developments in Plane Strain Fracture Toughness Testing, ASTM STP 463*, American Society for Testing and Materials, 1970, p. 216.
[5] Krafft, J. M., *Applied Materials Research*, Vol. 3. 1964, p. 88.
[6] Hahn, G. T. and Rosenfield, A. R. in *Applications Related Phenomena in Titanium Alloys, ASTM STP 432*, American Society for Testing and Materials, 1968, p. 5.
[7] Barsom, J. M., "Relationship Between Plane Strain Ductility and K_{Ic} for Various Steels," Paper No. 71-PVP-13, presented at the First National Congress on Pressure Vessels and Piping, San Francisco, Calif., 10-12 May 1971.
[8] Thomason, P. F., *International Journal of Fracture Mechanics*, Vol. 7, 1971, p. 409.
[9] Weiss, V. in *Mechanical Behavior of Materials*, Proceedings of the International Conference on Mechanical Behavior of Materials, Kyoto, Japan, Vol. 1, 1971, p. 458.
[10] Rice, J. R. and Rosengren, G. F., *Journal of the Mechanics and Physics of Solids*, Vol. 16, 1968, p. 1.
[11] Hutchinson, J. W., *Journal of the Mechanics and Physics of Solids*, Vol. 16, 1968, p. 13.
[12] Rice, J. R. and Johnson, M. A. in *Inelastic Behavior of Solids*, M. F. Kanninen et al, Eds., McGraw-Hill, New York, 1970, p. 641.
[13] Begley, J. A. and Landes, J. D. in *Fracture Toughness, ASTM STP 514*, American Society for Testing and Materials, 1972, p. 1.
[14] Wells, A. A. in *Proceedings*, Cranfield Crack Propagation Symposium, Vol. 1, 1962, p. 210.
[15] Goodier, J. N. and Field, F. A. in *Fracture of Solids*, Drucker and Gilman, Eds., American Institute of Mining, Metallurgical, and Petroleum Engineers, 1963, p. 103.
[16] Bilby, B. A. and Swinden, K. H., *Proceedings of the Royal Society*, Vol. A285, 1965, p. 22.
[17] Rice, J. R. in *Proceedings*, First International Conference on Fracture, Sendi, Japan, Vol. 1, 1965, p. 283.
[18] Wells, A. A., *Engineering Fracture Mechanics*, Vol. 1, 1969, p. 399.
[19] Levy, N., Marcal, P. V., Ostergren, W. J., and Rice, J. R., *International Journal of Fracture Mechanics*, Vol. 7, 1971, p. 143.
[20] Vosikovsky, O., *International Journal of Fracture Mechanics*, Vol. 4, 1968, p. 321.
[21] Clausing, D. P., *International Journal of Fracture Mechanics*, Vol. 6, 1970, p. 71.
[22] Sailors, R. H., "Relationship Between Tensile Properties and Microscopically Ductile Plane Strain Fracture Toughness," TAM Report No. 367, University of Illinois, Urbana, Ill., 1973.

[23] Merkle, J. G., "An Elastic-Plastic Thick Walled Hollow Cylinder Analogy for Analyzing the Strains in the Plastic Zone Just Ahead of a Notch Tip," ORNL-TM 4071, HSST Technical Manuscript No. 20, Oak Ridge National Laboratory, Oak Ridge, Tenn., Jan. 1973.
[24] Clausing, D. P., "Comparison of Plane Strain and Axisymmetric Plastic Flow and Fracture," U.S. Steel Research Laboratory Report, 1 Aug., 1972.
[25] Turkalo, A. M. and Low, J. R., Jr., *Transactions*, American Institute of Mining, Metallurgical, and Petroleum Engineers, Vol. 212, 1958, p. 750.
[26] Sailors, R. H., Caterpillar Tractor Company, unpublished research, 1968.
[27] Rolfe, S. T. and Novak, S. R. in *Review of Developments in Plane Strain Fracture Toughness Testing, ASTM STP 463*, American Society for Testing and Materials, 1970, p. 24.
[28] Jones, M. H. and Brown, W. F., Jr., in *Review of Developments in Plane Strain Fracture Toughness Testing, ASTM STP 463*, American Society for Testing and Materials, 1970, p. 63.
[29] Baker, A. J., Lauta, F. J., and Wei, R. P. in *Structure and Properties of Ultra-High Strength Steel, ASTM STP 370*, American Society for Testing and Materials, 1965, p. 3.
[30] Carr, F. L. et al in *Application of Electron Microfractography to Materials Research, ASTM STP 493*, American Society for Testing and Materials, 1971, p. 36.
[31] Sailors, R. H., University of Illinois, Urbana, Ill., unpublished research, 1973.
[32] Birkle, A. J., Wei, R. P., and Pellissier, G. E., *Transactions Quarterly*, American Society for Metals, Vol. 59, 1966, p. 981.
[33] Cox, T. B. and Low, J. R., Jr., "Investigation of the Plastic Fracture of High Strength Steels," Research Grant NGR 39-087-003, NASA Technical Report No. 3, Carnegie-Mellon University, Pittsburgh, Pa., May 1972.

R. Taggart,[1] *K. K. Wahi,*[2] *and R. Beeuwkes, Jr.*[3]

Relationship Between the Fracture Toughness and the Crack Tip Radius

REFERENCE: Taggart, R., Wahi, K. K., and Beeuwkes, R., Jr., "**Relationship Between the Fracture Toughness and the Crack Tip Radius,**" *Properties Related to Fracture Toughness, ASTM STP 605,* American Society for Testing and Materials, 1976, pp. 62–71.

ABSTRACT: The conditions that surround the tip of a sharp crack in a ductile metallic material dictate the onset of plastic flow and crack extension. The problem of predicting the onset of unstable fracture is related directly to the difficulty of measuring or calculating the actual stresses and strains within the plastic enclave that encompasses the crack tip. Beeuwkes has obtained an approximate solution for the elastic-plastic state in the vicinity of the crack tip and concludes that the crack tip radius after deformation together with the fracture strength at nil ductility of the material form the basis for a fracture criterion.

In this study measurements have been made of the crack opening of fatigue cracked double cantilever beam specimens of 6061-T6 and annealed 4340VM steel. The crack opening measurements have been used to compute the crack tip radius at different loads by fitting the experimental data with an n^{th} order polynomial (n = 2, 4, 6, and 8). The polynomial for which the average deviation in the computed values is a minimum with respect to the measured values was chosen to represent the crack geometry. The values of the crack tip radius as given by this polynomial were plotted against the stress intensity factor.

It has been found for both the selected materials that the stress intensity factor and the crack tip radius follow a linear relation when plotted on a log-log basis. The stress intensity factor and the ratio of the crack tip radius to a critical crack tip radius also plot as a straight line on a log-log basis.

It is concluded that the concept of a critical crack tip radius is consistent with a crack extension model that depends on void coalescence and growth. The data also support the fracture criterion based on the elastic-plastic analysis proposed by Beeuwkes.

[1] Professor, Department of Mechanical Engineering, University of Washington, Seattle, Wash. 98195.

[2] Senior engineer, Science Applications Inc., Oakland, Calif. 94621.

[3] Research engineer, Army Mechanics and Materials Research Center, Watertown Arsenal, Mass.

KEY WORDS: fracture properties, crack propagation, plastic deformation, toughness, fracture strength

Beeuwkes [*1*][4] has obtained an approximate solution to the elastic-plastic state that exists in the vicinity of the tip of a crack and concludes that the radius at the crack tip, just prior to unstable crack propagation, together with the fracture strength at nil ductility of the material form the basis for a fracture criterion. Several investigators [*2*] have attempted to measure the radius at the end of a fatigue crack by making plastic replicas of the open crack. In this study measurements have been made of the crack opening of a fatigue-cracked double cantilever beam specimen. These measurements of the crack opening have been used to compute a crack tip radius.

Burdekin [*3*] suggests that the critical crack opening displacement may be employed to predict critical crack lengths for as-welded structures with residual stresses. According to Kanazawa [*4*] the crack opening displacement is representative of the integrated value of the plastic strain in the plastic zone at the crack tip. It may also be argued that a crack tip has a characteristic (fictitious) radius ρ that allows the computation of the stresses in an element at the crack tip by using an elastic stress concentration factor. Beeuwkes [*1*] describes the plane-strain yielding and fracture at notches and cracks in terms of a crack tip radius and the flow and fracture stresses. This approach differs from linear fracture mechanics in that the ductility of the material and the blunting of the crack tip due to such ductility are considered in formulating a fracture criterion. Beeuwkes [*1*] presents the expression

$$L = \frac{Y}{p}\left(\frac{\rho_i}{a}\right)^{0.5} + \frac{2(1 - \nu^2)Y}{E} \tag{1}$$

where

L = yield boundary having a strain e_e,
p = nominal stress applied perpendicular to the notch axis,
ρ_i = notch tip radius at no load,
Y = yield strength, and
a = notch depth.

The radius under load is given by

$$\left(\frac{\rho}{a}\right)^{0.5} = \left(\frac{\rho_i}{a}\right)^{0.5} + 2(1 - \nu^2)\frac{p}{E} \tag{2}$$

[4] The italic numbers in brackets refer to the list of references appended to this paper.

The parameter L has been tabulated against the angular change of the shear stress trajectory. Beeuwkes indicates that this angular change can be evaluated when the fracture stress at the tensile strain e_e is parallel to the maximum principal stress in the vicinity of the crack tip. It follows that the position of the fracture at strain e_e can be found. The location of this strain leads Beeuwkes [1] to anticipate both subsurface failures and a fracture mechanism that proceeds in a series of steps that correspond with the deformation needed in each step to attain the fracture stress. When this elastic-plastic analysis is considered in relation to the work of other investigators [3-5] it may be postulated that the crack tip radius just prior to fracture is a parameter that can characterize the resistance of a material to unstable crack propagation.

It is generally accepted [5] that transgranular ductile fracture occurs by the creation and coalescence of subsurface microvoids, and in the initial stages the fracture process is intermittent. Beachem [6] records a total of at least 14 mechanisms whereby fracture can proceed by the coalescence of subsurface microvoids, where the conditions ahead of a crack that account for the characteristic dimple shapes are dictated by the plastic strain field and the surrounding elastic strain field. The observations of the fracture surface support the idea that just prior to crack extension the radius at the crack tip attains a critical value and summarizes the total effect of the strain fields. It should be possible to relate this critical radius to the stress intensity factor K, the crack extension force G as defined by Irwin, or to a combination of these terms depending upon the predominance of Modes I, II, or III in the crack opening process.

Experimental Procedure

Double cantilever beam specimens (DCB) were prepared from 6061-T6 aluminum and annealed and hot rolled 4340 VM steel, and the dimensions are shown in Fig. 1. A universal fatigue testing machine, (model SF-01-U Wideman Baldwin) was used to maintain the tension-tension type of fatigue loading that produced consistent fatigue cracks 0.10 mm (0.0039 in.) to 1.00 mm (0.0394 in.) in length at the end of the machined vee notch. All the specimens were polished metallurgically, prior to the fatigue tests, to provide a surface finish that was suitable for optical microscopy up to X600.

The precracked (DCB) specimens were loaded in a special tensile jig as shown in Fig. 2. The jig was mounted on the stage of a metallurgical microscope, and measurements were made with a precalibrated filar eyepiece at X562.5; the closest measurement was 3×10^{-4} in. from the crack tip. The specimen was loaded in Mode I, and the crack opening measurements were made at increasing increments of load until plastic deformation at the crack tip made optical definition in this area impossi-

MATERIAL	L	2h	a_i	b	s	w	z
6061 T6 ALUMINUM	2.25	1.00	0.360	0.10	0.25	0.062	0.250
4340 STEEL	2.25	1.00	0.297	0.10	0.25	0.031	0.375

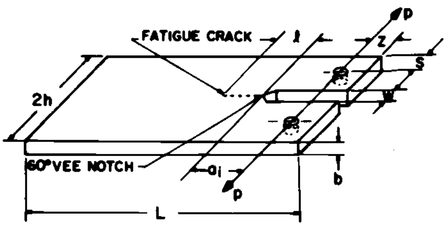

FIG. 1—*Specimen configuration with dimensions in inches.*

ble. The load at each stage was monitored by the load cell, shown in Fig. 2, and when plastic deformation obscured the crack tip it was found to be impossible to maintain the specimen under constant load.

The crack opening displacement data were used to compute the crack tip radius. An n^{th} order polynomial was employed for this computation, and n was made equal to 2, 4, 6, or 8. Even values were chosen for n because the crack was assumed symmetrical about the axis along the crack length. The polynomial was of the form

$$Y = A_0 + A_1X + A_2X^2 + A_3X^3 + \ldots A_nX^n \tag{3}$$

where A_0 is arbitrarily chosen as unity.

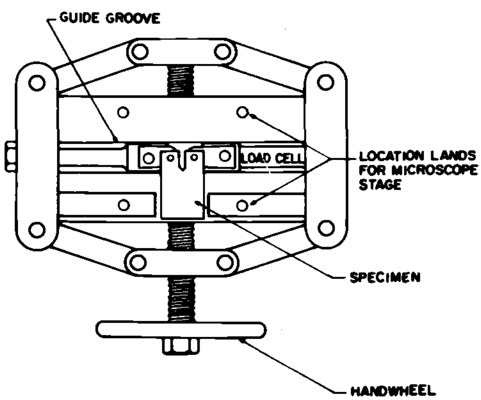

FIG. 2—*Specimen tensile straining jig.*

The radius of curvature was calculated, along the crack length, according to the relation

$$\rho = \frac{\left[1 + \left(\frac{dY}{dx}\right)^2\right]^{1.5}}{\frac{d^2Y}{dX^2}} \tag{4}$$

These computations were carried out at increments of 0.0005 in. along the crack length. The polynomial which indicated the best fit with the experimental data was used to estimate the crack tip radius.

A program written in ALGOL was set up for use with the B-5500 computer. This program was designed to calculate the crack tip radius when an n^{th} order polynomial was fitted to the experimental data. The program also calculated the deviation between the experimental data and the polynomial. The crack tip radius estimated from the curve that displayed the least deviation was used to describe the conditions at the crack tip.

All the precracked (DCB) specimens were pulled to destruction after the crack opening displacement measurements were made, and the final fracture loads are recorded in Tables 1 and 2.

Results and Discussion

The stress intensity factor K_I was calculated for each load and crack length by employing the expression given by Mostovoy [7] for a DCB specimen

$$G_I = \frac{P^2}{2b_n} \frac{24}{3Ebh^3} [3(a + a_0)^2 + h^2] \tag{5}$$

TABLE 1—*Load history of 6061-T6 aluminum specimens.*

Specimen No.	Cyclic Range, lb	Load Max, lb	Number of Cycles, N	Crack Length, 1 in.	Fracture Load, P_{cr} lb	Stress Intensity Factor at P_{cr}, ksi $\sqrt{\text{in.}}$
1A	25	30	124 000	0.00647	618	46.6
2A	25	30	200 000	0.01711	625	47.8
3A	25	30	84 000	0.00684	610	46.0
4A	25	30	384 000	0.03181	600	46.7
5A	25	30	110 000	0.01116	610	46.3

TABLE 2—*Load history of 4340 steel specimens.*

Specimen No.	Cyclic Range, lb	Load Max, lb	Number of Cycles, N	Crack Length, 1 in.	Fracture Load, P_{cr} lb	Stress Intensity Factor at P_{cr}, ksi $\sqrt{\text{in.}}$
1B	125	135	20 000	0.03260	1 250	88.5
2B	115	125	26 000	0.01660	1 300	90.1
3B	100	110	60 000	0.01220	1 260	86.8
4B	90	100	70 000	0.01338	1 305	90.1
5B	90	100	75 000	0.02050	1 300	90.6
6B	90	100	80 000	0.00889	1 295	88.8

Substituting

$$G_{\mathrm{I}} = \frac{(1 - \nu^2) K_{\mathrm{I}}^2}{E}$$

gives

$$K_{\mathrm{I}} = 2P\left[\frac{3(a + a_0)^2 + h^2}{b\, bn\, h^3(1 - \nu^2)}\right]^{0.5} \tag{6}$$

and from Fig. 1 for the present case $b = b_n$, $a = a_i + \ell$, and $a_0 = 0.6h$. The log-log plots of the stress intensity factor K_{I} calculated from Eq 6 versus the crack tip radius (ρ) indicated a linear relationship of the form

$$K_{\mathrm{I}} = m\rho^{m_1} \tag{7}$$

where m and m_1 are constants.

In all cases a 6th order polynomial showed the least average deviation and provided the best fit with the experimental data. The values of ρ in Eq 7 were those obtained from the 6th order polynomial.

The critical crack tip radius ρ_0 for each specimen was obtained by extrapolating the K_{I} versus ρ plot to K_{Ic} for each material. The extrapolation extends the calculated values of the crack tip radius for 4340 VM from 1.0×10^{-5} in. into the range 1.0×10^{-4} in. The values for 6061-T6 are extended from 6×10^{-5} to 1×10^{-2}. Thus, the extrapolation is realistic for the 4340 VM steel since the values of the critical crack tip radius obtained are comparable to those predicted by Beeuwkes [1] on the basis of an elastic-plastic analysis of the crack tip region. There is less confidence placed in the extrapolation for 6061-T6 because it extends over three orders of magnitude. For 6061-T6 aluminum the value of K_{Ic} was assumed to be 30 ksi $\sqrt{\text{in.}}$ and for 4340 VM steel in the annealed condition the value of K_{Ic} was taken as 70 ksi $\sqrt{\text{in}}$. A combined plot of K_I versus ρ/ρ_0 for each material is shown in Figs. 3 and 4 plotted on a log-log basis. The straight line through these points suggests a relation of the form

$$K_I = K_{Ic} (\rho/\rho_0)^{m_1} \tag{8}$$

where m_1 is a constant for each material.

For 6061-T6 aluminum the mean value of m_1 is 0.096, and for 4340 VM steel the mean value of m_1 is 0.188 as measured in Figs. 3 and 4. The average fracture toughness values for 6061-T6 aluminum and 4340 VM steel are recorded in Tables 1 and 2 and were obtained by testing all the DCB specimens to destruction. All the stress intensity factors at the fracture load are greater than the value K_{Ic} for the two materials, and this is attributed to the fact that in each case the final fracture mode was primarily plane stress. In both materials the initial fatigue fracture was plane strain, and this mode was maintained for all the crack lengths during the measurement of the crack opening displacement.

The critical crack tip radius estimated by employing Eq 8 is of the same order as those predicted by Beeuwkes [*1*]. The value of ρ_0 for 4340 VM steel is 2.5×10^{-4} in. compared with the 4×10^{-4} in. reported by Beeuwkes [*1*]. The value of the critical crack tip radius for 6061-T6 is 2.8×10^{-2} in. Beachem [*8*] measured the size of voids that exist ahead of a crack tip in 4340 steel and indicates these to be approximately 1.0×10^{-4} in. diameter prior to unstable fracture. This value for the diameter of a void is between 2 to 3 times smaller than the critical crack tip radius predicted on the basis of these experiments. The results of this study are, therefore, consistent with the hypothesis that crack propagation takes place by void formation and coalescence ahead of the crack tip because

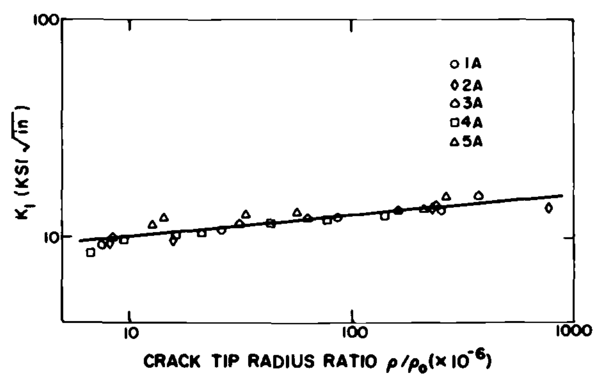

FIG. 3—*Stress intensity factor versus crack tip radius ratio for 6061-T6 aluminum.*

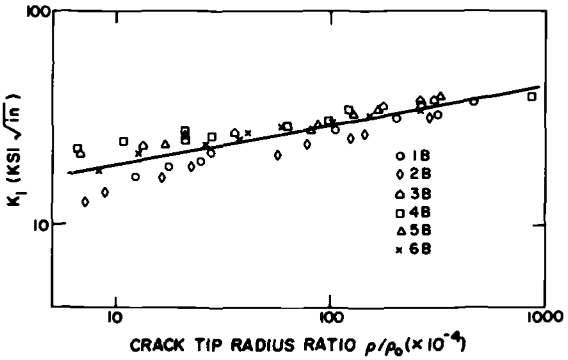

FIG. 4—*Stress intensity factor versus crack tip radius ratio for 4340 VM steel in the annealed condition.*

the void "dimension" is significantly less than the estimated critical crack tip radius.

The critical crack tip radius ρ_0 was also found to be approximately an order of magnitude smaller than the average grain size of either of the materials examined. The crack path and the fracture toughness parameters, therefore, should be influenced to a marked degree by the microstructure, as is generally recognized.

A comparison between the work of Bowles [2] and the present study shows that the results of this investigation are consistent with the fact that fatigue fracture proceeds at a stress intensity factor that is less than K_{Ic}. For 4340 VM, $K_{I_{max}}$ was 19 percent of K_{Ic} while ΔK was 9 percent of K_{Ic}. The corresponding value of the crack tip radius for $K_{I_{max}}$ was 10.25×10^{-8} in. (26.04×10^{-8} cm), and this is about ten times the average lattice parameter. This extrapolation suggests that the mechanism of crack propagation in fatigue cannot be summarized or averaged in terms of a crack tip radius parameter.

Conclusions

1. A relationship of the form

$$K_I = K_{Ic}(\rho/\rho_0)^{m_1}$$

has been defined for 6061-T6 aluminum and annealed 4340 VM steel. The value of the critical crack tip radius ρ_0 is consistent with the hypothesis that crack propagation takes place by void formation and coalescence ahead of the crack tip.

2. The value of the critical crack tip radius ρ_0 is in agreement with the values predicted by Beeuwkes [1] on the basis of an elastic-plastic

analysis of the zone around the crack tip. The results support the model proposed by Beeuwkes as a fracture criterion.

3. The concept of a critical crack tip radius cannot be extended, without modification, to describe crack propagation under cyclic straining.

Acknowledgments

The authors are grateful to the Army Mechanics and Materials Research Center, Watertown, Massachusetts, and to Syracuse University, New York, for the funding of this project under DA-31-124-ARO(D)-112.

References

[1] Beeuwkes, R., Jr., *Surfaces and Interfaces,* Vol. II, 1968.

[2] Bowles, C. Q., "Strain Distribution and Deformation at the Crack Tip in Low Cycle Fatigue," Report to Army Mechanics and Materials Research Center, Watertown, Mass., June 1970.

[3] Burdekin, F. M., Proceedings of the Symposium on Fracture Toughness Concepts for Weldable Structural Steel, Practical Fracture Mechanics for Structural Steel, April 1969, Papers C and F.

[4] Kanazawa, T., Machida, S., Momota, S., and Hagiwara, Y. in *Proceedings,* Second International Conference on Fracture, Brighton, England, April 1969, pp. 1-14.

[5] Beachem, C. D., *Transactions,* American Society for Metals, 1963, Vol. 56, pp. 318-326.

[6] Beachem, C. D., *Transactions,* American Society for Metals, 1975, Vol. 6A, No. 2, pp. 377-383.

[7] Mostovoy, S., Crosley, P. B., and Ripling, E. J., *Journal of Materials,* Vol. 2, 1967, pp. 661-681.

[8] Beachem, C. D., Lupton, T. C., and Brown, B. F., *Metallurgical Transactions,* Vol. 2, No. 1, 1971, pp. 141-143.

J. T. Staley[1]

Microstructure and Toughness of High-Strength Aluminum Alloys

REFERENCE: Staley, J. T., "**Microstructure and Toughness of High-Strength Aluminum Alloys,**" *Properties Related to Fracture Toughness, ASTM STP 605*, American Society for Testing and Materials, 1976, pp. 71–103.

ABSTRACT: The toughness of wrought, high-strength aluminum alloys is related to the amount, type, and morphology of coarse (larger than about 1 μm) constituent particles, intermediate size (about 0.02 to 0.5 μm) dispersoids, and fine (down to about 0.001 μm) precipitates. High toughness can be attained by minimizing the size and volume fraction of constituent particles, increasing the interdispersoid distance, refining the intragranular precipitate in 2XXX alloys, and controlling the intergranular precipitate in 7XXX alloys. For highest toughness in 7XXX alloy products where low residual stress is desired, rapid quenching followed by the minimum amount of cold work required for mechanical stress relief is recommended.

KEY WORDS: wrought aluminum alloys, fracture properties, toughness, notch sensitivity, tear tests, metallurgical constituents, precipitates, crack propagation

The purpose of this paper is to illustrate the relationship between certain microstructural features and the toughness of wrought, high-strength aluminum alloys and to present examples of alloys developed to have high fracture toughness.

Specimens for determining the fracture toughness of aluminum alloys are not standardized, and different indexes of toughness are employed. A brief review of some toughness indexes is offered before the relationship between microstructure and toughness is discussed. Because of the large number of variables usually studied in any investigation to determine effects of microstructure on fracture toughness, use of large-scale specimens designed to measure the stress intensity factors K_c or K_{Ic} is not feasible. Consequently, smaller and less expensive specimens have been

[1] Section head, Physical Metallurgy Division, Alcoa Laboratories, Alcoa Technical Center, Alcoa Center, Pa. 15069.

developed and are often used in alloy development and improvement programs [*1*][2]. The tear specimen provides two indexes of fracture toughness: (1) energy to propagate a crack and (2) ratio of the tear strength to the yield strength [*2*]. Both of these toughness indicators have been found to correlate with K_c[3] and K_{Ic}[*3*], and for the results presented in this paper both changed qualitatively in the same manner with changes in microstructure. The ratio of the strength determined using a circumferentially notched tension specimen to the yield strength of a smooth tension specimen is also used as an index to toughness [*4*]. This toughness indicator has been found to correlate with K_{Ic}[*3*]. Most of the conclusions presented in the paper were made based on results of tests of these specimens. Some of the conclusions have been verified by K_c and K_{Ic}[4] measurements obtained using center cracked panels and compact tension fracture toughness specimens, respectively. K_c and K_{Ic} values estimated from correlation with the tear or notch tension test data are identified as "estimated" in the figures.

Control of three microstructural features in high-strength aluminum alloys has led to substantial improvements in toughness and short-transverse ductility. These three features can be classified as constituents, dispersoids, and hardening precipitates according to the way in which they form.

Constituent Particles

All commercial 2XXX and 7XXX alloys contain significant amounts of the impurity elements iron and silicon. These elements are in liquid solution, but they combine with the other elements and separate during ingot solidification as coarse constituent particles up to about 30 μm in the longest dimension. These constituent particles are broken up somewhat during subsequent fabrication, but they cannot be taken into solid solution.

In addition to these insoluble constituent particles, most of the high-strength aluminum alloys contain intermetallic constituents which are at least partially soluble and may be as large as the insoluble particles. These constituents are made up of the major alloying elements such as zinc, magnesium, and copper and may be combined with aluminum. In certain of the alloys, these constituent particles cannot be completely dissolved

[2] The italic numbers in brackets refer to the list of references appended to this paper.

[3] It is recognized that K_c is not a geometry independent property of the material, but is dependent upon thickness, panel size, and test procedure. All K_c data referred to in this paper were obtained directly from or by correlation of tear tests with tests of 0.063-in.-thick, 16-in.-wide, center cracked panels ($2a/w = 0.25$) without antibuckling guides as described in Ref *3*.

[4] All K_{Ic} data not referred to as "estimated" in this paper were obtained from compact fracture toughness specimens tested in accordance with ASTM Method E 399.

during fabrication or heat treatment because melting is encountered before complete solution can be attained.

Constituent particles are considered to be detrimental to toughness because they fracture when stressed, thus providing preferential crack paths. Numerous investigations [*5-10*] have demonstrated that decreasing the iron and silicon contents decreases the number of Al_7Cu_2Fe, $FeAl_6$, and Mg_2Si insoluble constituents and increases toughness. An example of the effect of decreasing the iron and silicon contents on the toughness of 2024 sheet is illustrated in Fig. 1, and the results of multiple regression analyses of tear tests of 100 lots of 7050 sheet in Fig. 2 provide more quantitative information of the effect of these elements [*11*]. Thermal mechanical treatments prior to solution heat treatment can also increase toughness by modifying the size, distribution, and volume fraction of the partially soluble constituent particles. For example, decreasing the size of the Al_2CuMg particles in high-purity 2124 sheet from a range of about 10 to 20 μm to a range of about 5 to 10 μm by thermal mechanical treatments

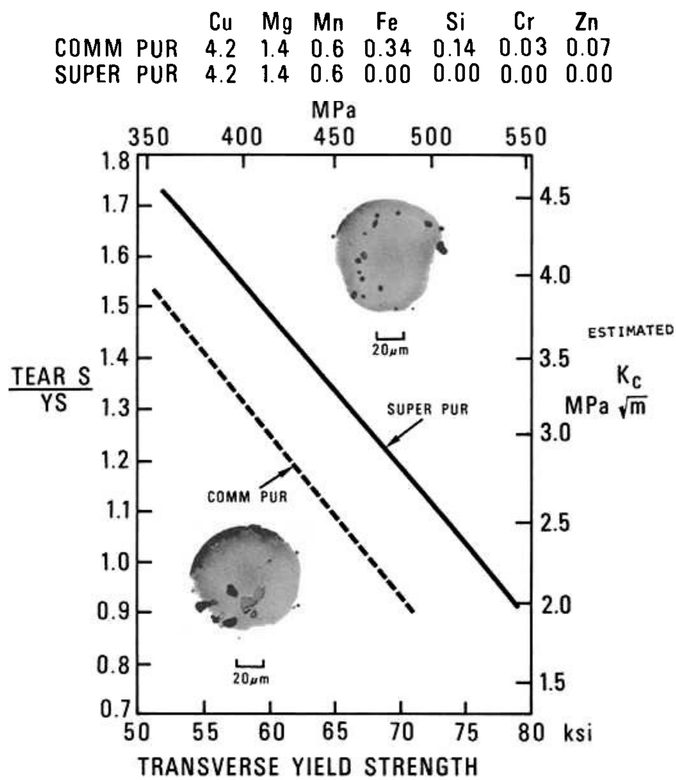

FIG. 1—*Effects of base metal purity on the toughness of 2024 sheet.*

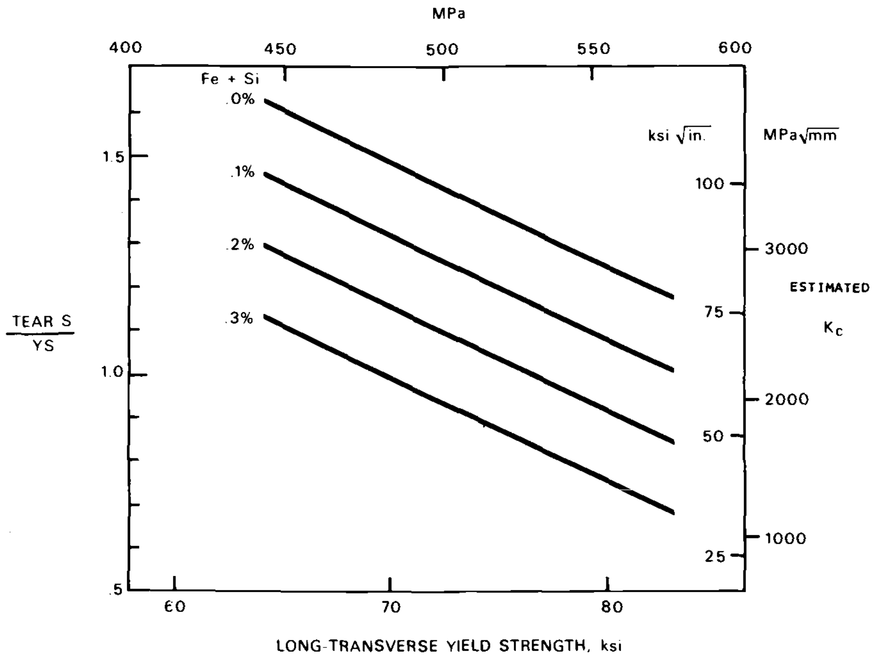

FIG. 2—*Effects of total iron plus silicon on toughness of alloy 7050 sheet.*

increased tear resistance (Fig. 3) and decreasing the volume fraction of the Al_2CuMg particles in 7050 plate increased notch toughness (Fig. 4).

Dispersoid Particles

A second class of particles called dispersoids forms by solid-state precipitation. Either chromium or manganese is added to all of the commercially established 2XXX and 7XXX alloys either to suppress recrystallization in hot worked mill products or to prevent grain coarsening in mill products cold worked prior to solution treatment. The amounts added (up to 0.3 percent chromium and 0.8 percent manganese) are retained in supersaturated solid solution during solidification but precipitate during the ingot preheat treatment as $Al_{12}Mg_2Cr$ or $Al_{20}Mn_3Cu_2$ dispersoid particles having a size of about 0.02 to 0.5 μm in the largest dimension. Once formed, these high-temperature precipitates cannot be completely dissolved, but their volume fraction, size, and distribution can be modified somewhat by thermal mechanical treatments.

Examination of fractographs of mating specimen surfaces revealed the role of $Al_{12}Mg_2Cr$ dispersoids in the fracture process (Fig. 5). One of these particles was almost invariably detected in a dimple on one or the other of the fractured surfaces. Moreover, examination of fractographs (Fig. 6) and random sections (Fig. 7) of specimens exhibiting high and low tear

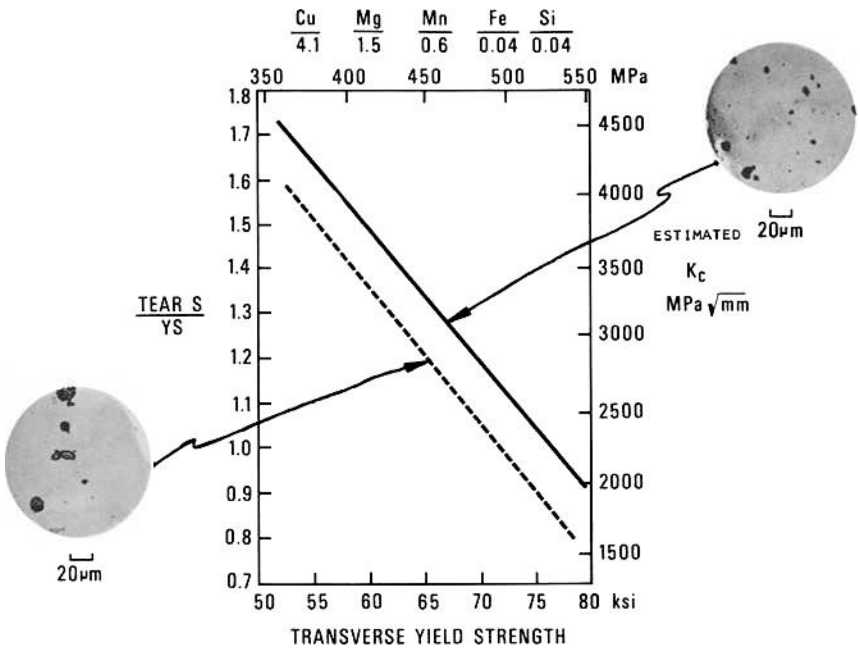

FIG. 3—*Effects of Al_2CuMg constituent size on the toughness of 2124 sheet.*

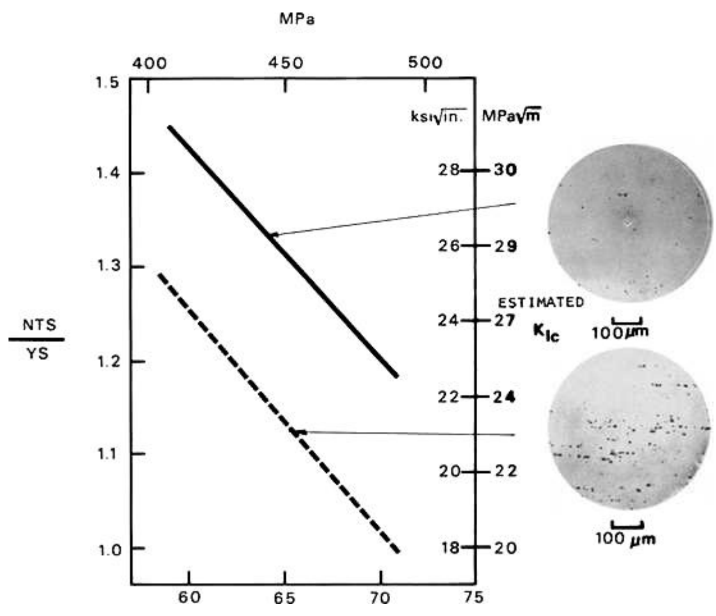

FIG. 4—*Effects of amount of Al_2CuMg constituent on the toughness of 7050 plate.*

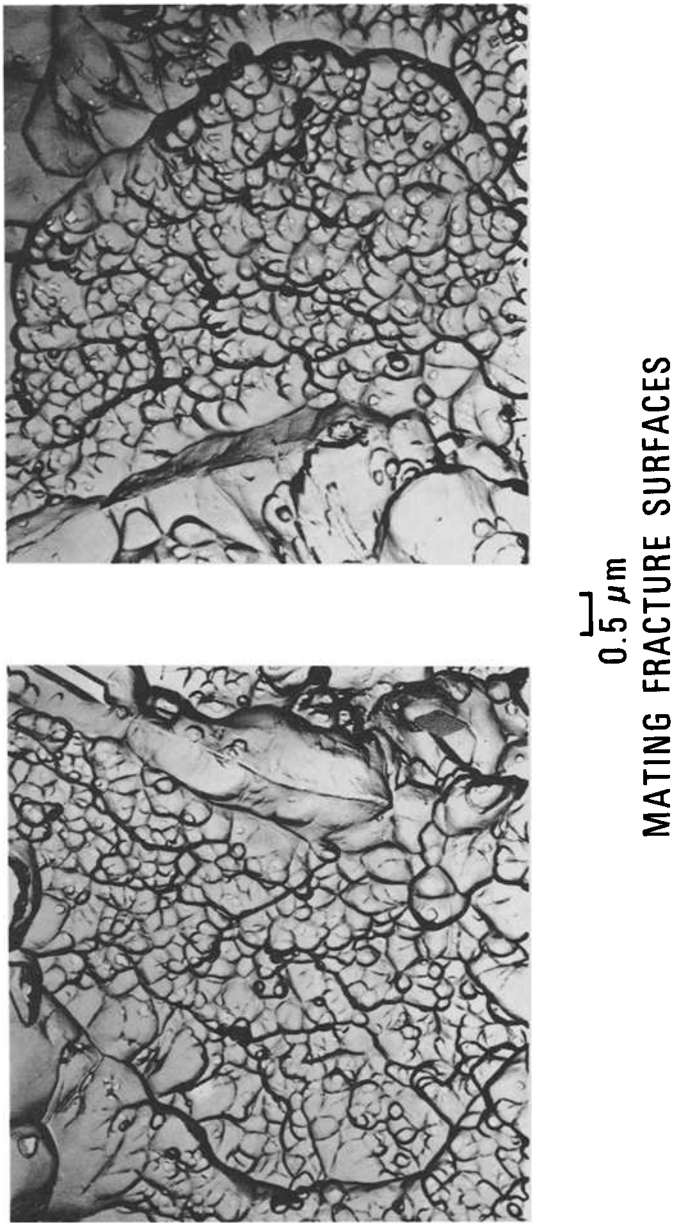

FIG. 5—*Oxide replicas of mating fractured tear specimens of 7075 sheet.*

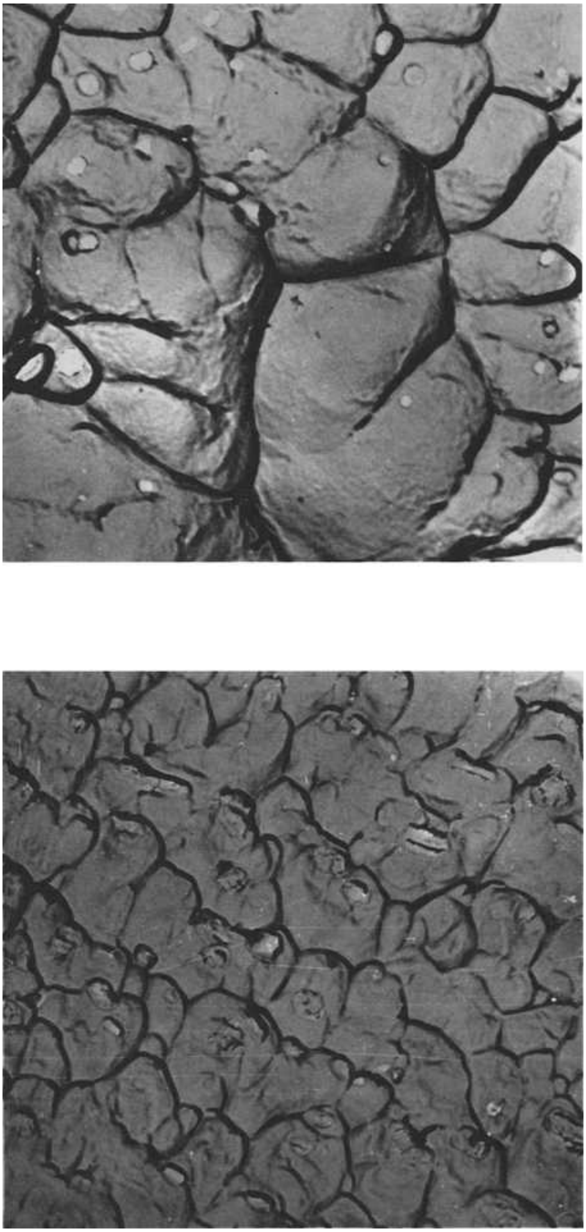

0.2 μm

90 in.-lb/in.^{2} (16 Nmm/mm^2)	CRACK PROPAGATION ENERGY	470 in.-lb/in.^{2} (82 Nmm/mm^2)
45 ksi$\sqrt{\text{in.}}$ (50 MPa$\sqrt{\text{m}}$)	ESTIMATED K_c	90 ksi$\sqrt{\text{in.}}$ (100 MPa$\sqrt{\text{m}}$)

FIG. 6—*Oxide replicas of fractured tear specimens of 7475 sheet.*

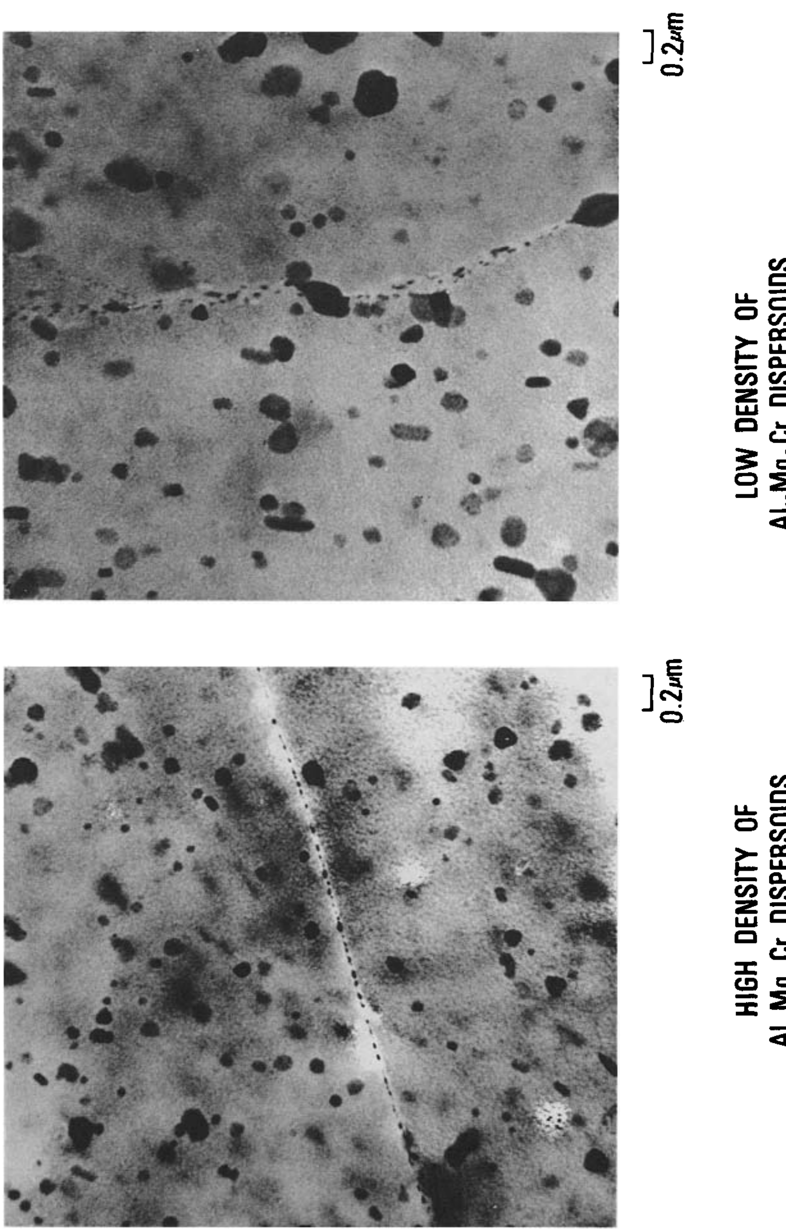

FIG. 7—*Transmission electron micrographs of 7475 sheet having high- and low-areal densities of dispersoids.*

resistance indicated that toughness increased with increasing dimple size and with decreasing number of dispersoids. Quantitative metallography of fractographs of tear specimens from several lots of commercial and super purity 7075 sheet exhibiting a wide range of crack propagation energies confirmed the effect of dispersoid density (Fig. 8). Tests of experimental alloys, however, revealed that the energy to propagate a crack decreased linearly with increasing chromium content (Fig. 9). The process by which the microvoids form at dispersoids and coalesce to link fractured constituents has been termed void sheet formation [9].

Because dispersoids which contain chromium strongly affect toughness, effects of substituting either manganese or zirconium for the chromium in alloy 7475 have been examined. In one investigation, 3-in.-thick 7475 plate (0.2 percent chromium) and similar plate containing either 0.5 percent manganese or 0.1 percent zirconium were examined and tested. Structural examinations indicated differences in both dispersoids and grain structure (Fig. 10). Both tear strength : yield strength ratios and crack propagation energies indicated that substituting zirconium for chromium increased toughness and that substituting manganese for chromium decreased toughness. Subsequent K_{Ic} measurements (Table 1) using compact fracture toughness specimens from plate aged to the same strength level confirmed the harmful effects of manganese but failed to substantiate the advantage of the zirconium. These results indicate that the toughness indicator can influence relative ranking of the toughness of aluminum alloys.

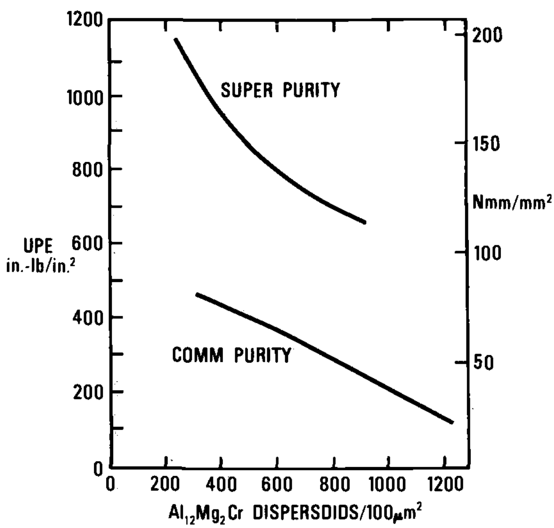

FIG. 8—*Unit crack propagation energy of 7075 sheet versus density of dispersoids on fractured surface.*

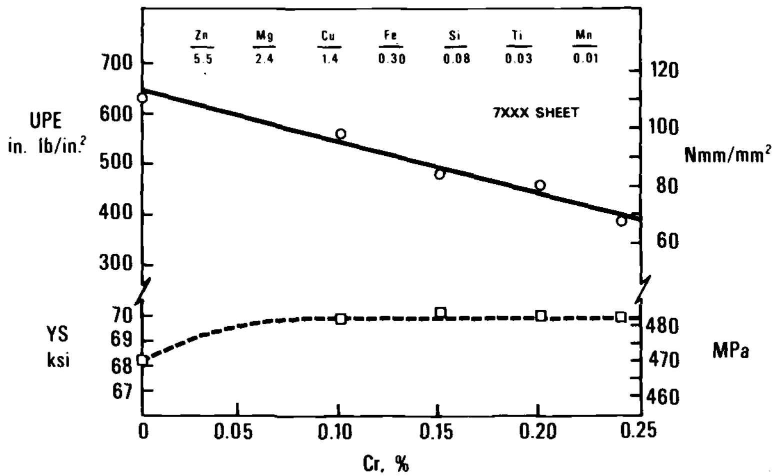

FIG. 9—*Effect of chromium content on unit crack propagation energy and yield strength.*

Comparative effects of the dispersoid-forming elements chromium, zirconium, and manganese on the toughness of super purity 7XXX alloy sheet have also been studied. In one experiment, fine grained sheets of alloys containing either 0.2 percent chromium, 0.3 percent manganese, or 0.1 percent zirconium developed comparable tear resistance. Tear resistance of the alloy containing both zirconium and chromium was on the low side of the band (Fig. 11), but the tear resistances of the alloys containing only one ancillary element appeared to be comparable.

Comparison of the test results of the plate and sheet indicates that effects of dispersoids on toughness may also be associated with their effect on grain structure.

Hardening Precipitates

A third microstructural feature in these alloys forms after the solution treatment either inadvertently during the quenching or in a controlled manner during precipitation heat treatments (aging). The size of these features ranges from about 10^{-3} μm for Guinier-Preston (G-P) zones

TABLE 1—*Effect of ancillary element addition on* K_{Ic} *of high-purity 7075-type plate.*

	Yield ksi	Strength (MPa)	K_{Ic}, ksi$\sqrt{\text{in.}}$ (MPa$\sqrt{\text{mm}}$)		
			0.2% Cr	0.1% Zr	0.5% Mn
L-T	65	(445)	40.2 (1400)	38.3 (1330)	33.7 (1175)
T-L	63	(430)	37.4 (1300)	32.3 (1125)	29.1 (1015)
S-L	59	(410)	28.6 (1000)	29.2 (1015)	25.0 (870)

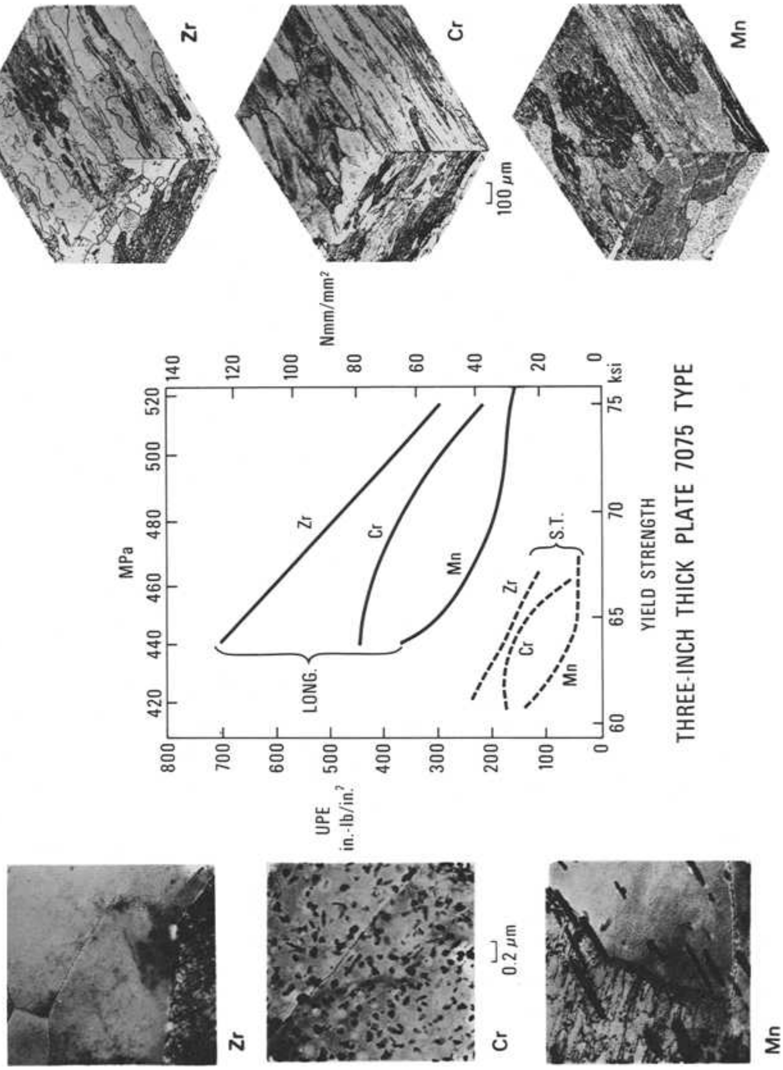

FIG. 10—*Effect of ancillary element additions on the energy to propagate a crack.*

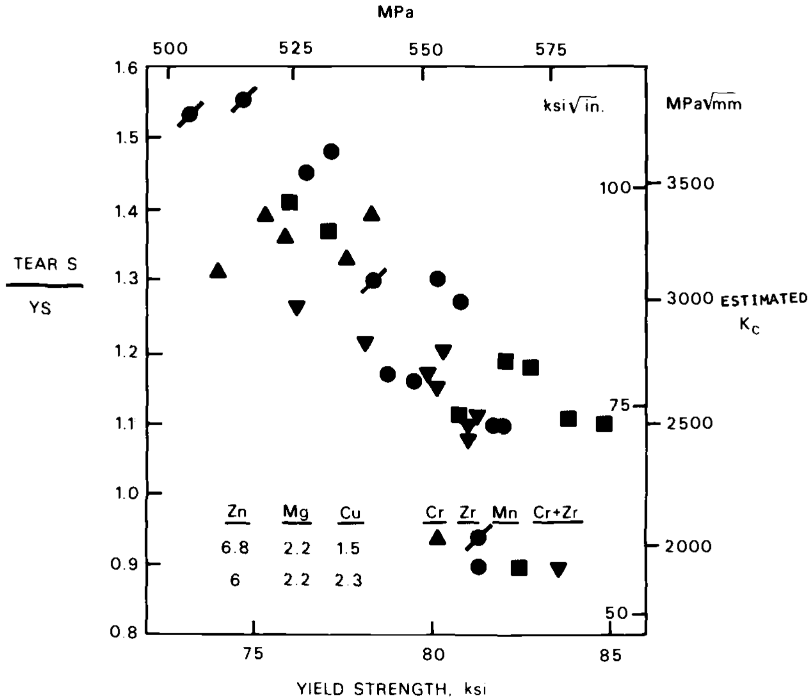

FIG. 11—*Effect of ancillary element addition on the tear strength: yield strength ratio of super purity 7XXX alloy sheet.*

formed at room temperature up to about 1 μm for coarse grain boundary precipitate formed during slow quenching or on drastic overaging.

Effects of precipitate morphology on toughness are different for the 2XXX and 7XXX alloys. Alloy 2024-T4 sheet which hardens by submicroscopic G-P zones develops higher toughness than overaged 2024 sheet which has a structure of coarse, corrugated, lath-type crystalline precipitates [*12,14*]. Cold working prior to artificial aging refines the crystalline precipitates, but underaged 2024 sheet develops higher toughness than sheet overaged to the same strength level (Fig. 12).

In contrast to these results, tear tests of five lots of 7075 and 7475 sheet indicated that intragranular precipitate morphology in alloys of this type (Fig. 13 shows test results of two lots) had no significant effect. Alloy 7075-W sheet, which age hardens by submicroscopic G-P zone precipitates, developed the same tear resistance as overaged 7075-T73 sheet which had a structure containing crystalline precipitates up to about 0.02 μm in the longest dimension (Fig. 14). The 7075-T6 sheet samples developed the highest strength and the lowest tear resistance. The hardening precipitate structure consisted of coarse G-P zones and fine crystalline precipitate.

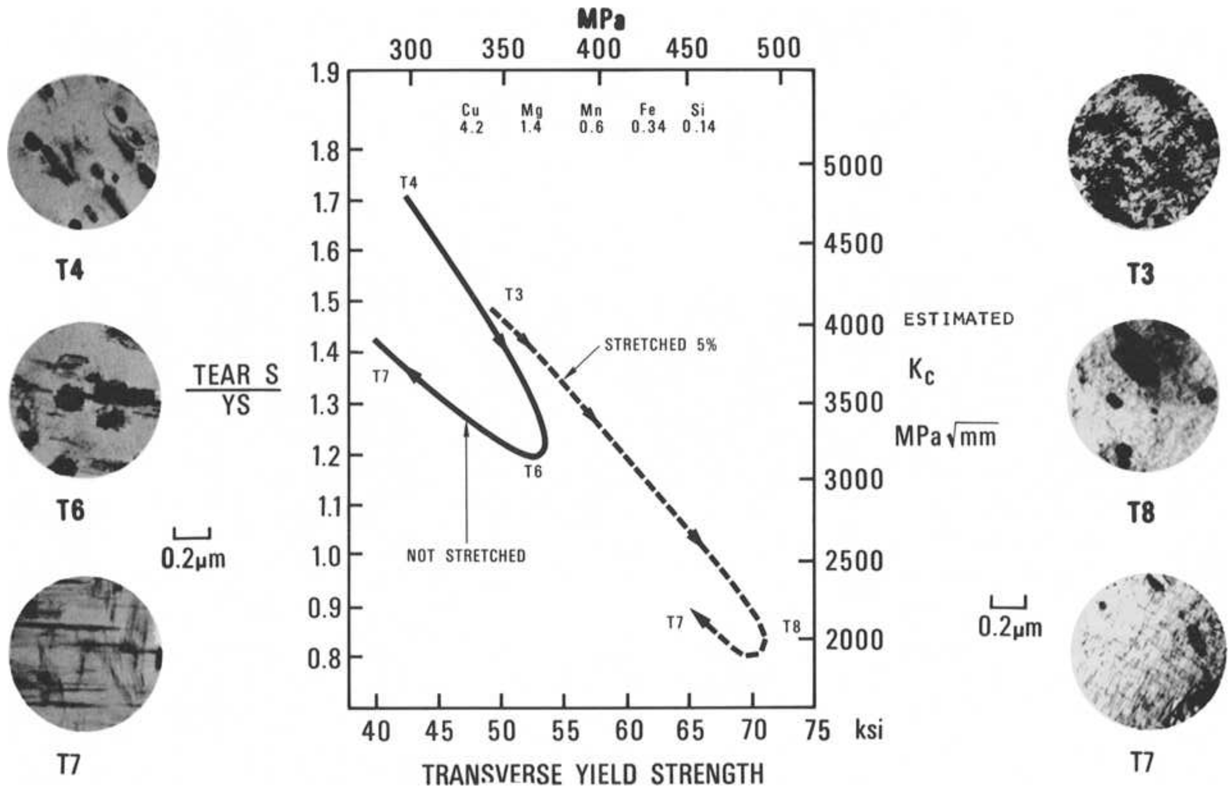

FIG. 12—*Effect of age hardening precipitate structure on the tear strength: yield strength ratio of 2024 sheet.*

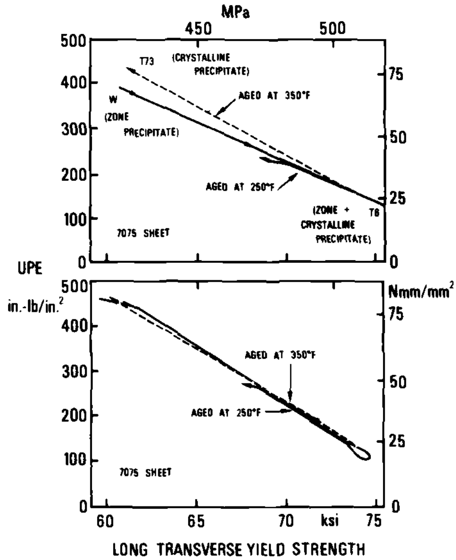

FIG. 13—*Effect of precipitation heat treatment practice on the unit crack propagation energy in 7075 sheet.*

Grain boundary precipitate, however, significantly affects toughness by controlling the relative amounts of intergranular fracture [*12,15*]. The morphology of these precipitates is affected by composition, grain structure, and quenching as well as aging conditions. High-solute contents, high-angle grain boundaries, slow quenching, and high-temperature aging treatments that are not preceded by low-temperature aging treatments may produce grain boundary precipitates and wide precipitate-free zones which favor intergranular fracture and low toughness.

Effects of differences in grain structure on the precipitate morphology and consequent effects on intergranular fracture and notch toughness are illustrated by an experiment with alloy 7050 plate. In this experiment 4.5-cm-thick plates having either almost completely unrecrystallized or almost completely recrystallized grain structures were prepared using thermal mechanical treatments. A range of yield strengths was obtained by overaging a series of samples at 325°F (436 K) following solution treatment, quenching, stretching 2 percent, and preaging 24 h at 250°F (394 K). Toughness in the transverse direction was characterized using notch tension specimens. Notch toughness of the unrecrystallized plate was higher than that of the recrystallized plate at comparable yield strengths (Fig. 15 shows results of short-transverse tests).

The relatively high toughness of the unrecrystallized material is attributed to structural features within the grains and at grain boundaries (Fig. 16). The large number of dislocations and low angle grain boundaries act

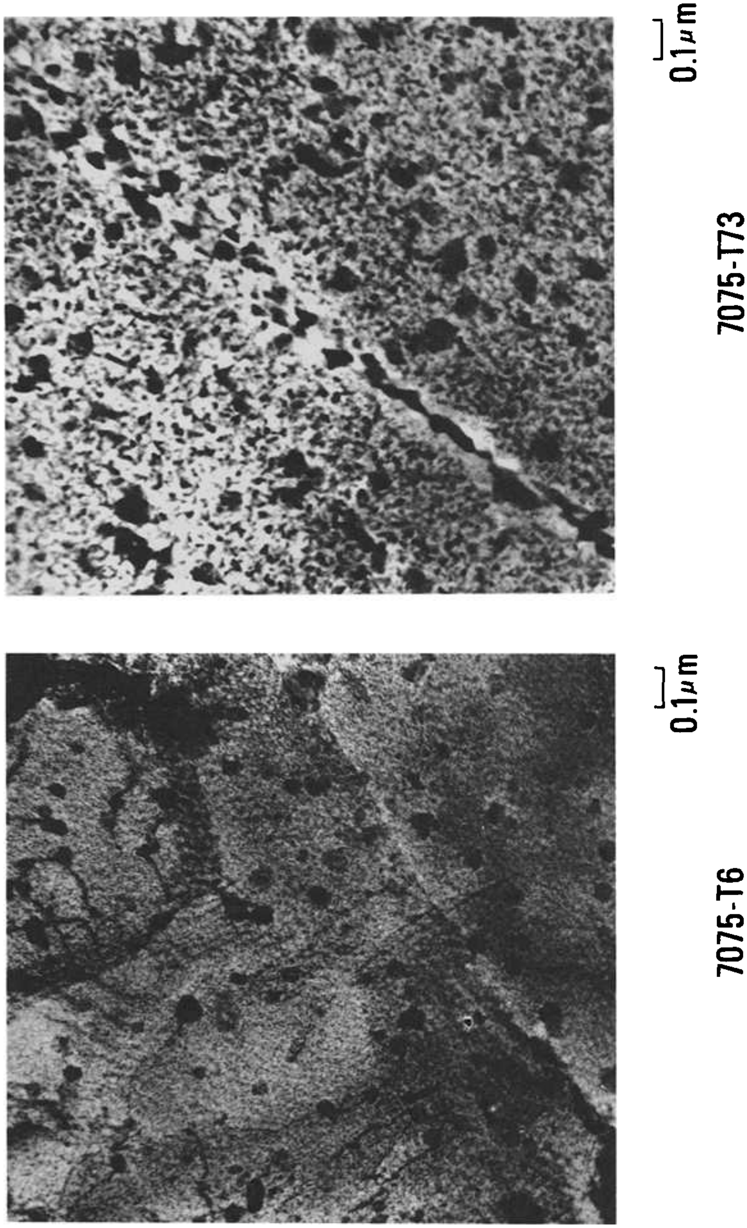

FIG. 14—*Transmission electron micrographs of 7075-T6 and 7075-T73 sheet.*

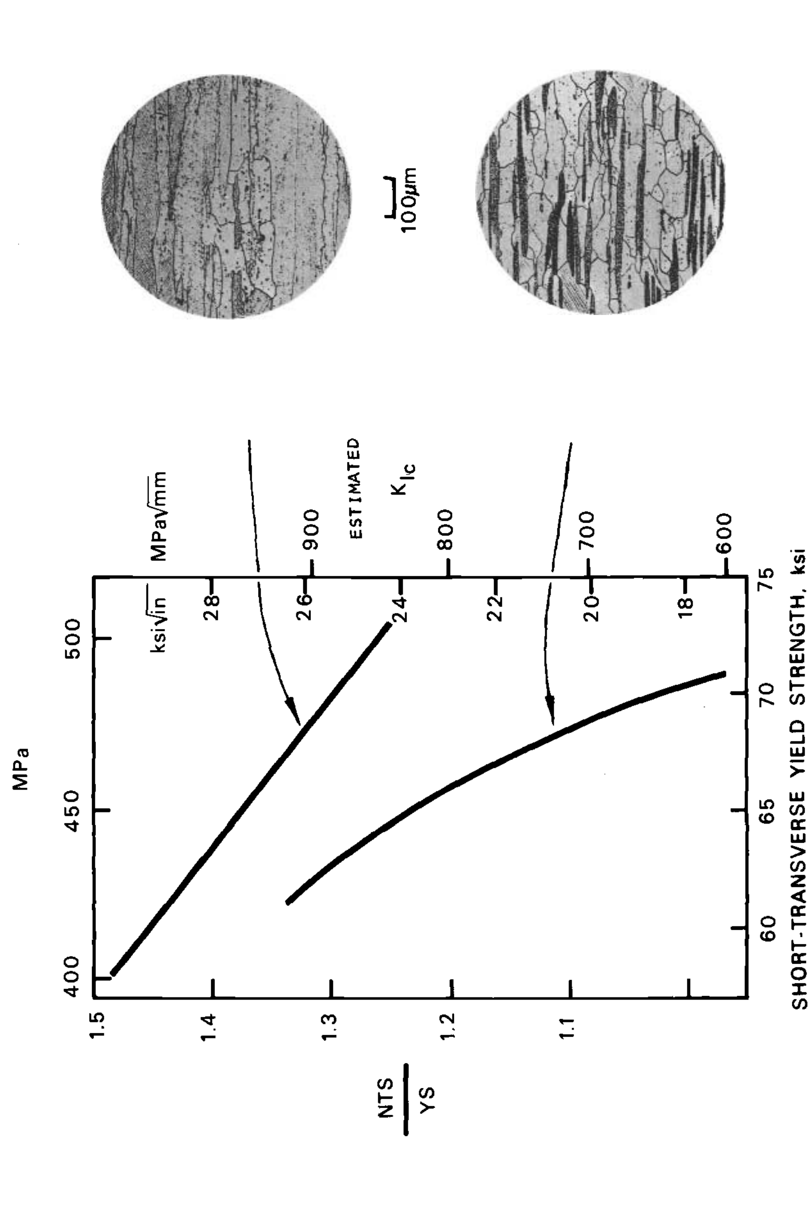

FIG. 15—*Effect of degree of recrystallization on notch toughness of 7050 plate.*

NOTE THE SUB-GRAIN STRUCTURE AND THE PLATELET MORPHOLOGY OF THE HARDENING PRECIPITATE η'.

FIG. 16—*Transmission electron micrograph of overage 7050 plate having a low degree of recrystallization.*

as sites for precipitation of fine η' platelets. These partially coherent precipitates promote homogeneous slip by forcing dislocations to bow around the precipitate particles. In addition, the growth of incipient slip bands is impeded by the subgrain boundaries and the dislocations within the grains. Consequently, dislocations cannot pile up at grain boundaries. Moreover, the copious precipitation on dislocations and low-angle boundaries precludes the formation of large, brittle grain boundary precipitates and of wide precipitate-free zones (PFZ). As a result, the material fractures largely by the transgranular dimple rupture mode (Fig. 17, top).

The lower toughness of the recrystallized plate is attributed to a larger proportion of intergranular fracture caused by alterations in the dislocation, precipitate, and grain boundary structures (Fig. 18). Because few subgrain boundaries are present, slip bands can develop the length of the grain when the recrystallized material is stressed. These dislocations pile

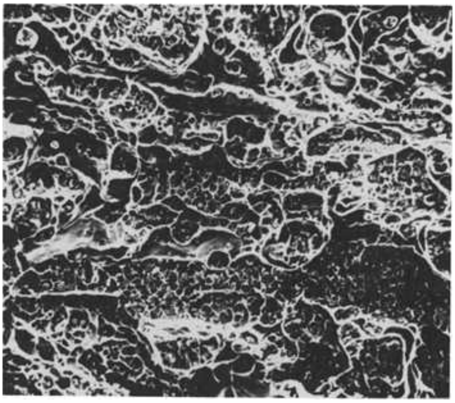

SHORT-TRANSVERSE PROPERTIES

YS 70 ksi (480 MPa)

$\frac{NTS}{YS}$ 1.22

EST K_{Ic} 24.5 ksi$\sqrt{in.}$ (860 MPa$\sqrt{mm}$)

SAMPLE NO. 418966-14B-2 50 μm

ALMOST COMPLETELY UNRECRYSTALLIZED

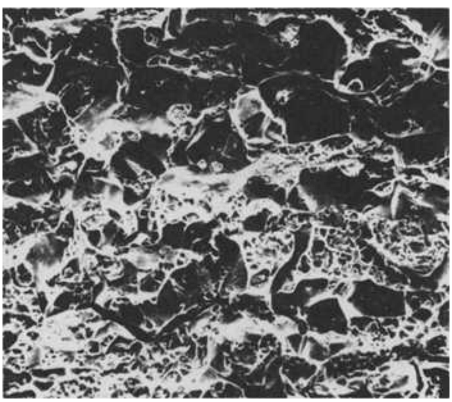

YS 70 ksi (480 MPa)

$\frac{NTS}{YS}$ 0.96

EST K_{Ic} 17 ksi$\sqrt{in.}$ (600 MPa$\sqrt{mm}$)

SAMPLE NO. 418966-34B-1 50μm

ALMOST COMPLETELY RECRYSTALLIZED

FIG. 17—*Illustrates high degree of intergranular fracture in almost completely recrystallized 7050 plate.*

up at grain boundaries and exert a force for intergranular separation. Furthermore, the high-angle boundaries act as vacancy sinks, thus promoting the development of a wide PFZ during artificial aging. Finally, the high-angle boundaries are preferred sites for nucleation of coarse equilibrium precipitates which weaken the grain boundaries. The combination of the stress exerted by the dislocations, the wide PFZ, and the

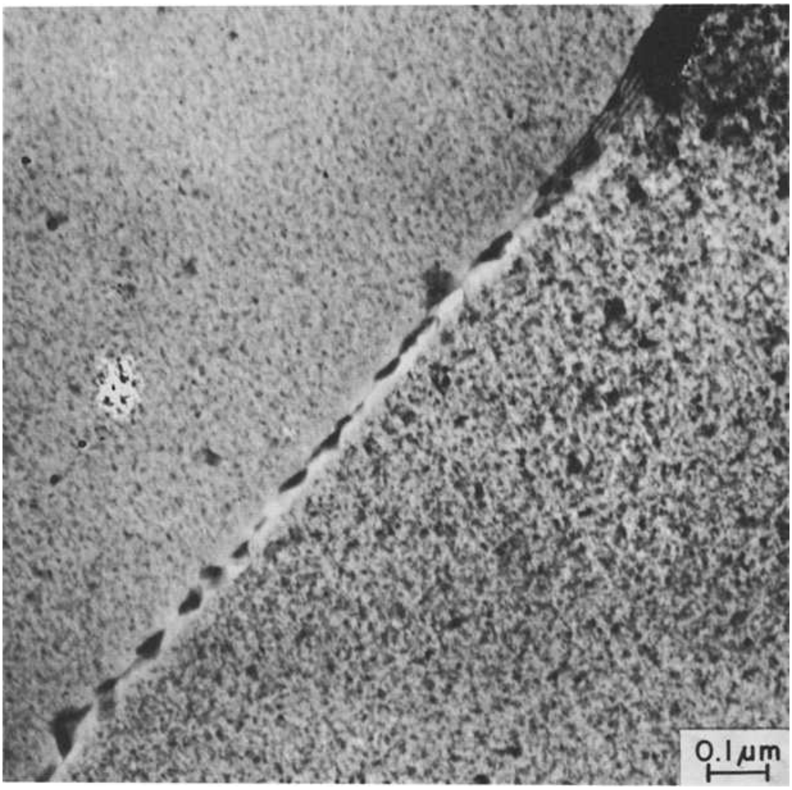

NOTE THE WIDE PFZ AND LARGE GRAIN BOUNDARY PRECIPITATES.

FIG. 18—*Transmission electron micrograph of overaged 7050 plate having a high degree of recrystallization.*

coarse grain boundary precipitates promotes fracture at or near the grain boundaries (Fig. 17, bottom).

Differences in composition which make subtle changes in hardening precipitate structure also affect toughness. Toughness of 7XXX alloys decreases with increasing magnesium content when compared at equal strength [*12*], and 7XXX alloys containing copper generally develop higher toughness than similar copper-free alloys aged to the same strength [*10*]. In general, toughness of high-solute 7XXX-T7 (overaged) products is lower than that of lower solute 7XXX-T6 (peak strength) products (Fig. 19), although toughness of individual lots is identical when compared at equal underaged and overaged strengths. The explanation for this apparent paradox is illustrated in Fig. 20. Consider a particular high-solute alloy which has high strength and low toughness. Decreasing strength by

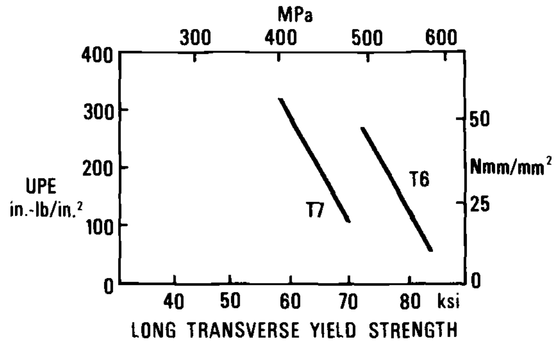

FIG. 19—*Unit crack propagation energies of commercial 7XXX alloy plate in peak strength and overaged tempers.*

modifying the aging practices increases toughness to some degree, but substituting a lower-solute alloy aged to peak strength increases toughness to a higher degree for the same sacrifice in strength.

Although cold working 2024 and most other 2XXX alloy products prior to artificial aging refines the precipitate structure and increases strength, cold working 7XXX alloy products prior to aging above about 300°F (422 K) coarsens the precipitate structure and decreases strength. This phenomenon is illustrated by the structure and properties of stretched and unstretched alloy 7050 plate which had been aged to near peak strength by

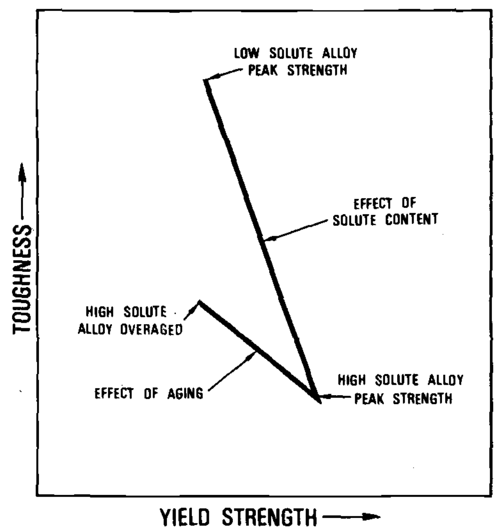

FIG. 20—*Illustrates effect of decreasing solute content and overaging on the toughness-yield strength relationship of 7XXX alloy products.*

the same practice (Fig. 21). Moreover, examinations of unstretched, overaged alloy 7050 plate and similar plate that had been stretched either 1 percent or 4 percent, then overaged to the same short-transverse yield strength, reveal that stretching progressively coarsened the precipitate structure despite the shorter aging times (Fig. 22). The notch toughness of the plate at comparable yield strengths also progressively decreased with increasing amount of stretch (Fig. 23),while the percentage of intergranular fracture increased. The change in fracture mode and decrease in toughness are attributed to alterations in deformation mechanisms within grains by the dislocations introduced during stretching.

Summary

In summary, the effects of soluble and insoluble constituents, dispersoids, and hardening precipitates on toughness of high-strength aluminum

UNSTRETCHED | STRETCHED 4%

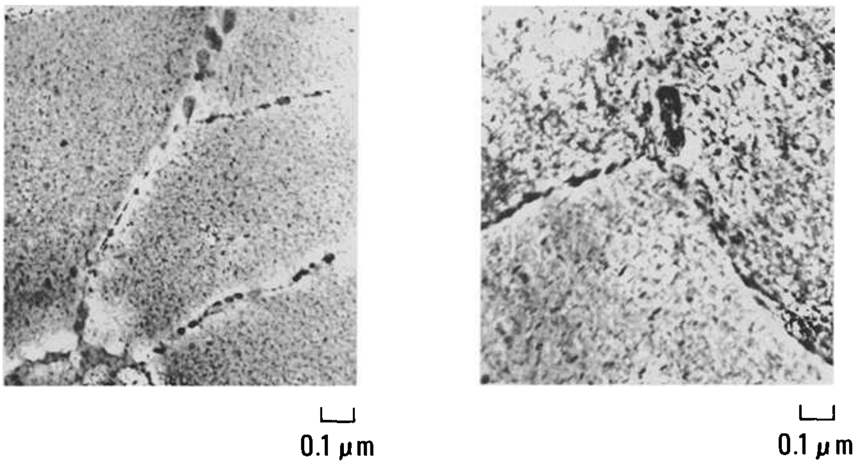

UNSTRETCHED

YIELD STRENGTH	ksi	(MPa)
L	78	(540)
LT	78	(540)
ST	77	(530)

STRETCHED 4%

YIELD STRENGTH	ksi	(MPa)
L	74	(510)
LT	71	(490)
ST	69	(475)

ALLOY 7050 PLATE AGED 24 HOURS AT 250 F (394 K) PLUS 14 HOURS AT 325 F (436 K)

FIG. 21—*Effects of stretching on the structure and tensile yield strength of alloy 7050 plate.*

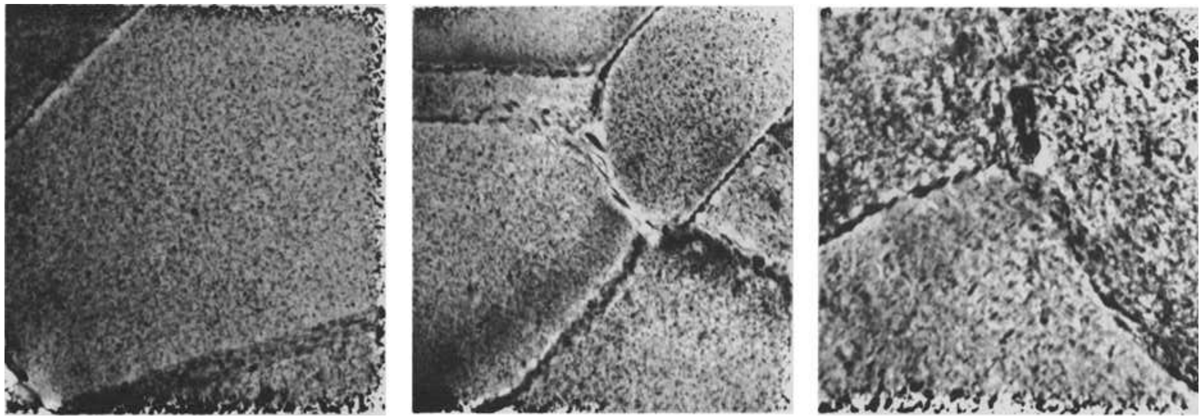

	UNSTRETCHED	1% STRETCH	4% STRETCH
	29 HOURS AT 325°F (436 K)	20 HOURS AT 325°F (436 K)	14 HOURS AT 325°F (436 K)
YIELD STRENGTH / ksi (MPa)	70.5 (486)	70.5 (486)	69.4 (478)
NTS/YS	1.34	1.20	1.10
ESTIMATED K_{Ic} / ksi $\sqrt{in.}$ (MPa $\sqrt{mm}$)	26 (900)	23 (800)	21 (730)

FIG. 22—*Effects of stretching on the structure and short-transverse notch toughness of alloy 7050 plate aged to the same yield strength.*

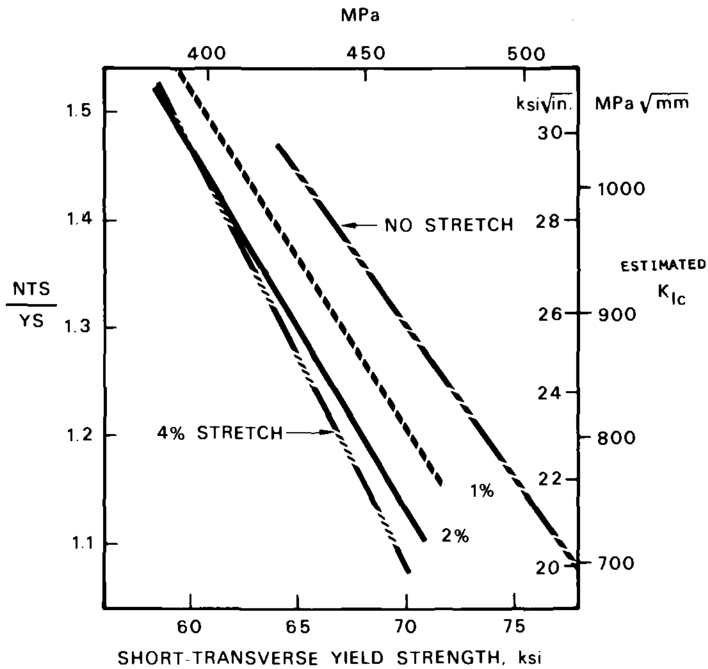

FIG. 23—*Effects of stretching on the relationship between strength and notch toughness of alloy 7050 plate.*

alloys are fairly well established. The following guidelines are offered to increase toughness by modifying these particles:

1. Minimize the volume fraction of insoluble constituents by increasing base purity.
2. Refine the size of soluble constituent particles by thermal-mechanical treatments.
3. Decrease the number of dispersoids by adjustments in chemistry or by thermal-mechanical treatments.
4. Quench as rapidly as possible.
5. Do not overage 2XXX alloy products.
6. Minimize cold work of 7XXX alloys before aging.
7. Where low residual stress is required, quench as rapidly as possible and mechanically stress relieve rather than quench slowly.
8. Age a lower-solute alloy to peak strength rather than overage a higher-solute alloy.
9. Reduce magnesium in 7XXX alloys to lowest level consistent with desired strength.
10. Where rapid quenching cannot be attained, as in plate, adjust practices to promote the lowest degree of recrystallization.

High-Toughness Alloys

New high-strength aluminum alloy products prepared according to these guidelines show promise of replacing older alloys for applications requiring high toughness with no sacrifice in strength.

Alloy 7475-T61 sheet [*14*] develops toughness approaching that of 2024-T3 at strength comparable to that of 7075-T6 sheet (Fig. 24) [*10,17,18*]. In the T761 temper, this material provides even higher toughness with strength and resistance to exfoliation corrosion comparable to that of 7075-T76 sheet. Alloy 7475-T651, T7651, and T7351 plate develop strength and corrosion resistance comparable to that of 7075 in corresponding tempers along with significantly improved toughness (Fig. 25). Because of its outstanding combination of strength and toughness, this alloy is being considered for several advanced designs and has been specified for the F-16.

Alloy 2124-T851 plate develops higher short-transverse elongation values than 2024-T851 plate along with higher fracture toughness in all directions, Fig. 26. It has seen extensive service on the F-111 and is in the F-14, F-5, B-1, and space shuttle.

Alloy 2048-T851 plate develops the toughness of alloy 2219-T851 plate at strength levels approaching those of alloy 2024-T851 plate [*19*]. It is currently being evaluated by the aerospace industry.

Other alloys contain controlled amounts of iron and silicon to provide

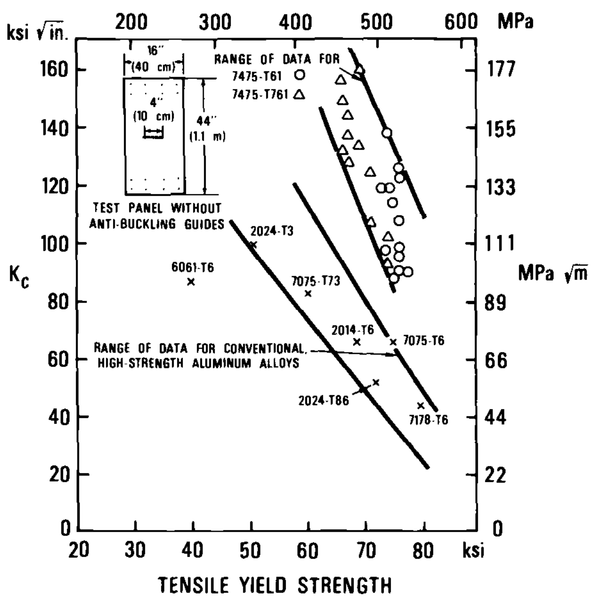

FIG. 24—K_c *of new alloy 7475 sheet relative to commercial alloy sheet.*

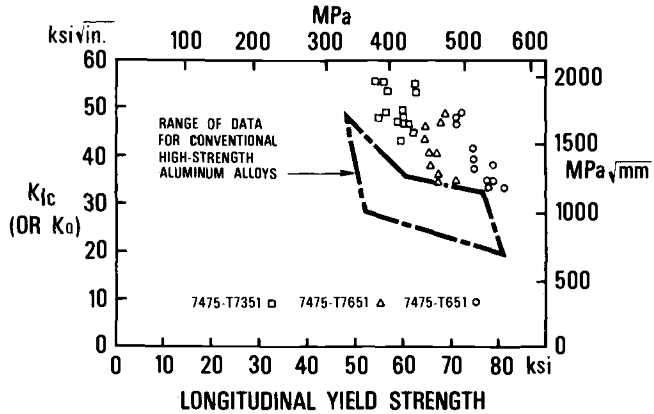

FIG. 25—K_{Ic} *of new alloy 7475 plate relative to commercial alloy plate.*

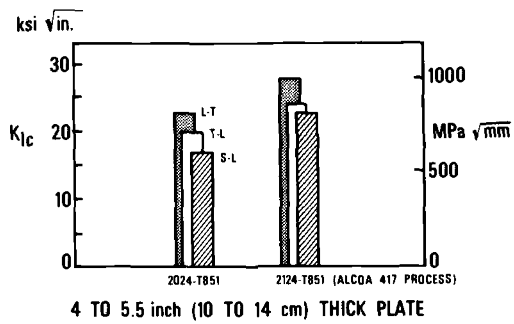

FIG. 26—K_{Ic} *of alloys 2024 and Alcoa 417 process 2124 plate.*

high toughness. Higher purity versions of alloys 2014 and 2219 which develop higher toughness than their standard purity counterparts have been evaluated. Moreover, the iron and silicon contents of alloy 7050 were established at low levels, and 7149, a higher purity version of 7049, has recently been registered with The Aluminum Association.

References

[*1*] Kaufman, J. G. and Hunsicker, H. Y. in *Fracture Toughness Testing and Its Applications, ASTM STP 381*, American Society for Testing and Materials, 1965, pp. 290-309.

[*2*] Kaufman, J. G. and Knoll, A. H., *Materials Research and Standards*, Vol. 4, No. 4, April 1964, p. 181.

[*3*] Kaufman, J. G. and Holt, M., "Fracture Characteristics of Aluminum Alloys," Alcoa Technical Paper 18, 1965.

[*4*] "Proposed Method for Sharp Notch Tension Testing of Thick, High-Strength Aluminum and Magnesium Alloys Products with Cylindrical Specimens," Part 10, *1974 Annual Book of ASTM Standards.*

[5] Carmen, C. M., Armiento, D. F., and Markus, H., *Transactions*, American Society of Mechanical Engineers, 1965, pp. 904-916.
[6] Piper, D. E., Quist, W. E., and Anderson, W. E., *Applications of Fracture Toughness to Structural Metals*, Vol. 31, Gordon and Breach, New York, 1966, pp. 227-280.
[7] Zinkham, R. E., Dedrick, J. H., and Jackson, J. H., *Proceedings of 5th International Leichtmetalltaging*, 1968.
[8] Fukui, T., *Journal of the Japan Institute of Metals*, Vol. 35, 1971, pp. 1035-1041.
[9] Van Stone, R. H., Marchant, R. H., and Low, J. R., Jr., *Fatigue and Fracture Toughness—Cryogenic Behavior, ASTM STP 556*, American Society for Testing and Materials, 1974, pp. 93-124.
[10] Nock, J. A. and Hunsicker, H. Y., *Journal of Metals*, Vol. 15, 1963, pp. 216-224.
[11] Staley, J. T. and Evancho, J. W., Final Report under Naval Air Systems Command Contract N00019-72-C-0146, 1972.
[12] Staley, J. T., "Fracture Toughness and Microstructure of High-Strength Aluminum Alloys," American Institute of Mining, Metallurgical, and Petroleum Engineers, Institute of Metals Division, Spring Meeting, May 1974.
[13] Rogers, R. W., Jr., Final Report under Contract DAAA25-68-C0771, June 1972.
[14] Rosenfield, A. R., Price, C. W., Martin, C. V., Williams, D. N., Drenn, D. C., Thompson, A. S., and Zinkham, R. E., AFML-TR-72-199, Part III, Air Force Materials Laboratory, Dayton, Ohio, 1973.
[15] Kirman, I., *Metallurgical Transactions*, Vol. 2, 1971, pp. 1761-1770.
[16] Hunsicker, H. Y. and Staley, J. T., U. S. Patent 3,791,880, 1974.
[17] Wang, D. Y., "Plane Stress Fracture Toughness and Fatigue Crack Propagation of Large Aluminum Alloy Sheet Panels," Paper presented at Sixth National Symposium on Fracture Mechanics, Philadelphia, Aug. 1972.
[18] Heyer, R. H. and McCabe, D. E., unpublished work at Armco Research.
[19] Levy, S. A., "X2048 Alloy—A High-strength, High-Toughness Alloy," Reynolds Metals publication, undated.

DISCUSSION

W. E. Quist,[1] *M. V. Hyatt,*[1] *and W. E. Anderson*[2] *(written discussion)*—We would like to compliment Dr. Staley on his excellent state-of-the-art summary on the relationship between microstructure and toughness in aluminum alloys. There is one area, however, concerning the effects of the impurity elements iron and silicon on the fracture toughness of 7000-series aluminum alloys, in which we would like to add some elaboration and perhaps correction. This seems particularly relevant in that essentially all new aluminum alloys in this system have very close restrictions on iron and silicon contents, imposed almost wholly to improve their fracture toughness characteristics.

It is commonly considered that the effects of iron and silicon on fracture toughness are quantitatively similar; both causing a degrading effect.[3,4]

[1] Research specialist, The Boeing Company, Seattle, Wash.

[2] Staff engineer, Battelle Northwest, Richland, Wash.

[3] Carman, C. M., Armiento, D. F., and Markus, H., "Plane-Strain Fracture Toughness of High-Strength Aluminum Alloys," *Transactions*, American Society of Mechanical Engineers, Dec. 1965, p. 904.

[4] Staley, J. T., this paper.

We have not found this to be the case, at least in a straight forward manner.

Effect of Iron

To our knowledge the effect of iron on the fracture toughness of 7075-7178 type alloys was discovered at Boeing in the 1961-1962 time frame.[5,6,7] Presentation (and application) of these findings was made to the Kaiser[8] and Alcoa[8] Aluminum Companies in 1961 and onward,[9] the Air Force Materials Laboratory in 1961,[10] the U. S. patent papers in 1963,[11] in the Masters thesis of W. E. Quist in 1963,[12] at the fall meeting of the American Institute of Mining, Metallurgical, and Petroleum Engineers in 1964,[13] and through the production of 60 000-70 000 lb of "low iron" 7178 for use on Boeing aircraft in 1964.[14] The principal effects that iron was found to cause in 7000-series alloys are as follows:

1. *Microstructure*—In commercial wrought 7000-series alloys, essentially all iron is found in the intermetallic phase Al_7Cu_2Fe. This massive constituent is one of the principal microstructural features in these types of alloys.[13]

[5] It should be pointed up that for many years the general effects on intermetallic phases, oxide particles, and the like, have been recognized as being detrimental to the ductility and formability characteristics of metals, and that this had resulted in an industry movement toward vacuum melting practices and other techniques to improve the "purity" of various engineering alloys. Incidently Dr. Staley's Ref *10* (our footnote 6), which purportedly establishes Alcoa as the initial observer of the effects of iron (and silicon) on fracture toughness does not, in fact, describe these relationships. We are aware, however, of earlier unpublished work at Alcoa (1961) which was initiated in response to visits by Boeing personnel, and which did investigate the effects of iron (and other elements) on fracture toughness.

[6] Nock, J. A. and Hunsicker, H. Y., *Journal of Metals,* March 1963, p. 216.

[7] Boeing Internal Reports: (1) C/S MS 2515, "Status Report on 7000-Series Aluminum Alloy Development Program," W. E. Quist to A. C. Larson, 4 Oct. 1961 and (J2) C/S MS 2889, "Status of Fracture Toughness Research on 7000-Series Alloys," W. E. Quist to A. C. Larson, 19 Jan. 1962.

[8] Products of experimental alloys used in the Boeing studies.

[9] Private communications, W. E. Quist and W. E. Anderson with (1) Alcoa (H. Y. Hunsicker, J. G. Kaufman and others), 3 and 4 May 1961 and onward and (2) Kaiser Aluminum Co. (F. W. DeMoney and others), 1961 and onward.

[10] Private communication, W. E. Quist and W. E. Anderson with the Air Force Materials Laboratory, Dayton, Ohio, 1961.

[11] Anderson, W. E. and Quist, W. E., U.S. Patent No. 3,284,193, filed 5 Dec. 1963, granted 8 Nov. 1966.

[12] Quist, W. E. "Effect of Composition on the Fracture Properties of Aluminum Alloy 7178," Masters thesis University of Washington, Seattle, Wash., May 1963.

[13] Piper, D. E., Quist, W. E., and Anderson, W. E., "The Effect of Composition on The Fracture Properties of 7178-T6 Aluminum Alloy Sheet," presented at the Fall Meeting, Institute of Mining, Metallurgical, and Petroleum Engineers, 1964. published: *Application of Fracture Toughness Parameters to Structural Metals,* Gordon and Breach, New York, Vol. 31, 1966, pp. 227-280.

[14] Purchase orders to Kaiser Aluminum and Reynolds Aluminum for 60000 to 70000 lb of "low iron" 7178 (other chemistry adjustments also), June 1964. Receipt of material by The Boeing Company, Seattle, Wash., began Aug. 1964.

2. *Strength*—Increased iron contents bring about an increase in the quantity of Al_7Cu_2Fe particles, and the copper contained in this constituent is unavailable for taking part in solid solution and precipitation hardening. It was independently determined that copper is not a major strengthening element in commercial 7000-series alloys, however,[13,15] and thus it is not surprising to find that iron contents up to ~ 0.50 percent do not cause major changes in yield or ultimate strengths. Examples of this behavior are shown in Fig. 27, where several alloy groups with varying iron contents are compared. (Alloys connected by solid lines have a similar chemistry except for iron.) Composition, strength, and fracture data are presented in Tables 2 and 3.

3. *Fracture Toughness*—Iron causes the fracture toughness of 7075-type alloys to decrease precipitously as iron contents are increased from 0 to 0.5 percent. See Figs. 28 and 29 for the effect of iron on several alloy compositions. It is emphasized that other composition variables (and heat treatments) were held as constant as possible in these tests, an important prerequisite to a straightforward analysis.

It recently has been suggested that a causal relationship exists between the grain size of certain of these alloys and their fracture toughness.[16] We believe this correlation is coincidental, as the grain sizes in these alloys were much too large to permit a normal Petch type fracture or strengthen-

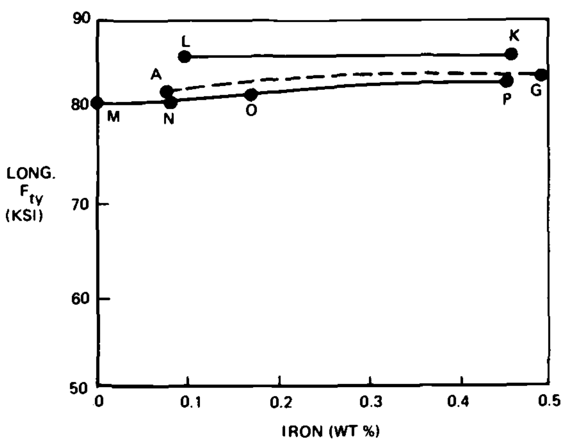

FIG. 27—*Effect of iron on yield strength (footnote 15).*

[15] Quist, W. E. and Hyatt, M. V., "The Effect of Chemical Composition on the Fracture Properties of Al-Zn-Mg-Cu Alloys,"*Proceedings,* American Institute of Aeronautics and Astronautics American Society of Mechanical Engineers. Seventh Structures and Materials Conference, Cocoa Beach, Fla.

[16] Rosenfield, A. R., Price, C. W., Martin, C. J., Thompson, D. S., and Zinkham, R. E., "Research on Synthesis of High-Strength Aluminum Alloys," Report No. AFML-TR-74-129, Air Force Materials Laboratory, Dayton, Ohio, Dec. 1974.

TABLE 2—*Chemical compositions of several 7075-7178 type experimental alloys, weight percent (footnotes 13 and 15).*

Alloy	Cu	Fe	Si	Mn	Mg	Zn	Ni	Cr	Ti	V	Be
A	2.27	0.09	0.08	0.11	2.66	6.58	0.002	0.18	0.03	0.005	0.003
G	2.36	0.48	0.09	0.11	2.68	6.58	0.003	0.17	0.02	0.005	0.003
K	1.52	0.45	0.06	0.11	2.59	7.25	0.002	0.24	0.03	0.006	0.001
L	1.50	0.09	0.06	0.10	2.61	7.28	0.002	0.23	0.03	0.006	0.002
M	1.48	0.00	0.06	0.11	2.61	6.47	0.002	0.23	0.03	0.009	0.001
N	1.49	0.08	0.06	0.11	2.56	6.42	0.002	0.21	0.03	0.006	0.002
O	1.50	0.17	0.05	0.11	2.58	6.52	0.002	0.22	0.03	0.008	0.002
P	1.53	0.44	0.05	0.12	2.61	6.51	0.002	0.21	0.03	0.006	0.002
R	1.49	0.09	0.20	0.12	2.57	6.45	0.002	0.22	0.03	0.006	0.002
30	1.42	0.11	0.47	0.10	2.43	6.39	...	0.20	0.02	...	0.002
31	1.46	0.10	0.20	0.11	2.90	6.32	...	0.25	0.03	...	0.002

TABLE 3—*Tensile and fracture toughness properties of experimental alloy series*[a] *(footnotes 13 and 15).*

Alloy No.	Tensile[b] Strength, psi	Yield[b] Strength, psi	Elongation[b] % in 2 in.	k_c psi$\sqrt{\text{in.}}$	G_c, in-lb/in.^{2}	γ, psi/s
A	90 100	82 200	15	45 800	202	1.2×10^5
				45 662	200	1.6×10^5
G	92 000	84 000	13	38 320	141	1.4×10^5
				34 385	114	1.2×10^5
				39 242	148	1.2×10^5
				37 381	141	6.1×10^4
K	92 500	86 500	12	31 159	93	6.4×10^4
				31 195	94	6.5×10^4
L	92 100	86 200	13	47 023	213	5.6×10^4
				41 369	166	6.0×10^4
M	87 500	81 100	13	57 959	323	5.5×10^4
				60 050	347	5.6×10^4
N	88 800	81 700	13	53 173	272	5.6×10^4
				52 978	270	6.1×10^4
O	89 500	83 100	11	48 777	229	5.7×10^4
				46 261	206	5.6×10^4
P	90 300	84 100	11	40 429	157	7.6×10^4
				40 482	158	2.3×10^5
R	85 800	78 900	14	60 636	353	3.5×10^4
				61 061	358	8.0×10^3
30	76 400	69 300	13	66 400	427	3.0×10^5
				68 400	453	2.9×10^5
31	87 800	81 600	12.5	40 800	162	2.8×10^5
				45 400	200	2.8×10^5

[a] Longitudinal grain direction for 0.16-in.-thick sheet.
[b] Average value of at least two separate determinations.
[c] All data taken from center cracked panels.

$$K_c = \sigma_g \left[W \tan \frac{\pi}{W} \left(a + \frac{k_c^2}{2\pi\sigma_{ys}^2} \right) \right]^{1/2} \quad \text{(graphical solution)}$$

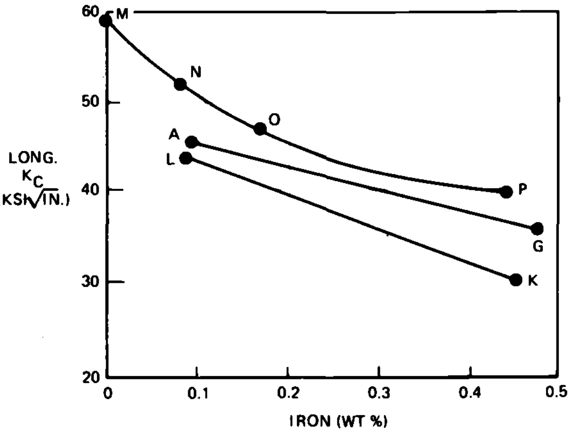

FIG. 28—*Effect of iron on toughness (footnote 15).*

ing mechanism to be operative. Furthermore, fracture paths in our alloys were completely transgranular, unlike those studied in footnote 16.

Effect of Silicon

We have found the effect of silicon on fracture toughness to be much different than that of iron, a point that did not become clear to us until 1966,[15] and which as yet has not become fully appreciated.[4] A summary of the effects of silicon on microstructure, strength, and fracture toughness are as follows:

1. *Microstructure*—In 7000-series alloys, silicon combines principally with aluminum, iron, and magnesium to form the massive silicon-bearing intermetallic compounds αAlFeSi and Mg_2Si, primarily the latter. The

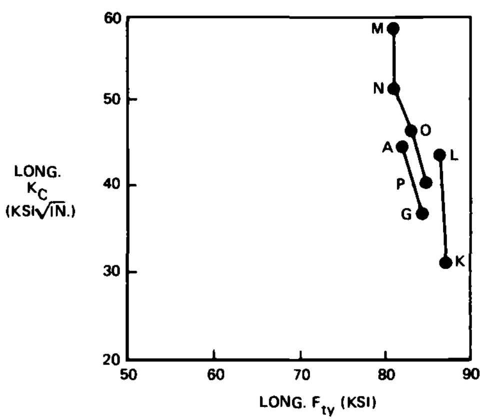

FIG. 29—*Effect of iron on toughness and yield strength (footnote 15).*

solution treating temperatures normally used for alloys in this system do not put the Mg_2Si phase into solution, and it remains as massive intermetallic particles randomly distributed throughout the microstructure.

2. *Strength*—In the Mg_2Si phase, the weight ratio of magnesium to silicon is ~1.73 to 1; thus, the presence of this phase prevents substantial quantities of the powerful strengthening element magnesium from performing its normal role in precipitation hardening. This causes a substantial decrease in both yield and ultimate strength. An example of this behavior is shown in Fig. 30 for experimental alloys *N*, *R*, and 30 where yield strength decreased from 81.7 to 69.3 ksi as silicon increased from 0.06 to 0.47 percent. See Tables 2 and 3 for composition, strength, and fracture data.

3. *Fracture Toughness*—Because of the observed formation of massive particles of αAlFeSi and Mg_2Si in the microstructure of 7000-series alloys as silicon is added, it has long been presumed by most observers that the effect of silicon on fracture toughness was degrading, similar to the effect of iron.[3,4] However, our studies did not confirm this assumption[13,15] and, in fact, showed a significant fracture toughness improvement as silicon was added. This behavior is illustrated by alloys *N*, *R*, and 30 in Fig. 31 where K_c increased from 53.1 to 67.4 ksi$\sqrt{\text{in.}}$ as silicon was increased from 0.06 to 0.47 percent. This result is somewhat understandable, since the toughness increase is accompanied by the just noted decrease in yield strength. The decreased strength is fully explainable by the formation of Mg_2Si particles, and the commensurate decrease in magnesium available for participation in hardening reactions.

In order to test whether Mg_2Si particles are inherently detrimental to toughness, independent of yield strength changes, a high silicon content

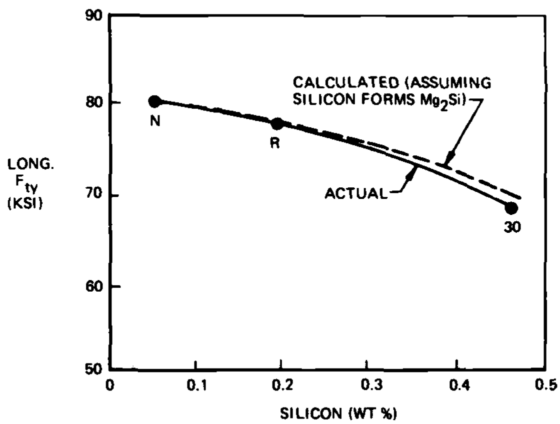

FIG. 30—*Effect of silicon on yield strength (footnote 15).*

TABLE 4—*Effect of Mg_2Si on fracture toughness (footnote 15).*

Alloy No.	Chemical Content, weight %											
	Zn	Mg	Cu	Fe	Si	Mn	Cr	E_{ty}, psi	F_{tu}, psi	Elongation, % in 2 in.	K_c, psi$\sqrt{\text{in.}}$	G_c, in·lb/in.^{2}
N	6.52	2.56	1.49	0.08	0.06	0.11	0.21	81 700	88 800	13.0	53,100	274
31	6.32	2.90	1.46	0.10	0.20	0.11	0.25	81 640	87 800	12.5	43,000	185

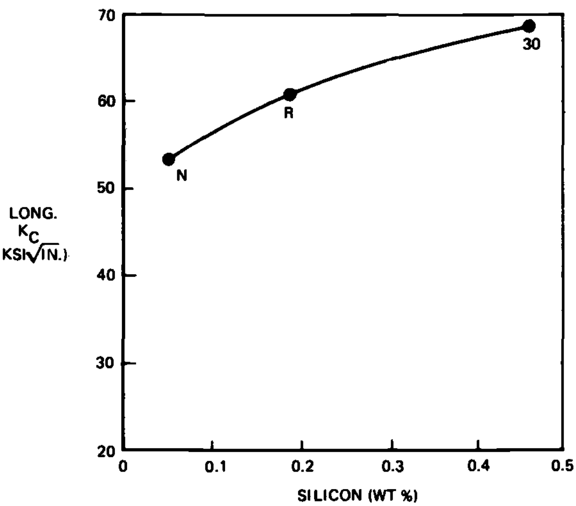

FIG. 31—*Effect of silicon on toughness (footnote 15).*

alloy was formulated (alloy 31) such that its yield strength was equivalent to a similar low silicon content alloy (alloy *N*). This was accomplished in alloy 31, by adding on extra amount of magnesium equivalent to that removed by its excess Mg_2Si particles.[15] The results are shown in Table 4. The fracture toughness of the high silicon content alloy is 43.0 ksi$\sqrt{\text{in.}}$ compared to 53.1 ksi$\sqrt{\text{in.}}$ for the low silicon content alloy, thereby demonstrating that the massive silicon bearing intermetallic particles are indeed detrimental.

From the preceding observations one deduces that the effect of lowering the iron content in established 7000-series commercial alloys will be to improve fracture toughness in a straightforward manner. For silicon content reductions, if a fracture toughness advantage is to be gained, and indeed it can be, then the nominal magnesium content of the alloy must be adjusted downward such that typical or average yield strengths are held constant. If this is not done the effect of reducing silicon content will be to increase yield strength and lower fracture toughness. For new alloys, a reduction of iron and silicon contents will bring straightforward advantages, as delta-yield-strength changes between an "old" and "new" alloy will not be a consideration.

It is hoped that these observations will clarify the important effects of iron and silicon on the fracture toughness of 7000-series alloys, at least to the extent that out studies have shown.

J. C. Newman, Jr.[1]

Fracture Analysis of Various Cracked Configurations in Sheet and Plate Materials

REFERENCE: Newman, J. C., Jr., "**Fracture Analysis of Various Cracked Configurations in Sheet and Plate Materials,**" *Properties Related to Fracture Toughness, ASTM STP 605,* American Society for Testing and Materials, 1976, pp. 104–123.

ABSTRACT: A two-parameter fracture criterion has been derived which relates the linear-elastic stress-intensity factor at failure, the elastic nominal failure stress, and two material parameters. The fracture criterion was used previously to analyze fracture data for surface- and through-cracked sheet and plate specimens under tensile loading. In the present paper the fracture criterion was applied to center-crack tension, compact, and notch-bend fracture specimens made of steel, titanium, or aluminum alloy materials tested at room temperature. The fracture data included a wide range of crack lengths, specimen widths, and thicknesses. The materials analyzed had a wide range of tensile properties. Failure stresses calculated using the criterion agreed well (± 10 percent) with experimental failure stresses. The criterion was also found to correlate fracture data from different specimen types (such as center-crack tension and compact specimens), within ± 10 percent for the same material, thickness, and test temperature.

KEY WORDS: fracture properties, fracturing, mechanical properties, stresses, cracks, plastic deformation

Nomenclature

c	Initial length of crack defined in Fig. 1, *m*
F	Boundary correction on the stress-intensity factor
K_F	Fracture toughness computed from Eq 2, N/m$^{3/2}$
K_I	Elastic stress-intensity factor, N/m$^{3/2}$
K_{Ie}	Elastic stress-intensity factor at failure, N/m$^{3/2}$
L	Major span length for notch-bend specimen, *m*
m	Fracture-toughness parameter
P	Applied load at failure, *N*

[1] Research engineer, NASA-Langley Research Center, Hampton, Va. 23665.

S Gross failure stress, N/m^2
S_n Elastic nominal stress (net section) at failure, N/m^2
S_u Nominal stress required to produce a fully plastic region on the net section, N/m^2
t Specimen thickness, m
W Specimen width, m
γ Function defined by Eq 6
λ Crack-length-to-specimen width ratio (defined in Fig. 1)
σ_u Ultimate tensile strength, N/m^2
σ_{ys} Uniaxial yield stress, N/m^2
ϕ Ratio of K_{Ic} to K_F

The concepts of linear-elastic fracture mechanics have been very useful in correlating fracture data for cracked plates and structural components in which the crack-tip plastic deformations are constrained to small regions (plane-strain fracture [*1*]).[2] However, for high-toughness sheet materials where large amounts of plastic deformation occur near the crack tip at fracture, the elastic stress-intensity factor at failure (K_{Ie}) varies with planar dimensions, such as crack length and specimen width [*2-5*]. To account for variation in K_{Ie} with crack length and specimen width, the elastic-plastic stress-strain behavior near the crack tip must be considered.

Several equations for calculating the elastic-plastic stress-strain behavior at notches or cracks have been proposed. Among these are equations derived for notches by Hardrath and Ohman [*6*], and by Neuber [*7*]. For cracks, equations have been derived by Hutchinson [*8*] and by Rice and Rosengren [*9*]. The Hardrath-Ohman equation was later generalized for a cracked plate and was applied as a fracture criterion by Kuhn and Figge [*10*]. In a similar way, Newman [*4,5*], using the Neuber relation and the elastic-stress distribution in the crack-tip region, derived a fracture criterion for a cracked plate which related the elastic stress-intensity factor at failure, the elastic nominal failure stress, and two material parameters. The two-parameter fracture criterion was used in Ref *4* to analyze failure of surface- and through-cracked sheet and plate specimens under tensile loading. This criterion was rederived in a more general form in Ref *5* and was used to analyze failure of compact and notch-bend sheet specimens.

In the present paper, the criterion was applied to center-crack tension, compact, and notch-bend sheet and plate specimens (Fig. 1) made of steel, titanium, or aluminum alloy materials tested at room temperature. The fracture data included a wide range of crack lengths, specimen widths, and thicknesses. The materials analyzed had a wide range of tensile properties.

[2] The italic numbers in brackets refer to the list of references appended to this paper.

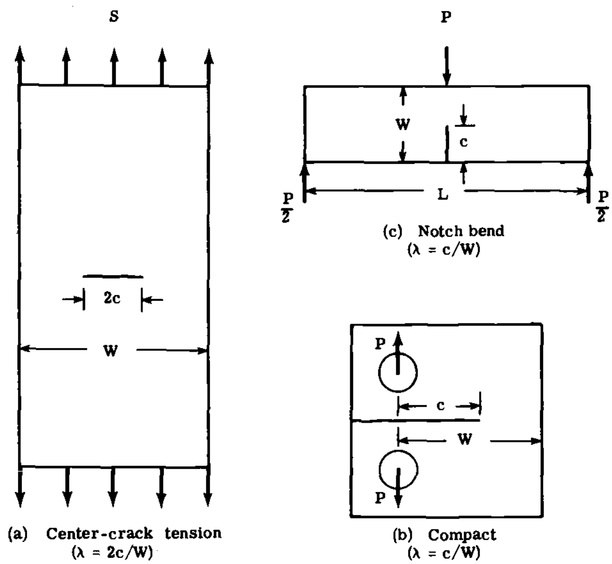

FIG. 1—*Center-crack tension, compact, and notch-bend specimen configurations.*

Two-Parameter Fracture Criterion

The elastic-stress distribution near a crack tip in an elastic material which contains the stress-intensity factor, K_I, and the square-root singularity is well known [*2*]. The determination of K_I is the basis for linear-elastic fracture mechanics. The stress-intensity factor is a function of the load, the configuration, and the size and location of the crack. In general, the elastic stress-intensity factor at failure for any cracked (Mode I) configuration can be expressed as

$$K_{Ie} = S_n \sqrt{\pi c}\, F \tag{1}$$

where S_n is the nominal failure stress (computed from the maximum load at failure) and c is the initial crack length. The boundary-correction factor, F, accounts for the influence of various boundaries on stress intensity. (Appendix I gives the equations for S_n and F for the center-crack, compact, and notch-bend specimens.) The use of the linear-elastic equation is restricted to conditions in which the plastic zone at the crack tip is very small compared to other dimensions of the body (brittle fracture [*1*]). Consequently, to analyze ductile materials, the elastic-plastic behavior of the stresses and strains near the crack tip must be considered.

A fracture criterion was derived [*4,5*] that accounts for the elastic-plastic behavior of the material. This criterion is

$$K_F = \frac{K_{Ie}}{1 - m\left(\frac{S_n}{S_u}\right)} \quad \text{for } S_n \leq \sigma_{ys} \tag{2}$$

where K_F and m are the two material parameters. The stress S_u (the ultimate value of elastic nominal stress) was computed from the load required to produce a fully plastic region or hinge [*11*] on the net section (based on the ultimate tensile strength, σ_u). For the center-crack tension specimen S_u is equal to σ_u. For the three-point notch-bend specimen S_u is 1.5 σ_u. For the compact specimen S_u is a function of load eccentricity and is 1.62 σ_u for a c/W ratio of 0.5. (See Appendix I.)

The fracture parameters K_F and m are assumed to be constant in the same sense as the ultimate tensile strength; that is, the parameters may vary with material thickness, state of stress, temperature, and rate of loading. To obtain fracture constants that are representative for a given material and test temperature, the nominal failure stress must be less than σ_{ys}, the fracture data should be from a single batch of material of the same thickness, and from tests that encompass a wide range of specimen width or crack length.

If m is equal to zero in Eq 2 K_F is equal to the elastic stress-intensity factor at failure, and the equation represents behavior of low-toughness materials (plane-strain fracture). If m is equal to unity the equation represents behavior of high-toughness materials (plane-stress fracture) [*4,5*]. Thus, the fracture-toughness parameters, K_F and m, describe the crack sensitivity of the material.

The denominator in Eq 2 reflects the influence of the nominal failure stress on fracture toughness. The variation of the denominator with nominal stress for a typical material is shown in Fig. 2. When the nominal stress is less than the uniaxial yield stress, σ_{ys}, the function ϕ (ratio of K_{Ie} to K_F) is a linear function of nominal stress (solid line). The line has a negative slope, m. However, when the nominal failure stress is greater than the yield stress, the function ϕ becomes nonlinear and is dependent upon the stress-strain curve of the material and the state of stress in the crack-tip region, as discussed in Ref *4*. For thin materials, where the state of stress in the crack-tip region is biaxial, the expected behavior is estimated by the dash-dot curve. An equation was chosen to give a simple approximation to the dash-dot curve and is given by

$$\phi = \frac{K_{Ie}}{K_F} = \frac{\sigma_{ys}}{S_n}\left(1 - m\,\frac{S_n}{S_u}\right) \tag{3}$$

for $\sigma_{ys} < S_n < S_u$ and is shown by the dashed curve. The vertical dashed line truncates the nominal stress at S_u. For thick materials, where the state of stress in the crack-tip region is triaxial, the fracture behavior for

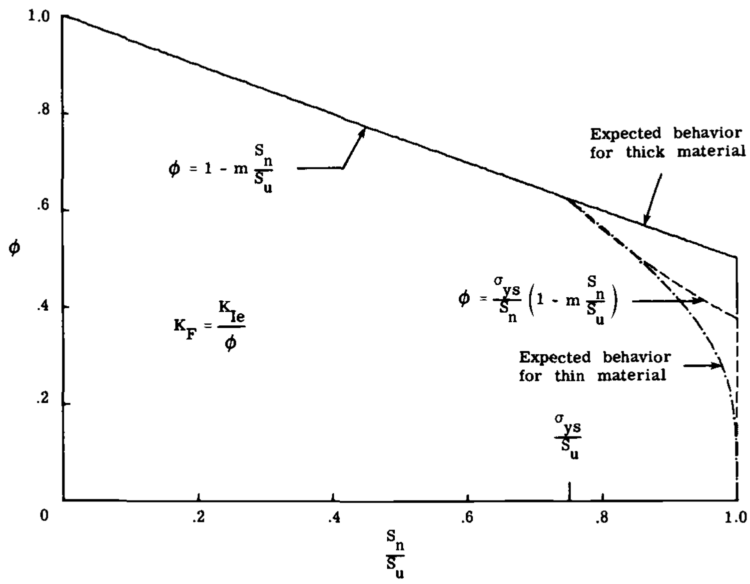

FIG. 2—*Relationship between ϕ and* S_n/S_u.

$S_n > \sigma_{ys}$ is expected to lie closer to the solid line. The solid vertical line truncates the nominal stress at S_u. The function ϕ, described by the solid lines, was used in Refs *4* and *5*. In order to show the expected range of behavior for thickness, both the solid and dashed curves were used for $S_n > \sigma_{ys}$ in the section on "Analysis of Test Data."

Failure Predictions

After the fracture toughness parameters K_F and m have been determined from fracture tests on a given material and test temperature, Eqs 2 and 3 can be used to predict failure stresses for other cracked configurations. The failure stresses were calculated by substituting Eq 1 into Eqs 2 and 3, and were given by

$$S_n = \frac{K_F}{\sqrt{\pi c}\,F + \dfrac{mK_F}{S_u}} \quad \text{for } S_n > \sigma_{ys} \tag{4}$$

and

$$S_n = \sqrt{(m\gamma)^2 + 2\gamma S_u} - m\gamma \quad \text{for } S_u > S_n \geqslant \sigma_{ys} \tag{5}$$

where

$$\gamma = \frac{K_F\sigma_{ys}}{2S_u\sqrt{\pi c}\,F} \tag{6}$$

Figure 3 shows the computed nominal failure stresses from Eqs 4 and 5 normalized to S_u for a typical material as a function of crack length in an infinite plate subjected to tensile loading. The tensile and fracture properties for this material are given in Fig. 3. The solid curve shows the calculations from Eq 4 for nominal failure stresses less than and greater than the yield stress of the material. For small crack lengths (less than about 1 mm for this material), Eq 4 predicts nominal failure stresses greater than S_u, but in these cases S_n was set equal to S_u. The dash-dot curve in Fig. 3, which shows the expected behavior for a thin material ($S_n > \sigma_{ys}$), was calculated by using the function ϕ, described by the dash-dot curve in Fig. 2. The dashed curve shows the calculations from Eq 5 for $S_n > \sigma_{ys}$. For stress levels greater than the yield stress, Eq 4 (solid curve) predicts failure stresses higher than expected for thin center-crack tension, compact, and notch-bend specimens made of ductile materials, but closely approximates the failure stresses for surface-cracked specimens [4]. Because the function ϕ, given by Eq 3, is a simple approximation to the expected behavior, Eqs 3 and 5 should be used only to estimate failure stresses for $S_n > \sigma_{ys}$ and not to obtain K_F and m from nominal failure stress in that range.

Analysis of Test Data

Fracture data from the literature on center-crack tension, compact, and notch-bend specimens made of steel, titanium, or aluminum alloy sheet and plate material were analyzed using the two-parameter fracture

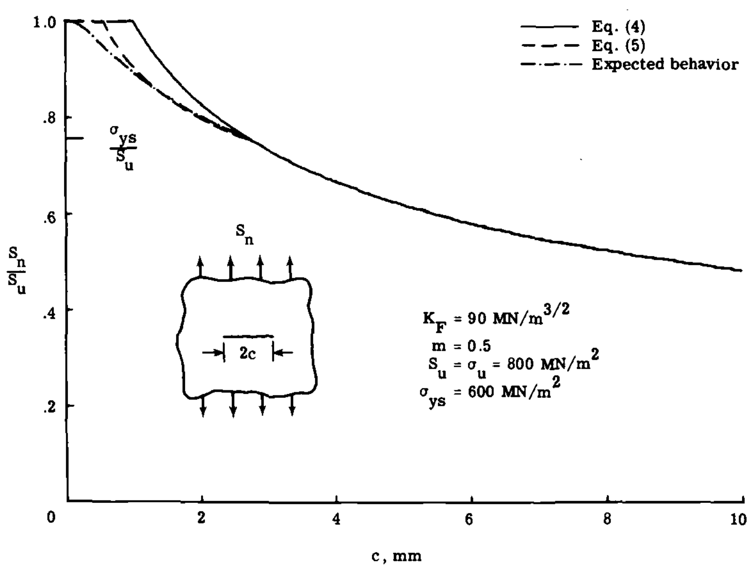

FIG. 3—*Computed nominal failure stresses as a function of crack length.*

criterion. The fracture constants, K_F and m, were determined from the fracture data using Eq 2 and a best-fit procedure [*4*]. In some cases, to illustrate that K_F and m are material parameters, they were determined from one type of specimen and were then used to predict the failure stresses for other types of specimens. In the following sections all of the fracture data are presented in terms of the elastic stress-intensity factor at failure, K_{Ie}. The experimental K_{Ie} values are compared with either calculated or predicted values as a function of crack length or specimen width. The calculated or predicted K_{Ie} values were obtained by substituting the failure stresses computed from Eq 4 or 5 into Eq 1 and were given by

$$K_{Ie} = \frac{K_F}{1 + \dfrac{mK_F}{S_u\sqrt{\pi c}\,F}} \quad \text{for } S_n \leq \sigma_{ys} \tag{7}$$

$$K_{Ie} = \{\sqrt{(m\gamma)^2 + 2\gamma S_u} - m\gamma\}\sqrt{\pi c}\,F \quad \text{for } S_u > S_n > \sigma_{ys} \tag{8}$$

and

$$K_{Ie} = S_u\sqrt{\pi c}\,F \quad \text{for } S_n = S_u \tag{9}$$

The "calculated" K_{Ie} values were obtained by a best fit of Eq 7 or 8 to the experimental data. The "predicted" values were obtained from Eq 7 or 8 where K_F and m were determined from fracture tests conducted on a different specimen type. Equation 7 was also used for $S_n > \sigma_{ys}$ in order to show the expected range of behavior for thickness as discussed previously.

Aluminum Alloy Specimens

Tests on 7075-T6 and 2024-T3—Fracture tests were conducted on center-crack tension specimens (Fig. 1*a*) made of 7075-T6 or 2024-T3 material (NASA Langley data, Table 1) to demonstrate that the fracture criterion applies over a wide range of material fracture toughness. The fracture data (square symbols for 7075-T6 and circular for 2024-T3) are shown in Fig. 4 as K_{Ie} plotted against crack-length-to-width ratio. The solid symbols denote tests for which S_n was greater than σ_{ys}. The K_{Ie} values for the 7075-T6 were nearly constant, as expected, for a low-toughness material (K_F = 31 MN/m$^{3/2}$). In contrast to the low-toughness behavior of the 7075-T6, the 2024-T3 sheet material exhibited a high-fracture toughness (K_F = 267 MN/m$^{3/2}$). Because the failure stresses for the 2024-T3 specimens were nearly equal to the yield stress of the material, K_{Ie} varied significantly with crack length. The solid curves show

TABLE 1—*Nominal failure stresses for center-crack tension specimens of 7075-T6 plate and 2024-T3 sheet material.*

7075-T6		2024-T3	
t = 12.7 mm W = 300 mm σ_u = 600 MN/m^2 σ_{ys} = 496 MN/m^2		t = 2.3 mm W = 300 mm σ_u = 490 MN/m^2 σ_{ys} = 356 MN/m^2	
c, mm	S_n, MN/m^2	c, mm	S_n, MN/m^2
8.5	170.6	6.4	364.4
13.0	142.3	12.7	356.1
13.2	135.7	25.4	344.2
17.3	135.3	50.8	329.4
51.4	111.1	76.2	321.3
73.9	92.31	01.5	321.8
101.3	93.0		

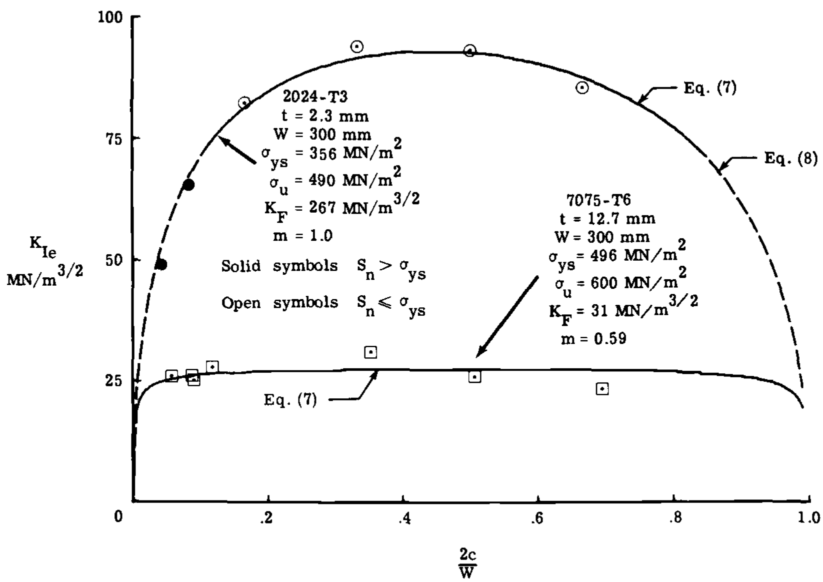

FIG. 4—*Elastic stress-intensity factors at failure for center-crack tension specimens made of 7075-T6 and 2024-T3 aluminum as a function of crack-length-to-width ratio.*

the calculated results from the fracture criterion (Eq 7) using the values of K_F and m determined from a best fit of these data. The dashed curves (at crack-length-to-width ratios less than 0.15 and greater than 0.85 for the 2024-T3 alloy) show the calculated behavior for $S_n > \sigma_{ys}$ using Eq 8. The calculations from Eq 7 for $S_n > \sigma_{ys}$ (not shown) nearly overlapped the dashed curve. For both materials, the calculated results were in good agreement with the experimental results.

Tests on 2219-T851—Kaufman and Nelson [12] conducted fracture tests on compact specimens (Fig. 1*b*) made of 2219-T851 plate material for various specimen thicknesses, widths, and crack lengths. The plate thickness analyzed was 25.4 mm, and the c/W ratio was 0.5. Figure 5 shows the experimental (symbols) and calculated (curves) K_{Ie} values plotted against specimen width. The fracture constants, K_F and m, were determined from these data ($S_n < \sigma_{ys}$). The solid symbols denote fracture tests for which S_n was greater than σ_{ys}. The solid and dashed curves were calculated using Eqs 7 and 8, respectively. Equation 7 was applied over the complete range of specimen widths, even though S_n was greater than σ_{ys}, to show that the two equations give about the same results (within 10 percent) for $W < 100$ mm. For wide specimens, the calculated K_{Ie} values approach the fracture toughness K_F (indicated by the dash-dot line).

The results of fracture tests conducted on 38-mm-thick compact specimens [12] at various c/W ratios for a constant specimen width (150 mm) are shown in Fig. 6*a*. The fracture constants $K_F = 65.8$ MN/m$^{3/2}$ and

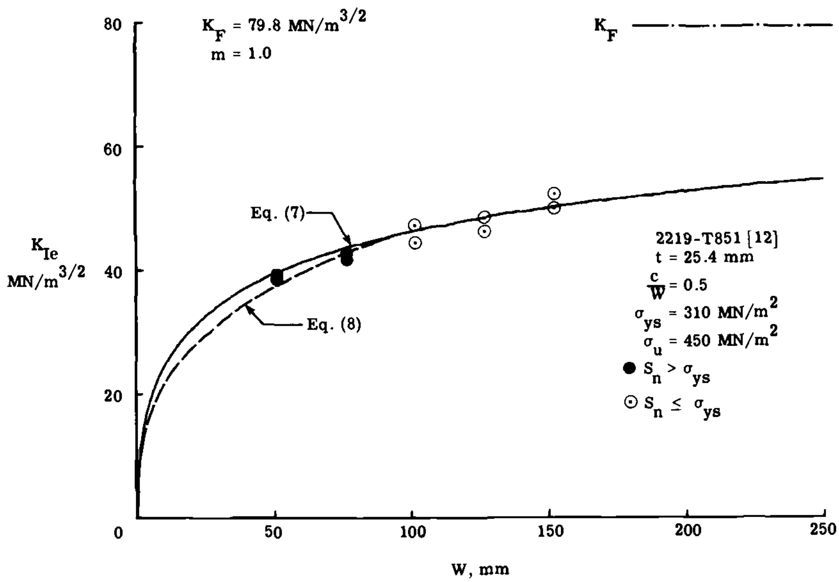

FIG. 5—*Elastic stress-intensity factors at failure for compact specimens made of 2219-T851 aluminum alloy as a function of specimen width.*

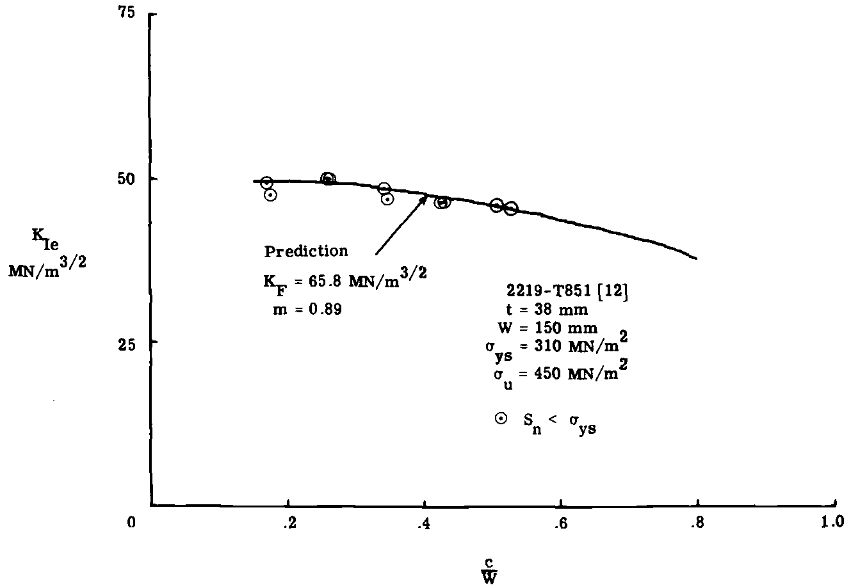

FIG. 6*a*—*Experimental and predicted elastic stress-intensity factors at failure for compact specimens made of 2219-T851 aluminum alloy as a function of crack-length-to-width ratio.*

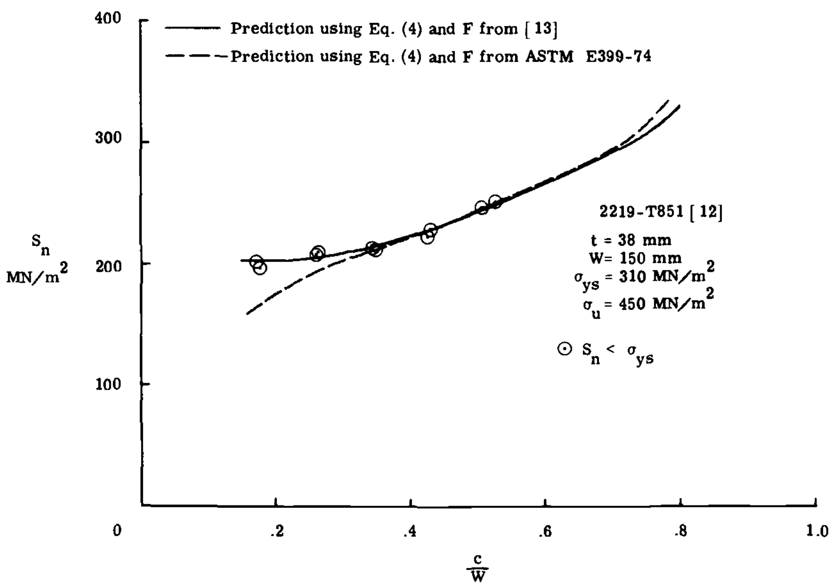

FIG. 6*b*—*Experimental and predicted nominal failure stresses for compact specimens made of 2219-T851 aluminum alloy as a function of crack-length-to-width ratio.*

$m = 0.89$ were obtained from data (not shown) on the same material and thickness where the c/W ratio was held constant at 0.5 and the specimen width was varied between 75 and 150 mm. Since these fracture properties were obtained from tests with a constant c/W, they do not inherently account for variations in K_{Ie} with c/W. The curve in Fig. 6*a* shows the predictions using Eq 7. The agreement between the experimental and predicted results is considered good. Figure 6*b* shows how the pin-loaded holes in the compact specimen influence nominal failure stresses. The symbols show the experimental failure stresses plotted against c/W for the same data shown in Fig 6*a*. The solid and dashed curves show the predictions using Eq 4 and the boundary-correction factors obtained with [*13*] and without (ASTM Test for Plane-Strain Fracture Toughness of Metallic Materials (E 399-74)) the pin-loaded holes. The good agreement between the experimental and predicted results (solid curve) at the small c/W ratios can be attributed to including the influence of the pin-loaded holes on stress intensity.

Tests on Hiduminium-48—Adams and Munro [*14*] conducted fracture tests on center-crack tension specimens made of Hiduminium-48, an aluminum alloy sheet material, over a wide range of crack lengths and specimen widths. The material thickness for all specimens was 3.2 mm. The experimental results (symbols) are presented in Fig. 7*a* as K_{Ie} plotted against $2c/W$ for the specimen widths ranging from 50 to 200 mm. The curves were calculated using Eq 7 or 8 depending on nominal stress levels, with $K_F = 405$ MN/m$^{3/2}$ and $m = 0.95$ (best fit to these data). The two-parameter fracture criterion correlated the data within ±4 percent for all crack lengths and specimen widths. (The solid curves for $S_n > \sigma_{ys}$ nearly overlapped the dashed curves and were not shown to simplify the plot.)

Adams and Munro [*14*] also conducted fracture tests on compact specimens made of the same Hiduminium-48 sheet material previously described. The compact specimen fracture data were analyzed using the fracture constants, K_F and m, determined from the center-crack tension specimens. Figure 7*b* shows the experimental (symbols) and predicted (dashed curve) K_{Ie} values plotted against specimen width. The predicted K_{Ie} values fell within ±10 percent of the experimental results, even though the nominal failure stresses were 20 to 50 percent higher than the yield stress of the material. The solid curve, predicted from Eq 7, is about 15 percent higher than the experimental K_{Ie} values. These predictions also indicate that specimen widths much larger than 250 mm would be required to obtain failures with $S_n < \sigma_{ys}$.

Tests on 7075-T6 Clad and 2014-T3—Bradshaw and Wheeler [*15*] conducted fracture tests on center-crack tension and compact specimens made of four different aluminum alloy sheet materials. All specimens were 1.6 mm thick. Only the analysis of the materials with the highest and lowest yield stress (7075-T6 clad and 2014-T3, respectively), are shown.

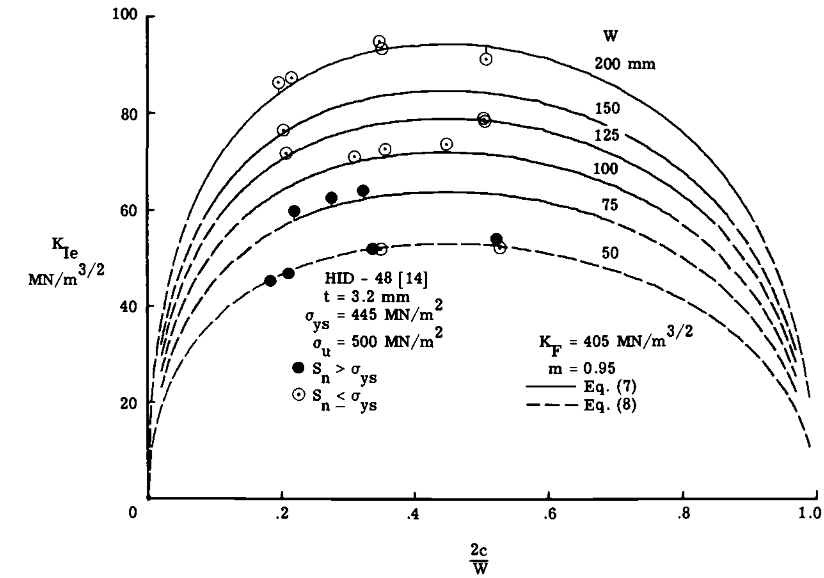

FIG. 7a—*Elastic stress-intensity factors at failure for center-crack tension specimens made of Hiduminium-48 sheet material.*

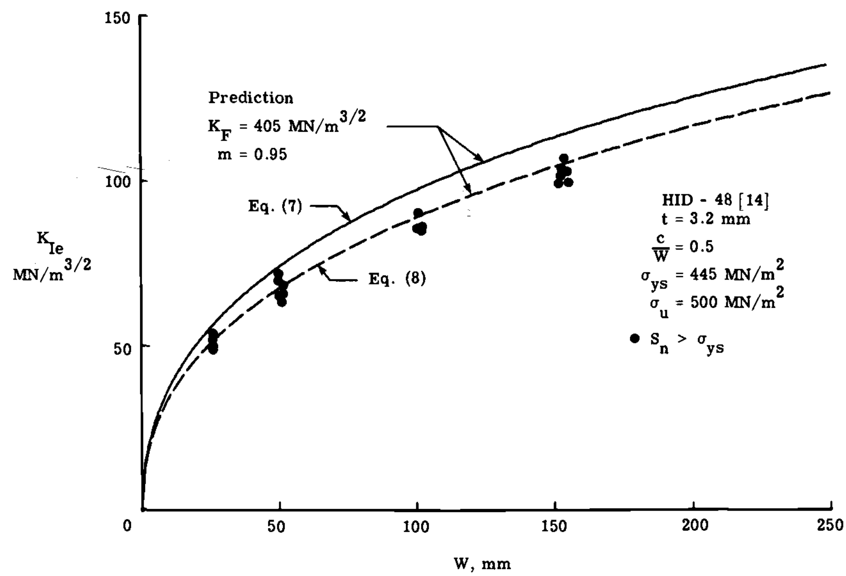

FIG. 7b—*Experimental and predicted elastic stress-intensity factors at failure for compact specimens made of Hiduminium-48 sheet material as a function of specimen width.*

The fracture constants, K_F and m, for the two aluminum alloys were determined from an analysis of the center-crack specimen data (not shown). The center-crack specimens were either 250 or 750 mm wide and the crack-length-to-width ratio ranged from 0.1 to 0.5. The fracture properties $K_F = 77.6$ MN/m$^{3/2}$ and $m = 0.43$ were obtained from the 7075-T6 data and $K_F = 273$ MN/m$^{3/2}$ and $m = 1$ from the 2014-T3 data.

The fracture properties determined from the center-crack tension specimens were then used to predict the failure of the compact specimens. The elastic stress-intensity factor for the compact specimens used in Ref *15*, which were not standard ASTM Method E 399-74 specimens, was

$$K_I = \frac{P}{t\sqrt{W}} 3.7 \text{ for } \frac{c}{W} = 0.17 \tag{10}$$

Figure 8 shows the experimental K_{Ie} values (symbols) plotted against specimen width for the 7075-T6 clad material. The solid and dashed curves show the predicted K_{Ie} values using Eq 7 and 8, respectively. The predicted behavior was within ±7 percent of the experimental results.

Figure 9 shows the experimental (symbols) and predicted (dashed curve) K_{Ie} values plotted against specimen width for the 2014-T3 compact specimens. The nominal failure stresses for all of the specimens were greater than σ_{ys}. The dashed curve shows the predicted behavior using Eq 8 with the values of K_F and m that were determined from the center-crack

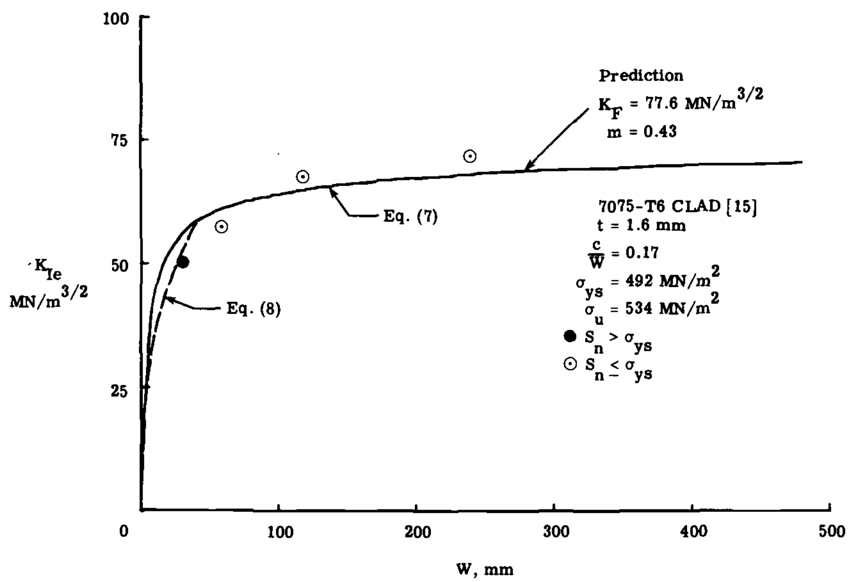

FIG. 8—*Experimental and predicted elastic stress-intensity factors at failure for compact specimens made of 7075-T6 clad aluminum alloy as a function of specimen width.*

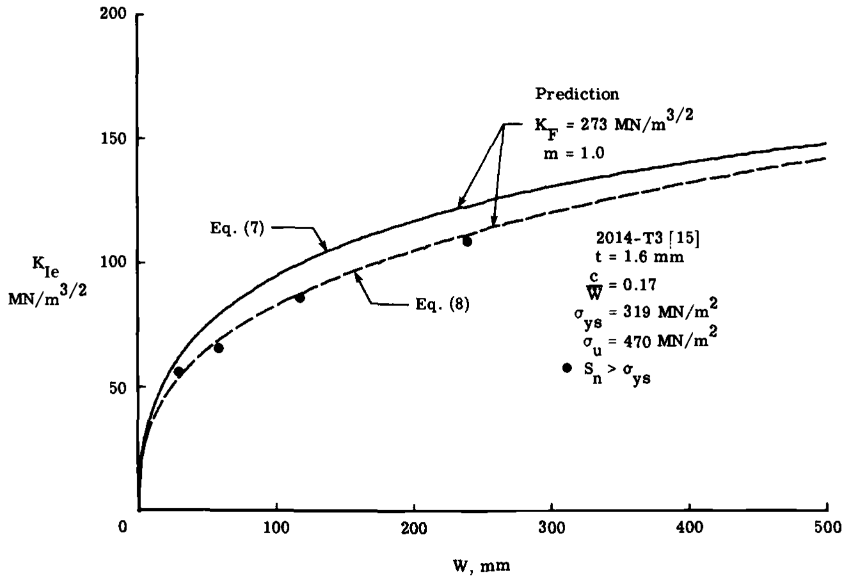

FIG. 9—*Experimental and predicted elastic stress-intensity factors at failure for compact specimens made of 2014-T3 aluminum alloy as a function of specimen width.*

specimen fracture data. The predicted behavior was within ±5 percent of the experimental results. Again, the solid curve shows how Eq 7 overpredicts the experimental failure stresses for thin materials when the nominal failure stresses are greater than σ_{ys}.

Ti-6Al-4V Titanium Alloy Specimens

Gunderson (Air Force Materials Laboratory, AFML-MXE 73-3) conducted fracture tests on compact specimens made of a beta-processed mill-annealed plate of Ti-6Al-4V (25.4 mm thick). Figure 10 shows the experimental (symbols) and calculated (curves) K_{Ie} values plotted against specimen width. The c/W ratio for these data was 0.5. The values of K_F and m used in the calculations were determined from an analysis of these data. The calculated results (solid and dashed curves) for $c/W = 0.5$ agreed well with the experimental results. The curves for $c/W = 0.2$ and 0.8 show how K_{Ie} varies as a function of c/W. These results indicate that for larger c/W ratios wider specimens are required to obtain $S_n < \sigma_{ys}$ (intersection of solid and dashed curves denote where $S_n = \sigma_{ys}$). All three curves approach the fracture toughness, K_F (dash-dot line), for very wide specimens.

4340 Steel Specimens

Jones and Brown [16] conducted fracture tests on three-point notch-bend specimens (Fig. 1*c*) made of 4340 steel with several strength levels.

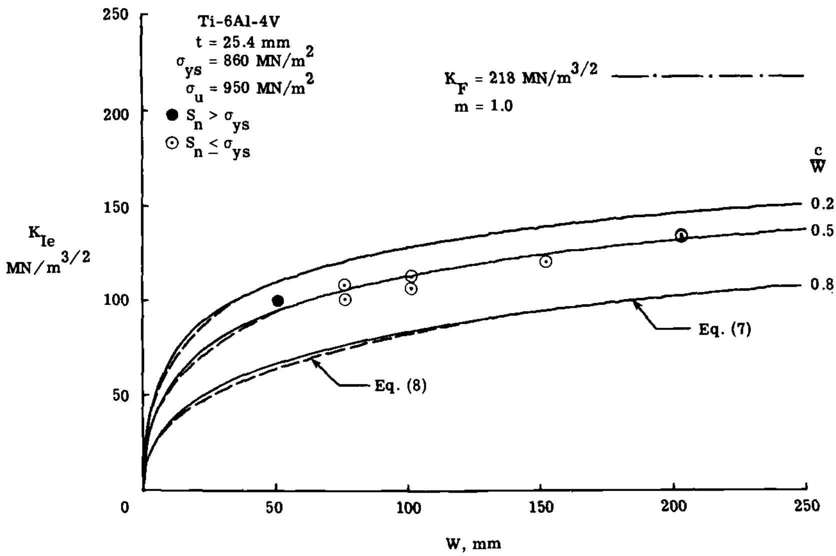

FIG. 10—*Elastic stress-intensity factors at failure for compact specimens made of Ti-6Al-4V titanium alloy as a function of specimen width.*

These tests were conducted to determine the influence of thickness, crack length, and specimen width on fracture toughness. Figure 11 shows the results of fracture tests (symbols) conducted on 1.3 and 25.4-mm-thick specimens with $c/W = 0.5$ for various specimen widths. The curves were calculated using either Eq 7 or 8 with K_F and m determined by a best fit for each material thickness. For the thin material, all of the test data had nominal failure stresses greater than the yield stress of the material. Therefore, the values of K_F and m were determined using Eq 8. (The values of K_F and m should have been obtained from testing specimens with widths greater than 75 mm where the nominal failure stresses would have been less than σ_{ys}, but no fracture data were available with widths greater than 75 mm.) For the thicker material, K_F was equal to K_{Ic}, the plane-strain fracture toughness, and K_{Ie} was equal to K_{Ic}, the plane-strain fracture toughness, and K_{Ie} values were independent of specimen width.

Plane-Stress and Plane-Strain Fracture

The two-parameter fracture criterion derived in Refs *4* and *5* gave a linear relationship between K_{Ie} and the nominal failure stress, S_n, for $S_n < \sigma_{ys}$. The three-dimensional diagram in Fig. 12 shows how the experimental values of K_{Ie} (square symbols) vary as a function of nominal failure stress (normalized to S_u) and plate thickness for compact specimens made of 2219-T851 aluminum alloy [*12*]. The experimental relationship between K_{Ie} and S_n is, also, approximately linear. The three-

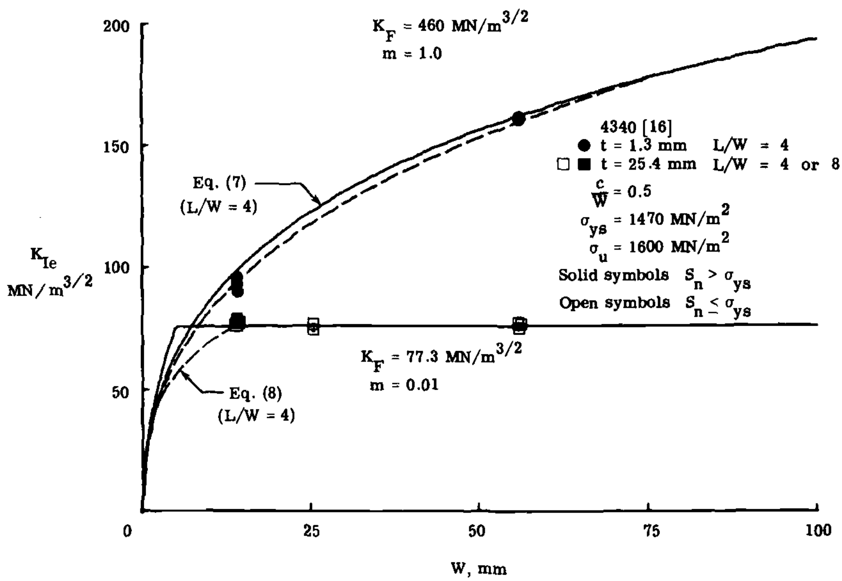

FIG. 11—*Elastic stress-intensity factors at failure for three-point notch-bend specimens made of 4340 steel (two thicknesses) as a function of specimen width.*

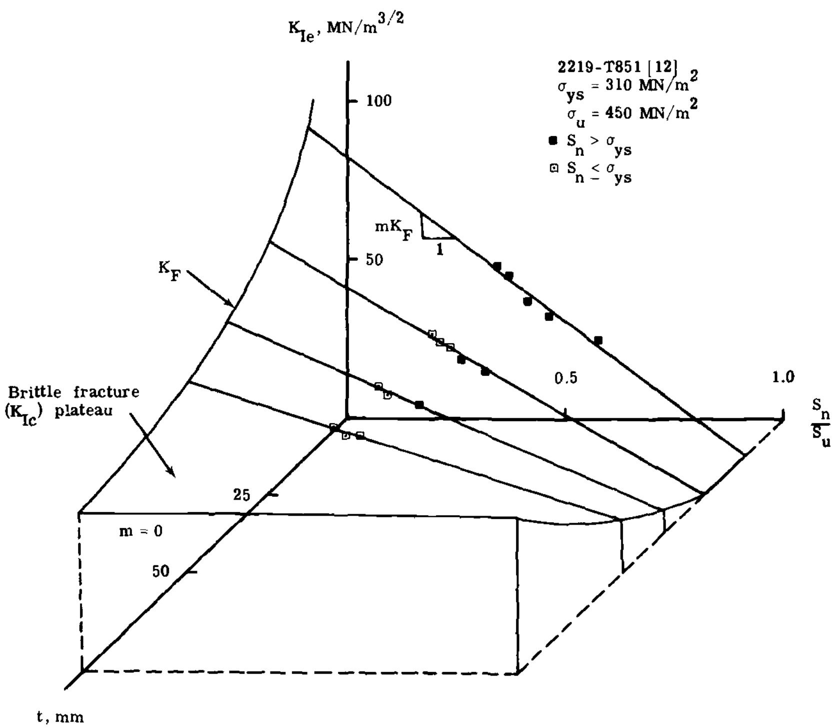

FIG. 12—*Elastic stress-intensity factors at failure for compact specimens made of 2219-T851 alloy as a function of nominal failure stress and thickness.*

dimensional surface, formed by the straight-line generators (solid lines), is the locus of K_{Ie} values for various combinations of specimen dimensions. The ASTM Method E 399-74 is intended to produce a constant value of plane-strain fracture toughness, K_{Ic}. Such behavior would produce a plateau near the left extremity of the surface shown (with $m = 0$). For many materials of practical interest the specimens required to produce plane-strain fracture are so large that testing is very difficult, if not impossible. Thus, the two-parameter fracture criterion can be useful for computing fracture toughness and predicting failure stresses for structural materials which fracture under either plane-stress or plane-strain conditions.

Concluding Remarks

A two-parameter fracture criterion that relates the elastic stress-intensity factor at failure, the elastic nominal failure stress, and two material parameters was used to analyze fracture data on center-crack tension, compact, and notch-bend specimens made of steel, titanium, or aluminum alloy materials tested at room temperature. The specimens had a wide range of crack lengths, specimen widths, specimen thicknesses, and material properties. The fracture criterion correlated the data well (generally within ± 10 percent of the experimental failure stresses) for a broad range of materials, including some regarded as very ductile. The two fracture parameters, K_F and m, were found to be nearly independent of crack length and specimen width for a given material and specimen thickness. The fracture parameters did vary as a function of material and specimen thickness. The fracture criterion was also found to correlate fracture data from different specimen types (such as center-crack tension and compact specimens), within ± 10 percent for the same material, thickness, and test temperature.

APPENDIX I

Elastic Stress-Intensity Factors and Nominal Stress Definitions for the Center-Crack Tension, Compact, and Notch-Bend Specimens

In the application of Eqs 2 and 3 to center-crack tension, to compact, and to notch-bend specimens, the stress-intensity factor, the nominal stress, and S_u must be determined as a function of crack length and specimen width. The following sections give these equations.

Center-Crack Tension Specimen

For the center-crack specimen (Fig. 1*a*), the elastic stress-intensity factor is given by Eq 1

where

$$S_n = \frac{S}{1 - \lambda} \tag{11}$$

and

$$F = (1 - \lambda)\sqrt{\sec\left(\frac{\pi\lambda}{2}\right)} \tag{12}$$

for $0 \leq \lambda < 1.0$ where λ is the crack-length-to-width ratio. The secant term is the finite-width correction on stress intensity and was obtained from Ref *1*.

The ultimate value of elastic nominal stress, S_u, for the center-crack specimen is σ_u.

Notch-Bend Specimen

For the notch-bend specimen (Fig. 1*c*), the elastic stress-intensity factor is given by Eq 1

where

$$S_n = \frac{3PL}{t(W - c)^2} \tag{13}$$

and

$$F = (1 - \lambda)^2 \quad \frac{f(\lambda)}{\sqrt{\pi}} \tag{14}$$

The function $f(\lambda)$, obtained from Ref 1, was given by

$$f(\lambda) = A_0 + A_1\lambda + A_2\lambda^2 + A_3\lambda^3 + A_4\lambda^4 \tag{15}$$

L/W	A_0	A_1	A_2	A_3	A_4
4	1.93	−3.07	14.53	−25.11	25.80
8	1.96	−2.75	13.66	−23.98	25.22

for $0 \leq \lambda \leq 0.6$. Equation 15 is within 0.2 percent of the more accurate values [*17*] for c/W ratios (λ) up to 0.6 and is 3.5 percent lower than the correct value at a c/W ratio of 0.7.

The ultimate value of elastic nominal stress, S_u, for the notch-bend specimens is 1.5 σ_u. This was computed from the load required to produce a fully plastic hinge on the net section using the ultimate tensile strength.

Compact Specimen

For the compact specimen (Fig. 1*b*), the elastic stress-intensity factor is, again, given by Eq 1

where

$$S_n = \frac{P}{t(W - c)}\left[1 + 3 \quad \left(\frac{1 + \lambda}{1 - \lambda}\right)\right] \tag{16}$$

and

$$F = \frac{(1-\lambda)f(\lambda)}{\sqrt{\pi\lambda}\left[1 + 3\left(\frac{1+\lambda}{1-\lambda}\right)\right]} \tag{17}$$

The function $f(\lambda)$, obtained from Ref *13*, was given by

$$f(\lambda) = 4.55 - 40.32\,\lambda + 414.7\,\lambda^2 - 1698\,\lambda^3 + 3781\,\lambda^4 - 4287\,\lambda^5 + 2017\,\lambda^6 \tag{18}$$

for $0.2 \leq \lambda \leq 0.8$. Equation 18 includes the influence of the pin-loaded holes in the compact specimen.

The ultimate value of elastic nominal stress, S_u, for the compact specimen is a function of load eccentricity and is given by

$$S_u = \left\{\left[\sqrt{1 + \left(\frac{1+\lambda}{1-\lambda}\right)^2} - \left(\frac{1+\lambda}{1-\lambda}\right)\right]\left[1 + 3\left(\frac{1+\lambda}{1-\lambda}\right)\right]\right\}\sigma_u \tag{19}$$

For a range of λ between 0.2 and 0.8

$$S_u = 1.61\,\sigma_u \tag{20}$$

agrees to within 4 percent of that given by Eq 19.

References

[*1*] *Plane Strain Crack Toughness Testing of High Strength Metallic Materials, ASTM STP 410,* American Society for Testing and Materials, 1966.

[*2*] *Fracture Toughness Testing, ASTM STP 381,* American Society for Testing and Materials, 1964.

[*3*] Kuhn, P., "Residual Tensile Strength in the Presence of Through Cracks or Surface Cracks," TN D-5432, National Aeronautics and Space Administration, Washington, D.C., 1970.

[*4*] Newman, J. C., Jr., "Fracture Analysis of Surface- and Through-Cracked Sheets and Plates," *Engineering Fracture Mechanics Journal*, Vol. 5, 1973. (Presented at the Symposium on Fatigue and Fracture, George Washington University, May 1972.)

[*5*] Newman, J. C., Jr., "Plane Stress Fracture of Compact- and Notch-Bend Specimens," TM X-71926, National Aeronautics and Space Administration, Washington, D.C., 1973.

[*6*] Hardrath, H. F. and Ohman, L., "A Study of Elastic and Plastic Stress Concentration Factors Due to Notches and Fillets in Flat Plates," Report 1117, National Advisory Committee for Aeronautics, 1953 (supersedes NACA TN 2566).

[*7*] Neuber, H., *Transactions,* American Society of Mechanical Engineers, Series E, *Journal of Applied Mechanics,* Vol. 28, 1961, pp. 544-550.

[*8*] Hutchinson, J. W., *Journal of the Mechanics and Physics of Solids*, Vol. 16, 1968, pp. 13-31.

[*9*] Rice, J. R. and Rosengren, G. F., *Journal of the Mechanics and Physics of Solids,* Vol. 16, 1968, pp. 1-12.

[*10*] Kuhn, P. and Figge, I. E., "Unified Notch-Strength Analysis for Wrought Aluminum Alloys," TN D-1259, National Aeronautics and Space Administration, Washington, D.C., 1962.

[*11*] Timoshenko, S., *Strength of Materials,* Advanced Theory and Problems, D. Van Nostrand Co., New York, 1956.

[*12*] Kaufman, J. G. and Nelson, F. G. in *Fracture Toughness and Slow-Stable Cracking, ASTM STP 559,* American Society for Testing and Materials, 1974, pp. 74-85.

[13] Newman, J. C., Jr., *Fracture Analysis, ASTM STP 560,* American Society for Testing and Materials, 1974, pp. 105-121.
[14] Adams, N. J. I. and Munro, H. G., "A Single Test Method for Evaluation of the J-Integral as a Fracture Parameter," *Engineering Fracture Mechanics,* Vol. 6, No. 1, March 1974.
[15] Bradshaw, F. J. and Wheeler, C., "The Crack Resistance of Some Aluminum Alloys and the Prediction of Thin Section Failure," Technical Report 73191, Royal Aircraft Establishment, March 1974.
[16] *Review of Developments in Plane Strain Fracture Toughness Testing, ASTM STP 463,* American Society for Testing and Materials, 1969.
[17] Srawley, J. E. and Gross, G., "Stress Intensity Factors for Bend and Compact Specimens," *Engineering Fracture Mechanics Journal*, Vol. 4, No. 3, Sept. 1972.

J. D. Buch[1]

Mechanical Behavior Model for Graphites

REFERENCE: Buch, J. D., "**Mechanical Behavior Model for Graphites,**" *Properties Related to Fracture Toughness, ASTM STP 605,* American Society for Testing and Materials, 1976, pp. 124–144.

ABSTRACT: A physically based statistical theory of fracture for polycrystalline bulk graphite is presented. It is based on the inherent weakness of graphitic grains normal to the *a-b* plane and a coincidence alignment of these planes which has been found to have a dominant influence on strength. These concepts lead to a self-consistent treatment of the tensile fracture of graphite on the basis of the physical parameters of grain size, grain orientation, grain cleavage stress, porosity, fracture toughness, and specimen volume. This interpretive analytical model for the fracture of graphite provides a method for predicting the mechanical and fracture behavior of graphite as a function of its microstructure. The concepts and logic are applicable to other material systems.

KEY WORDS: fracture properties, fracturing, statistics, grain cleavage, mechanical properties, porosity, toughness, strength, strains, crack initiation, crack propagation, grain boundaries, graphite

Polycrystalline graphite is a primary material candidate for nosetips in aerospace reentry missile systems because of its thermochemical ablation performance, its resistance to thermal stress, and its mechanical strength at high temperatures. Advancement of graphite technology requires the development of graphite structures that are even less susceptible to thermal stress cracking and ablation. Therefore, precise knowledge of the mechanical and fracture behavior of graphite is required for improvement in the thermostructural behavior of graphite. The determination of the relationship between microstructure and fracture is the key to improvement in the properties of graphite. This approach entails the theoretical modeling of graphite on the basis of its microstructure [*1,2*][2] and the experimental observation of crack propagation in graphite [*3*].

[1] Engineering associate, Prototype Development Associates, Inc., Santa Ana, Calif. 92705.

[2] The italic numbers in brackets refer to the list of references appended to this paper.

Polycrystalline graphites currently manufactured exhibit large variations in mechanical properties. These variations result from different microstructural features not only among the various types of graphite but also within a specific grade of graphite. Previous analytical models [4-6] have been based on statistical approaches that correlate experimental data to fracture in order to predict failure but do not relate fracture to the graphite microstructure.

The objective of this study was to develop a theoretical model for the tensile fracture of polycrystalline graphite solely on the basis of microstructural fractures. The approach to this development was to proceed in a series of cumulative modeling steps. First, fracture was modeled for an idealized pore-free, well-bonded, isotropic graphite. This fracture was on the basis of individual grain fracture on inherent planes of weakness and subsequent arrayment of these microcracks to a critical size deduced from fracture mechanics theory. The nonlinear strain that resulted from the microcracking was used to calculate the stress-strain behavior. Porosity was then added to the model by treating pores as randomly distributed precracked grains. A bimodal distribution of grain and pore sizes that more closely approximates real graphitic microstructures was then considered. Finally, preferred orientation distributions were added that permitted a description of the stress-strain and fracture behavior of anisotropic polycrystalline graphites.

Pore-Free, Well-Bonded Isotropic Graphites

An idealized graphite is assumed for the initial fracture modeling. Cubical grains are bonded together without pores to form a bulk body. These particles are assumed to be reasonable approximations to graphite crystals in the sense that each particle contains a "plane of weakness," which, presumably, is related to the general crystal structure and c-plane orientation of the grain or particle.

Fracture is modeled as a progressive phenomenon that involves the initiation of microcracks within grains. These microcracks increase in density as stress is increased. Furthermore, they join to form arrays of contiguous cracked grains (Fig. 1). Eventually, the crack arrays become large enough to satisfy the macroscopic condition of fracture mechanics for catastrophic growth under the applied stress and failure occurs. Thus, this theoretical graphite fracture behavior involves microcrack formation, microcrack arrayment or the equivalent of stable crack growth, and determination of the critical crack array size or catastrophic propagation.

Microcrack Formation

Within a reasonably well-defined graphitic particle, there will be a plane of weakness associated with the basal plane. Basically, this plane of weakness can be characterized by its orientation, its extent, and the

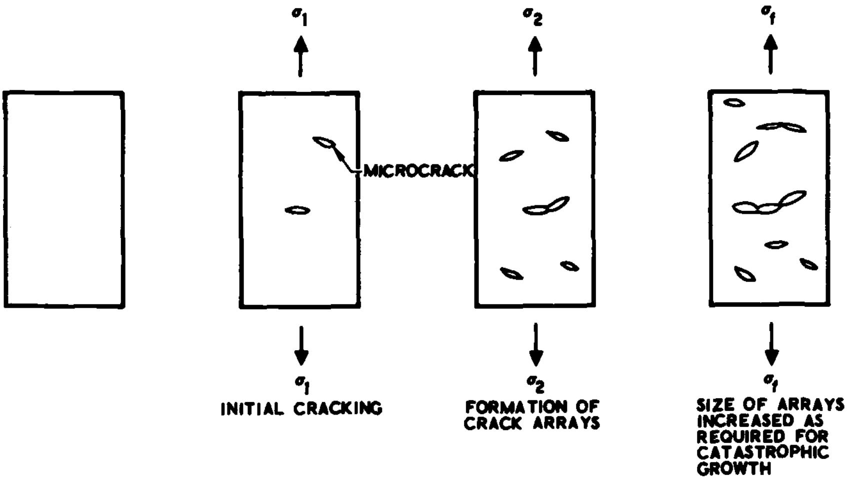

FIG. 1—*Progressive microcracking model.*

tensile stress acting across the plane of weakness required to cause basal plane separation or cleavage. Thus, in principle, the formation and extent of a single isolated microcrack can be predicted.

If the angle between the normal to the plane of weakness of a given grain and the direction of applied stress is ϕ, the component of stress perpendicular to the plane of weakness σ_n is

$$\sigma_n = \sigma_a \cos^2\phi \tag{1}$$

where σ_a is the applied stress. If the plane of weakness is characterized by a cleavage stress S_c, then the plane will have cleaved if

$$S_c \leq \sigma_n = \sigma_a \cos^2\phi \tag{2}$$

The probability of a random grain being fractured is given by the probability that Eq 2 is satisfied or by the probability that

$$\phi \leq \cos^{-1} \left\{ \sqrt{S_c/\sigma_a} \right\} \tag{3}$$

for $S_c \leq \sigma_a$. Obviously, if $S_c > \sigma_a$, no microfracturing will occur. In principle, the value of S_c can be deduced from observations of first microcleavage under stress [*3*].[3]

The orientation distribution of the grains relative to the tensile axis

[3] The assumption of a single, well-defined cleavage strength is very idealistic. A distribution of cleavage strengths is more probable, and a simple distribution will be presented later.

$\Omega(\phi)$ is obtainable from x-ray diffraction measurements of preferred orientation. Initially, randomly oriented grains are considered. It can be shown that for uniaxial tension the probability of grain cleavage P_c will be given by

$$P_c = \begin{cases} 1 - \sqrt{S_c/\sigma_a} & \text{for } \sigma_a > S_c \\ 0 & \text{for } \sigma_a < S_c \end{cases} \tag{4}$$

The mathematical details are presented in the anisotropy section of this paper.

Experimental observation of grain cleavage along planes of weakness has been carried out by observing crack propagation in graphite under stress with a scanning electron microscope (SEM) [3].

Microcrack Arrayment; Stable Crack Growth

The concept of microcrack arrayment involves the probability that in an array of n grains, there will be N contiguous cracked grains. The probability that a random grain and $N - 1$ of its planar neighbors will be cleaved is given by P_c^N. Any one of these neighbors could be taken as the "center" of the array. This array of contiguous cracked grains is referred to as a coincidence alignment. Consequently, the probability P_N of a given grain site being the center of a coincidence alignment of N cracked grains is given by

$$P_N = \frac{(P_c)^N}{N} \tag{5}$$

The probability that it will not be such a center is $1 - P_N$. In a collection of n grains, the probability P_{Nn} that there will be no alignment of N cracked grains is

$$P_{Nn} = \left(1 - \frac{(P_c)^N}{N}\right)^n \tag{6}$$

The probability that there will be at least one planar array of N contiguous cracked grains is given by $1 - P_{Nn}$.

The relationship between these parameters and tension specimens is the association of n with the number of grains within the specimen. This number is a function of specimen volume and grain volume (or size). For cubical grains of size g and a specimen of volume V, $n = V/g^3$. Consequently, the probabilities of coincidence alignment formation of cracked grain arrays depend on grain size, specimen volume, applied stress, grain cleavage stress, and grain orientation probability distribution.

Critical Crack Array Size

The nucleation and arrayment of microcracks cannot continue indefinitely. As stress increases, the large crack arrays eventually reach the critical size at which they extend catastrophically.

Critical crack sizes can be estimated from macroscopic fracture mechanics. Assume that the contiguous cracked grains form a penny-shaped array as in Fig. 2. A circular planar crack is more detrimental to the strength of a material than an elliptical planar crack of the same area. With the grain size g taken to be uniform, N grains will provide a near penny-shaped array of area A given by $A = Ng^2$. The radius r of the penny-shaped area is given by

$$r = g\sqrt{N/\pi} \tag{7}$$

The fracture mechanics approach to failure defines the critical combination of crack size and stress as [7]

$$K_{Ic} = 2\sigma_c\sqrt{r/\pi} \tag{8}$$

or alternatively

$$N = \frac{\pi^3}{g^2}\left(K_{Ic}/2\sigma_c\right)^4 \tag{9}$$

where K_{Ic} is the stress intensity factor, and σ_c is the critical applied stress at fracture.

In macroscopic fracture mechanics, it is assumed that the crack is large compared with the microstructure. As a postulate, then, if the crack array is large compared with the microstructure, the fracture mechanics failure

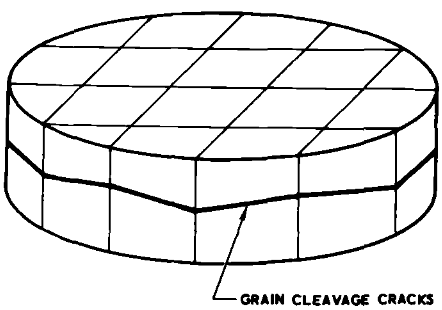

FIG. 2—*Penny-shaped array of contiguous cracked grains.*

condition should apply, that is, the crack array involves many grains (high values of N).

Strain Response

The strain response of the material is composed of several terms: (1) bulk elastic response associated with the elastic modulus and the applied stress, (2) elastic opening of the cracks, and (3) general plastic deformation. For a first-order theory, only the general elastic response and elastic crack opening terms are considered, that is, dislocation motion is ignored.

For uniaxial tension applied in the z-direction, the net strain ϵ_z will be composed of the bulk ϵ_{zb} and crack opening strains ϵ_{zc}. If Y_z is the Young's modulus in the z-direction, then

$$\epsilon_{zb} = \sigma_{az}/Y_z \tag{10}$$

The additional strain $\epsilon_{zc}{}^N$ that results from one circular crack N grains in extent is given by

$$\epsilon_{zc}{}^N = \frac{8}{3} r^3 \frac{(1+\nu)(2-\nu)}{(Y_z)\,\pi/2} \sigma_{az} \tag{11}$$

where ν is Poisson's ratio; the crack radius is $r = g\sqrt{N/\pi}$. This relationship is obtained by examining the displacement field associated with a penny-shaped crack in an infinite medium [8] and computing the displacements that occur between two points a unit distance apart with the crack centered between them.

If the probability that only one random grain site will be the center of a crack array of N grains in extent is P_N (Eq 5), then, in a collection of n grains, there are M_{Nn} crack arrays N grains in extent, as given by

$$M_{Nm} = nP_N \tag{12}$$

If crack-crack interactions are ignored and if all crack sizes are considered, the resulting strain ϵ_{sc} from all expected cracks within the material may be written as

$$\epsilon_{zc} = \sum_{N=1}^{\infty} M_{Nn}\epsilon_{zc}{}^N \tag{13}$$

The total strain ϵ_z then, is obtained by summing the bulk strain and the crack strain, that is

$$\epsilon_z = \epsilon_{zb} + \epsilon_{zc}$$

or

$$\epsilon_z = \frac{\sigma_{az}}{Y_z} + \sum_N M_{Nn}\epsilon_{zc}{}^N \tag{14}$$

The strain response is shown schematically in Fig. 3. The total crack strain increases as stress increases, thereby producing the nonlinear stress-strain behavior.

Failure Prediction

A computer program was written for implementation of the previous equations. At each successive increment of stress the probability of individual grain fracture is calculated from Eq 4. Additionally, at each stress level, the probabilities of grain fracture arrays that exist within the specimen are calculated from Eq 6 for wide ranges of array sizes. Thus, at each stress level, the probability of having a critical size flaw, as defined (at each stress level) by Eq 9, is determined. This automatically determines the probability of specimen failure at each of the incremented stress levels. The output of this program consists of selected points on the stress-strain curve including the fracture point (50 percent probability of failure or survival) and the probability of survival at each point.

The technique can be schematically illustrated in Fig. 4 in which the expected size of the largest microcrack agglomerate in a specimen of unit volume for various levels of confidence is plotted as a function of applied stress. Overplotted is the catastrophic crack propagation criteria as a function of applied stress. The intersections define various failure probability levels, and the divisions into microcrack initiation, stable growth, and unstable propagation become evident.

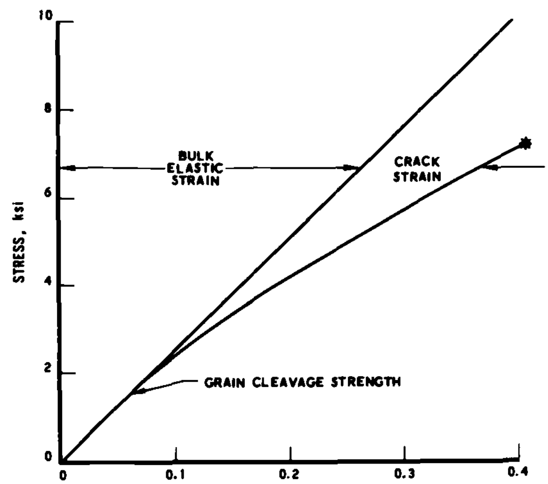

FIG. 3—*Strain response, bulk strain plus crack strain.*

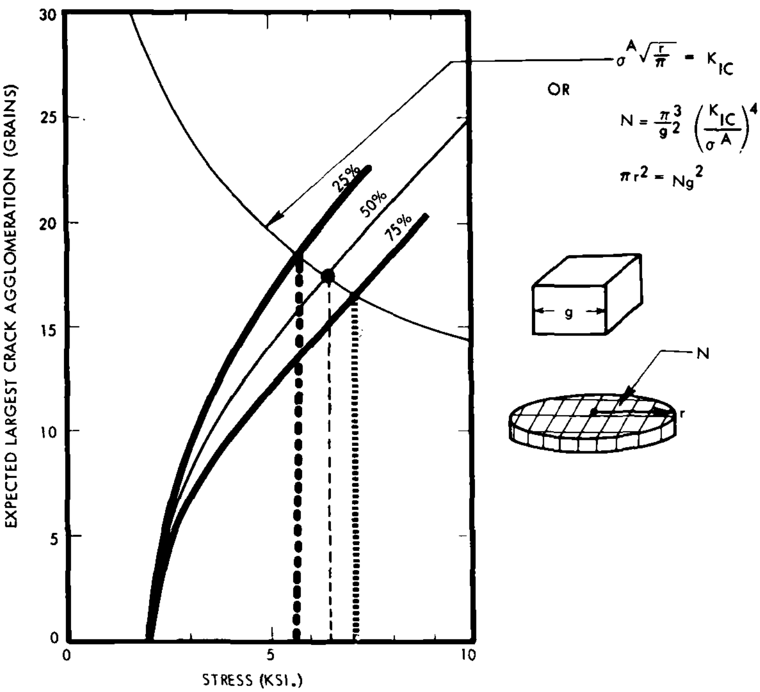

FIG. 4—*Statistics of failure, failure criterion, and fracture mechanics.*

Porosity

Porosity is one traditional physical variable involved in understanding the influence of microstructure on strength [*9-13*]. Porosity generally serves as a moderator of strength and thus is included here as an addition to the basic physical parameters in the fracture model.

Grain Substitution

A pore is modeled as a substitute for a grain. Because a pore has no strength in any direction, it is considered as equivalent to a cleaved or cracked grain. Large pore sizes are modeled as multiple contiguous grains.

In the model, the microcrack arrays can be combinations of cracked grains and pores. The probability that a particular grain site will act crack-like is equal to the probability that it will be either a pore or a cracked grain. The probability that a given grain site will be a pore is P, the volume fraction of porosity. The probability that a given grain site will be occupied by a grain is $1 - P$. If a grain site is occupied by a grain, the probability that it will be cracked is given by Eq 4. Thus, the general expression for a given grain site exhibiting crack-like behavior is

$$P_c' = \begin{cases} P + (1 - P)\left(1 - \sqrt{S_c/\sigma_a}\right) & \text{for } \sigma_a > S_c \\ P & \text{for } \sigma_a < S_c \end{cases} \tag{15}$$

for uniaxial tension. In other words, the pores are distributed randomly over the grain sites as in Fig. 5. It should be noted that this random substitution concept gives rise to pore clusters or agglomerate of contiguous pores as is also indicated.

The formal consideration of fracture proceeds as before, that is, at each stress level, the probabilities of contiguous crack arrays of various sizes are calculated using the modified grain site cleavage probability given by Eq 15. The basic formalism remains the same except that the probabilities of crack-like behavior are altered because of the geometric introduction of porosity. The calculation for strain proceeds as in the zero-porosity model, with one critical difference. The far field strains are calculated as before using the grain site cleavage probabilities; however, the bulk compliance uses net section stresses, that is

$$e_{zb} = \frac{\sigma_z}{Y_{zo}(1 - P)} \tag{16}$$

where Y_{Z0} is the zero porosity Young's modulus.

Parametric Characterization

The influence of porosity on the stress-strain behavior for the isotropic graphite is shown in Fig. 6. A zero-porosity modulus of 2.5×10^6 psi [*14*] has been assumed. The initial elastic modulus decreases and the failure stress decreases as porosity is increased. The reduction in strength results

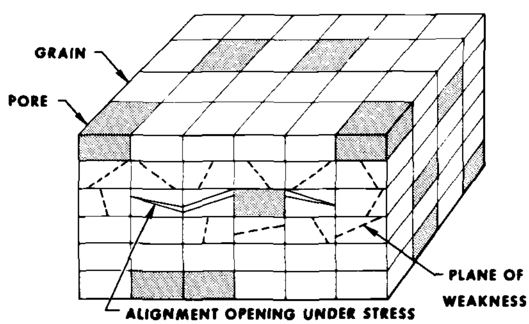

FIG. 5—*Microcrack arrayment including porosity.*

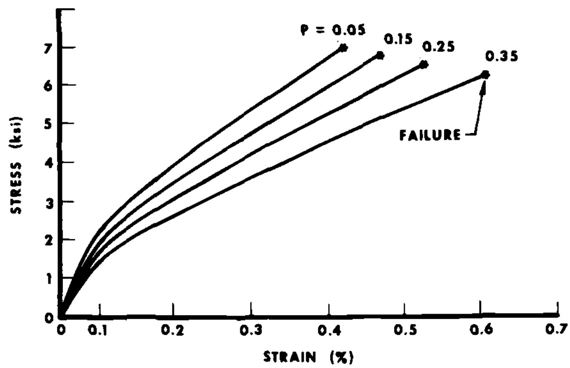

FIG. 6—*Effect of porosity on stress-strain curve.*

from simply adding precracked grains (the pores), thus increasing the probability of microcrack formation at a given stress level as is listed schematically in Fig. 7. The failure strain increases with an increase in porosity; this is relatable to the decrease in modulus. This porosity effect is summarized in Fig. 8 by the solid lines. The reduction in modulus is

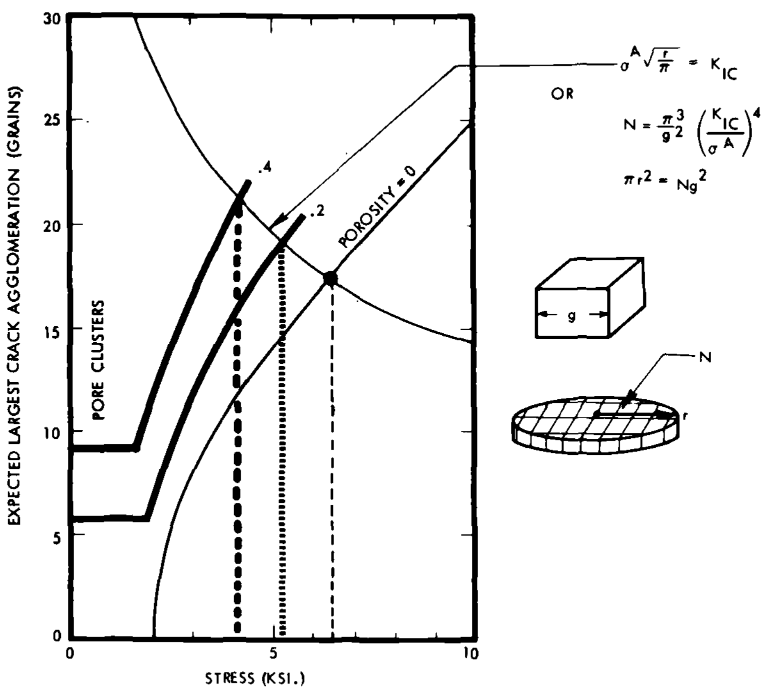

FIG. 7—*Porosity, failure criteria, and fracture mechanics.*

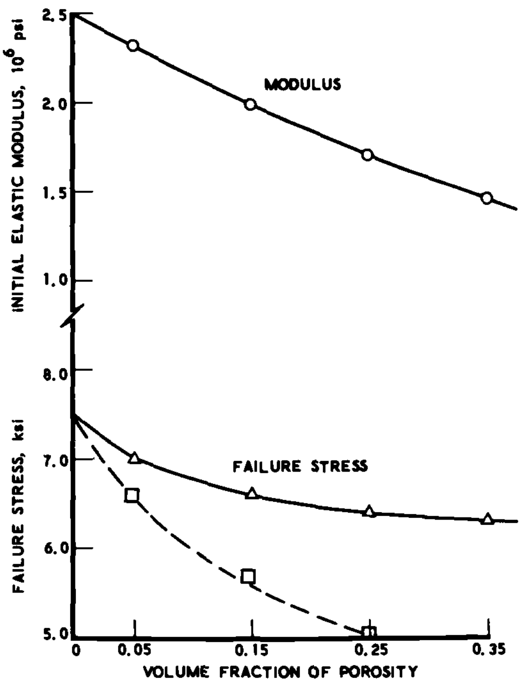

FIG. 8—*Effect of porosity on modulus and failure stress (dashed line couples fracture toughness to porosity).*

stronger than a simple $(1 - P)$ relationship due to the far field displacement terms.

As is true of all parametric characterizations, either all other parameters must be held constant, or interrelationships must be assumed between parameters. A specific example is the influence of porosity on fracture toughness. The initial Orowan modification to the Griffith theory [*15*] implies the definition of fracture toughness as

$$K_{\mathrm{Ic}} = \sqrt{\frac{2E\gamma_p}{\pi(1 - \nu)c}} \tag{17}$$

where γ_p is the specific work of fracture. If linear porosity relationships are assumed for the work of fracture (based upon an area reduction) and modulus (gross stress versus net stress), then it follows that the fracture toughness-porosity relationship should be linear in porosity, that is

$$K_{\mathrm{Ic}} = K_{\mathrm{Ic_0}}(1 - P) \tag{18}$$

This creates a stronger influence of strength on porosity, that is, strength depends more than linearly upon porosity as is shown by the dashed line in Fig. 8. Equation 18, while reasonable, will not be used in the further development of the logic as materials with different behavior are possible, and the ability to consider interparametric relationships within the logic has been demonstrated.

Parametric influences of grain cleavage strength on mechanical behavior are illustrated in Fig. 9. This parameter provides a considerable control over stress-strain behavior, particularly the nonlinear aspect of behavior. A low grain cleavage strength provides many grain cleavages and accompanying inelastic behavior, larger microcrack agglomerates, and diminished strength. The standard caveats against parametric studies and independent parameters apply.

Figures 10 and 11 represent a trade-off study for failure stress and strain in which the theory was force fit to representative data for ATJ-S [*16-18*], and independent parameters of grain size, grain cleavage strength, porosity, and fracture toughness were assumed. In this approximation, not all parameters which contribute to enhanced strength contribute to enhanced strain, a current design parameter for nosetip applications.

What is relevant is that the grain size effect or slope is not a simple integer exponent of $-1/2$ but rather is approximately -0.4. Because of the effect of stable crack growth, that is, the fracture initiation site being many grains in extent, this departure is possible. Further, if parameters

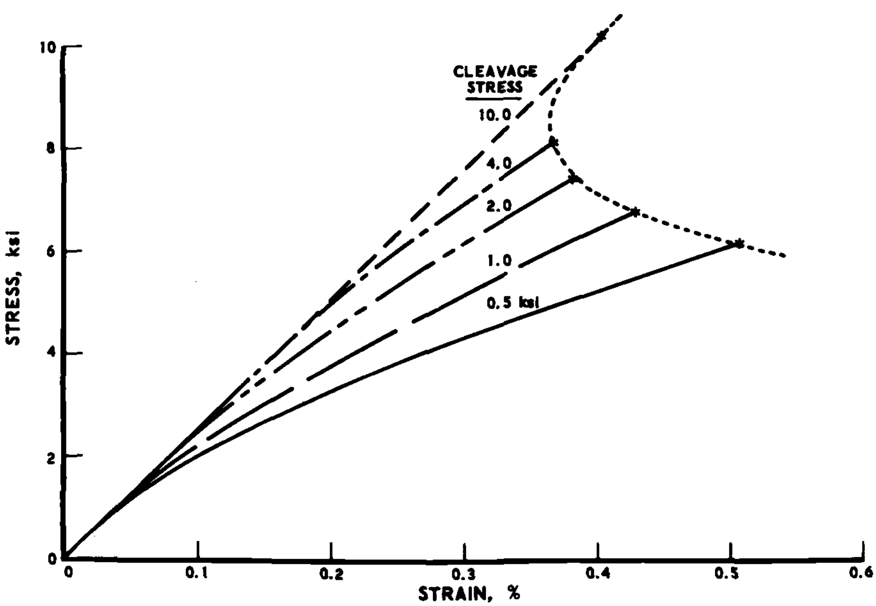

FIG. 9—*Effect of cleavage stress on stress-strain curve.*

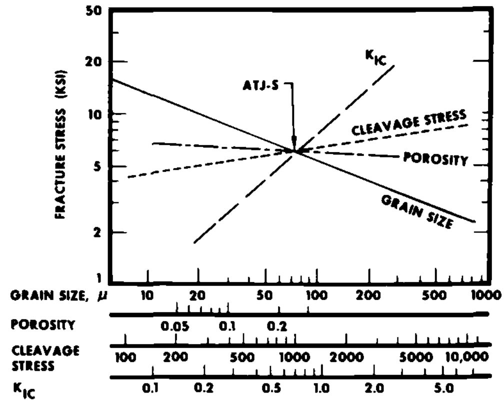

FIG. 10—*Parametric influences on strength.*

such as grain size and fracture toughness or any other combination are allowed to become independent, simple unique integer exponent relationships [*19-22*] between grain size and strength should not be expected. The present formalism appears general enough to account for experimental observations in the technical literature on grain size-porosity-strength interrelationships [*9-13,19-22,23-27*]. Subsequent sections will provide additional capability for simulating real materials and additional amplification on this point.

Grain Boundaries

The influence of grain boundaries on material fracture behavior is quite significant as the concepts of transgranular and intragranular fracture are well known in brittle fracture. Intuitively, it would appear that the

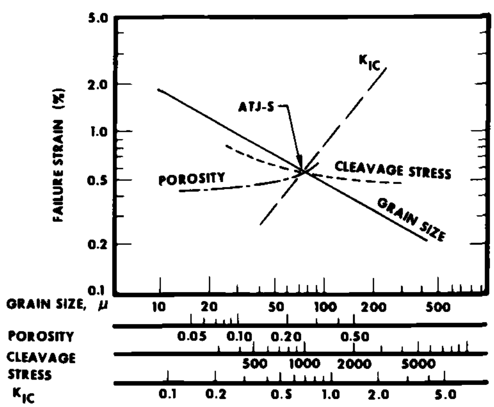

FIG. 11—*Parametric influences on failure strain.*

transition from one form of fracture to another is associated with the boundaries becoming weak relative to the grains and vice versa. This should be capable of descriptive modeling.

Grain boundaries are characterized by three factors: (1) boundary tensile strength, (2) size, and (3) orientation relative to both the tensile load direction and to the plane of weakness. At this point in time it must be explicitly recognized that the cubical array of grain sites is only a computational convenience and not a representation of reality. Dodecahedrons could be used in place of cubical grain sites with minor changes in computational details. The basic modifications for rectangular prismatic grain sites will be presented in another paper [*28,29*].

One type of grain boundary would be that associated with a natural flake or single crystal grain or filler. The surfaces of the particle would then be either *a*-planes or *c*-planes. The boundary orientations would then be fixed or correlated relative to the plane of weakness within the grain, that is, one grain boundary would always be parallel to the plane of weakness. Then to a good approximation, either the boundary fails or the grain cleaves, depending upon which strength is less. The probability of failure of a grain site is then obtained by Eq 15 in which the weaker of the two strengths, S_c for grain cleavage or S_b for boundary failure, is used. The remainder of the logic remains unchanged. Fracture initiation is then either purely transgranular or intergranular unless strength distributions for grains or boundaries or both are invoked.

The second type of boundary description would be represented by the dodecahedron type of grain where the boundary orientation is uncorrelated with the orientation of the plane of weakness within the particle. If it is assumed that the material is isotropic, that is, random orientations, then the failure probability for a grain site by the mechanisms of grain cleavage, boundary fracture, or porosity is given by

$$P_c' = \begin{cases} P & \sigma_a < S_b \text{ and } \sigma_a < S_c \\ P + (1 - P)\ \left(1 - \sqrt{S_b/\sigma_a}\right) & S_b < \sigma_a < S_c \\ P + (1 - P)\ \left(1 - \sqrt{S_c/\sigma_a}\right) & S_c < \sigma_a < S_b \\ P + (1 - P)\ \left(1 - \sqrt{S_b S_c/\sigma_a}\right) & \sigma_a > S_b \text{ and } \sigma_a > S_c \end{cases} \tag{19}$$

The remainder of the argument for crack growth and propagation proceeds as discussed previously with this wider definition of grain site failure probability.

This two strength model is compared with the single strength model in Fig. 12. As either boundary or cleavage stress decrease in the independent parametric sense, the fracture stress decreases and the nonlinearity increases as a consequence of increased microcracking. Depending upon

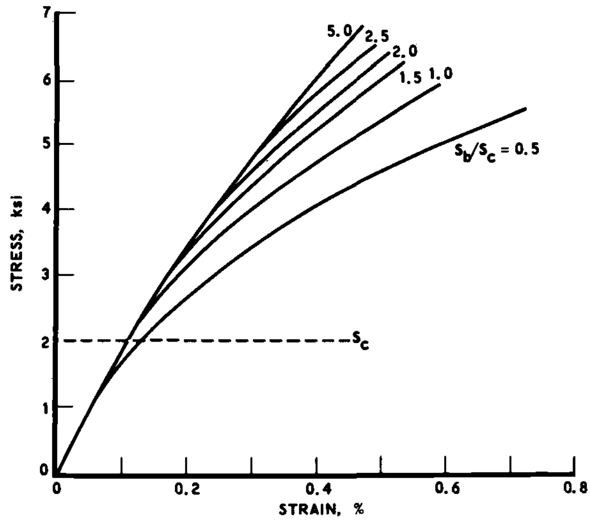

FIG. 12—*Effect of grain boundary-grain cleavage strength ratio.*

the relative ratio of cleavage and boundary strengths, the ratio of transgranular to intergranular aspect of the fracture initiation site will vary. The model at this point can accommodate either transgranular, intergranular, or mixed fracture initiation.

Anisotropy

In previous sections, the orientation distribution of the planes of weakness has been assumed to be purely random, resulting in isotropic stress-strain behavior. This, or course, is not realistic inasmuch as forming operations such as molding or extruding will produce preferred particle (and hence plane of weakness) orientation. In this section, nonrandom orientation distribution functions are discussed.

Crystallite orientation distributions can be determined from X-ray diffraction patterns. From diffraction data, a function can be extracted that represents the orientation distribution of crystallites, usually with respect to a direction of symmetry. In the coordinate system shown in Fig. 13, the basal plane orientation distribution is given by a function, say, $\Omega(\phi,\theta)$. The criteria for individual grain cleavage is

$$\phi \leq \cos^{-1} \left[S_c/\sigma_a\right] \qquad \sigma_a \geq S_c$$

It follows, then, that the probability P_c of individual grain cleavage under uniaxial tension in the Z-direction will be given by

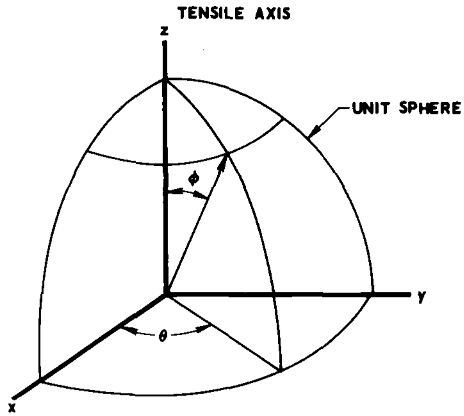

FIG. 13—*Coordinate system for grain orientation.*

$$P_c = \begin{cases} 0 & \sigma_a \leq S_c \\ \dfrac{\int_0^{2\pi}\int_0^{\phi*} \Omega(\phi',\theta')\sin\phi'\,d\phi'\,d\theta'}{\int_0^{2\pi}\int_0^{\pi-2} \Omega(\phi',\phi')\sin\phi'\,d\phi'\,d\theta'}, & \sigma_a > S_c \end{cases} \quad (21)$$

where

$$\phi^* = \begin{cases} \cos^{-1}\left(\sqrt{S_c/\sigma_a}\right) & S_c < \sigma_a \\ 0 & \end{cases}$$

Thus, from the function $\Omega(\phi,\theta)$, the probability of individual grain cleavage can be calculated and used in the basic formal calculation scheme. For a molded graphite stressed in the against-grain direction, the orientation distribution can be approximated by [*30*]

$$\Omega(\phi,\theta) = \Omega(\phi) = \cos^{\alpha}\phi \quad (22)$$

because of symmetry about the tensile axis. For an extruded graphite stressed in the with-grain direction, the orientation distribution is approximated by [*32*]

$$\Omega(\phi) = \sin^{\alpha}\phi \quad (23)$$

For the other tension directions, analogous expressions can be used. An increase in the exponent α or β increases the degree of preferred orientation and hence anisotropy. For random distributions, $\beta = \alpha = 0$. Noninteger exponents are allowed since evaluation of the integrations for cleavage probability can be accomplished by numerical methods.

The effect of anisotropy on the stress-strain behavior of molded or extruded graphites is shown in Fig. 14 where fracture considerations are temporarily excluded. The nonlinear behavior is sensitive to the relationship of the tensile axis to the directions of preferred orientation. This is to be expected on the basis of increased microcracking associated with directions of preferred orientation.

A fit to ATJ-S graphite uniaxial, deformation, and fracture behavior, a current nosetip material, is shown in Fig. 15. Reported grain sizes, porosity, fracture toughness values for each tensile direction, estimated zero-porosity moduli, the measured proportional limit as the estimate of grain cleavage strength [*16,18*], and a concept called large pore inclusions were used.

Volume Effect

One of the classical tests of brittle failure theories is the ability to predict or correlate with a fracture stress dependence on specimen volume [*4,31*]. The basic concept is related to the increased probability of finding a more severe (extreme value) flaw with increased specimen volume. The effect is built into the present model through the number of grains which may serve as the potential fracture initiation site. Data and predictions for ATJ graphite are shown in Fig. 16.

Discussion

The primary point to be brought out is not the ability of an approach to match experimental data but rather the logic for treating both fracture and

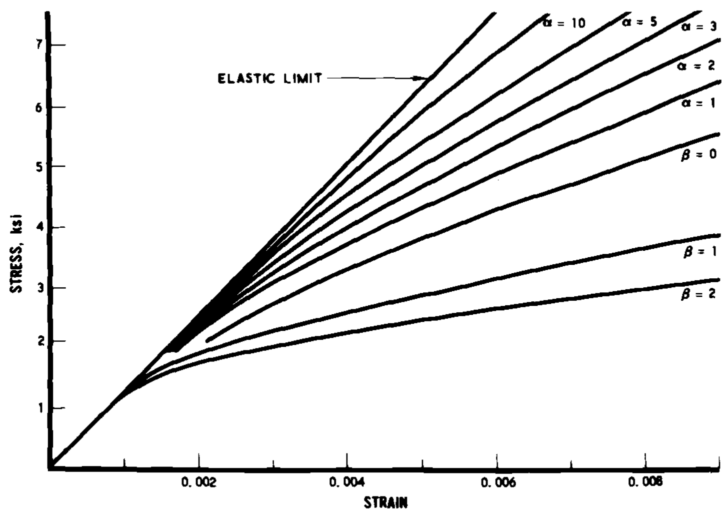

FIG. 14—*Effect of preferred orientation on stress-strain behavior.*

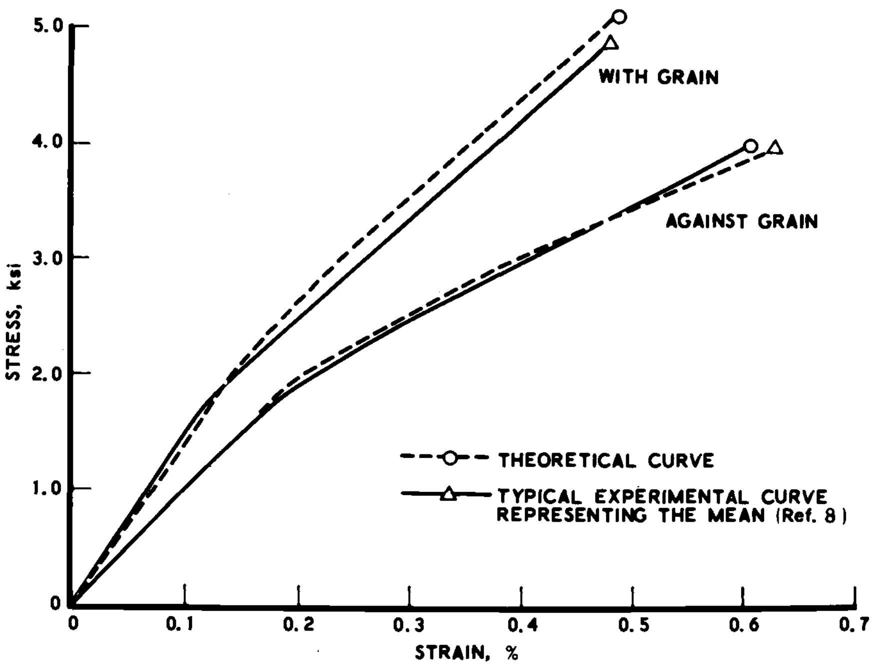

FIG. 15—*Theoretical fit to ATJ-S behavior.*

nonlinear behavior from a self-consistent point of view. Individual grain cleavages and their agglomeration into the macroscopic flaws as stress increases, their achievement of an unstable size, and their contribution to nonlinear response through their far field compliances form the self-consistent concepts. The flexibility of the model to incorporate real microstructural features, such as porosity and mixed trans- and inter-

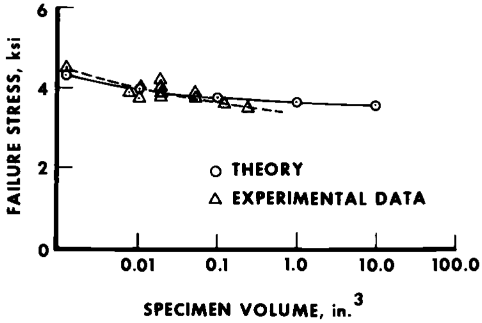

FIG. 16—*Specimen volume effect.*

granular fracture initiation sites and the relationship of preferred orientation to the fracture initiation site are logical and self-consistent. Separate theories are not required.

The major concepts have been verified by observations of deformation and fracture while under stress by both optical and SEM techniques [*3,32*].

The built-in freedom from simple integer exponential relationships between strength, modulus, grain size, and porosity are unique as well and could serve as a partial means of correlating available experimental behavior on materials other than graphite. The logic is unique, in part, in that the critical flaw is not restricted to the size of a single microstructural feature. Interparameter relationships such as toughness-porosity can be accommodated within the logic provided that these relationships are either experimentally known or derivable from a reasonable set of premises.

Summary

A physically based statistical theory of fracture for polycrystalline bulk graphites has been developed. The basic physical concept applied was a preferred direction of inherent weakness in graphitic grains.The new concept introduced by the model is that of a probabilistic "coincidence alignment" of these microcracks, which creates a greater and more detrimental influence than preexisting flaws on the strength of bulk graphites. This concept allowed a self-consistent treatment of the tensile fracture of graphite on the basis of the physical parameters of grain size, grain orientation, grain cleavage stress, porosity, fracture toughness, and specimen volume. The fracture model computes the stress-strain behavior and survival probabilities that permit prediction of the fracture of bulk graphites.

The concepts of microcrack formation because of grain cleavage on planes of weakness during stress and arrayment of these microcracks to a crack of critical size to cause fracture appear sufficient criteria for modeling the fracture of polycrystalline graphite. The strain associated with the progressive microcracking under stress can adequately account for the nonlinear stress-strain behavior of graphite.

This microstructural model for the fracture of graphite provides a method for determination of the mechanical and fracture behavior in tension of bulk graphite as a function of its microstructure.This information is required for improvement in the thermostructural behavior of graphite. This model also permits the prediction of fracture for different graphites without extensive experimental testing by variation of the input microstructural parameters in the associated computer code. With appropriate modifications representing the crystalline nature of other brittle and semibrittle systems, the model may form a more general basis for correlating existing experimental results.

Acknowledgment

The majority of the technical effort reported herein was conducted while the author was employed by the Aerospace Corporation, El Segundo, California. The suggestions and assistance of Drs. R. A. Meyer, J. L. White, and R. C. Rossi contributed significantly to this study. Sponsorship by the Naval Surface Weapons Center, White Oak (formerly Naval Ordnance Laboratory) is gratefully acknowledged.

References

[*1*] Buch, J. D. et al, "An Analytical Microstructural Model for the Fracture of Graphite," Aerospace Report ATR-74(7425)-4, The Aerospace Corporation, El Segundo, Calif., 28 June 1974.

[*2*] Buch, J. D., "A Physically Based Statistical Theory of Fracture Applied to Graphite," in *Continuum Aspects of Graphite Design*, AEC Report Conf-701105, Nov. 1970, p. 501.

[*3*] Meyer, R. A. et al, "Micromechanics of Failure in Carbon Systems," ATR-74(7408)-2, The Aerospace Corporation, El Segundo, Calif., 13 March 1974.

[*4*] Weibull, W., "Statistical Theory of Strength of Materials," *Ingenioersvetenskapsakademien., Handlingar*, No. 151, 1939, pp. 1-45.

[*5*] Robinson, E. Y., "Statistical Nature of Fracture," Technical Report UCRL-50622, University of California Radiation Laboratory, Lawrence, Calif., 30 March 1969.

[*6*] Mathews, R. B., *Journal of the American Ceramic Society*, Vol. 57, No. 5, May 1974, pp. 225-226.

[*7*] Paris, P. C. and Sih, G. C. in *Fracture Toughness and Its Applications, ASTM STP 381*, American Society for Testing and Materials, 1964, pp. 30-81.

[*8*] Sih, G. C. and Liebowitz, H. in *Fracture*, Vol. II, H. Liebowitz, Ed., Academic Press, New York, 1968, pp. 67-190.

[*9*] Knudsen, F. P., *Journal of the American Ceramic Society*, Vol. 42, No. 8, Aug. 1959, pp. 376-387.

[*10*] Carniglia, S. C., *Journal of the American Ceramic Society*, Vol. 55, No. 12, Dec. 1972, pp. 610-618.

[*11*] Hasselman, D. P. H., *Journal of the American Ceramic Society*, Vol. 46, No. 11, Nov. 1963, pp. 564-565.

[*12*] Spriggs, R. M., *Journal of the American Ceramic Society*, Vol. 45, No. 9, Sept. 1962, p. 454.

[*13*] Duckworth, *Journal of the American Ceramic Society*, Vol. 36, No. 2, Feb. 1953, p. 68.

[*14*] Cost, J. R. et al, *Philosophical Magazine*, Vol. 17, No. 148, Sept. 1968, pp. 851-854.

[*15*] Orowon, E., *Reports on Progress in Physics*, Vol. 12, 1948, pp. 186-232.

[*16*] Pears, C. D. and H. G. Sanders, "A Strength Analysis of a Polygraphite," Technical Report AFML-TR-69-204, Air Force Materials Laboratory, Dayton, Ohio, 1970.

[*17*] Anderson, C. A., Ph.D thesis, University of Pittsburgh, Pittsburgh, Pa., 1970.

[*18*] Yahr, G. T. et al, "Application of Fracture Mechanics to Graphite," Paper MP-139, Tenth Biennial Conference on Carbon, July 1971.

[*19*] Petch, N. J., *Journal of the Iron and Steel Institute*, London, Vol. 174, No. 1, Jan. 1953, pp. 25-28.

[*20*] Carniglia, S. C., *Journal of the American Ceramic Society*, Vol. 42, No. 11, Nov. 1965, pp. 580-583.

[*21*] Carniglia, S. C., *Journal of the American Ceramic Society*, Vol. 55, No. 5, May 1972, pp. 243-249.

[*22*] Chay, D. M. et al, *Journal of the American Ceramic Society*, Vol. 51, No. 1, Jan. 1968, pp. 10-16.

[*23*] Spriggs, R. M. et al, *Journal of the American Ceramic Society*, Vol. 47, No. 7, July 1964, pp. 323-327.

[*24*] Knudsen, F. P. et al, *Journal of the American Ceramic Society*, Vol. 43, No. 12, Dec. 1960, pp. 641-647.

[*25*] Cutler, I. B., *Journal of the American Ceramic Society*, Vol. 40, No. 1, Jan. 1957, pp. 20-23.

[26] Coble, R. L. and Kingery, W. D., *Journal of the American Ceramic Society*, Vol. 39, No. 1, Jan. 1956, pp. 377-385.
[27] Rice, R. W., *Proceedings of the British Ceramic Society*, No. 20, 1972, pp. 205-257.
[28] Meyer, R. A. and Buch, J. D., "Micromechanics of Failure in Graphite," Quarterly Progress Report No. 2, Report Number TOR-0073(3521)-2, The Aerospace Corporation, El Segundo, Calif., 20 Feb. 1973.
[29] Buch, J. D. (to be published).
[30] Bacon, G. E., *Journal of Applied Chemistry*, Vol. 6, No. 6, 1956, pp. 477-482.
[31] Freudenthal, A. M. in *Fracture*, Vol. II, H. Liebowitz, Ed., Academic Press, New York, 1968, pp. 591-618.
[32] Meyer, R. A. et al, "Microstructure and Fracture of Carbon Systems, Quarterly Progress Report No. 2," Report No. TOR-0075(5626)-2, The Aerospace Corporation, El Segundo, Calif., 31 Dec. 1974.